OKINAWA INSTITUTE OF SCIENCE AND TECHNOLOGY
GRADUATE UNIVERSITY

Thesis submitted for the degree

Doctor of Philosophy

Topology of band-like excitations in frustrated magnets and their experimental signatures

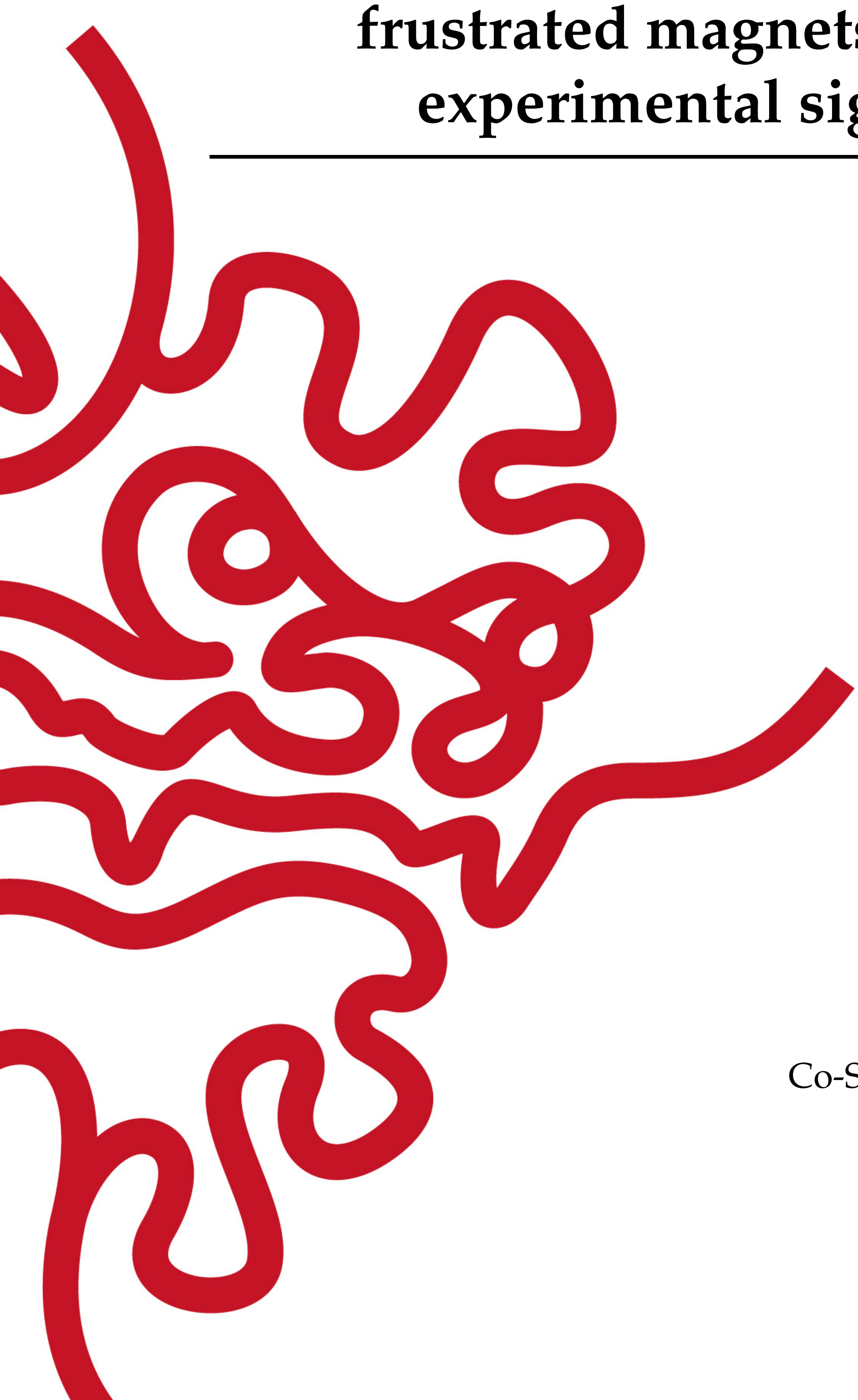

by

Andreas Thomasen

Supervisor: **Nic Shannon**
Co-Supervisor: **Judit Romhanyi**

August 2021

Declaration of Original and Sole Authorship

I, Andreas Thomasen, declare that this thesis entitled *Topology of band-like excitations in frustrated magnets and their experimental signatures* and the data presented in it are original and my own work.

I confirm that:

- No part of this work has previously been submitted for a degree at this or any other university.
- References to the work of others have been clearly acknowledged. Quotations from the work of others have been clearly indicated, and attributed to them.
- In cases where others have contributed to part of this work, such contribution has been clearly acknowledged and distinguished from my own work.
- None of this work has been previously published elsewhere, with the exception of [1] A. Thomasen, K. Penc, N. Shannon, and J. Romhányi, *Novel features of Spin Hall and Chern insulator phases realized by triplet excitations*. arXiv:2012.11765 [cond-mat].

Date: August 24, 2021
Signature: Andreas Thomasen

Abstract

One of the most important revolutions in physics during the latter half of the 20th century must surely be the introduction of topology. Beginning with the discovery of the integer quantum Hall effect, modern condensed matter theory has now discovered a new class of phases with unconventional transport properties. The theory of topologically non-trivial electronic bands in solids is now extremely well-studied. Questions of where similar physics may arise with magnetic excitations have therefore also gained attention. Magnons and other pseudo-particle spin-excitations form a diverse cast with distinct properties that may be important in quantum metrology or even quantum logic tasks and simulation. In this thesis, we investigate the band-topology of such excitations and their experimental signatures.

In our study of the bilayer kagome Heisenberg model we investigate the unconventional excitations of a quantum paramagnet. We show that the $\mathcal{Z}_2$ topological invariant known from the time-reversal invariant quantum spin Hall system of electrons makes an appearance here. These are comparable, but not analogous to Krämers pairs in electron transport, and they can be characterized in a similar fashion, but they do not enjoy the same symmetry protection under time-reversal due to their bosonic nature. We describe how bond-nematic terms appear which destroy the $\mathcal{Z}_2$ phase.

We also study the monolayer spin-polarized kagome Heisenberg model. Our representation theory of the bands allows for the determination of degeneracies as well as interactions which give rise to non-trivial band-gaps. We show how one may associate certain features in the neutron scattering spectra with topological excitations. We show that pinch-points and half-moon features found ubiquitously in neutron scattering experiments will undergo characteristic distortions when those bands carry Chern numbers.

Our work paves the way for a more systematic experimental characterization and treatment of topologically gapped magnetic excitations and motivates experimental investigation of the spin Nernst effect in for instance quantum dimer materials, or possibly in certain ferro-quadrupolar ordered solids.

Acknowledgments

I would like to first acknowledge all my dear friends at Okinawa Institute of Science and Technology (OIST). There are too many to list here, but the student body of OIST has so many exceptional individuals, it is hard to imagine a life outside of this great community. During my time on the student council, Dr. Ankur Dhar was an inspiration to me both in his dedication and his principled leadership. I continue to be impressed by the organization skill and professionalism of Tom Burns and the natural easy leadership of Otis Brunner, to name a few.

For their camaraderie and support, I would like to acknowledge my friends and colleagues in the Theory of Quantum Matter Unit. Dr. Geet Rakala for discussing interesting new research combining machine learning and condensed matter which has had a big impact on me. Dr. Matthias Göhlke who has been my lunch friend during most of my thesis writing process. Dr. Tokuro Shimokawa, whose expertise and dedication from the beginning has been impressive to witness. My dear friend and mentor Dr. Karim Essafi, whom I owe a debt of personal gratitude. I am grateful to have met and befriended fellow PhD students Kimberly Remund, Soshi Mizutani, Leilee Chojnacki and Ananya Samanta, and of course, I wouldn't have gotten anywhere without our research unit administrator Megumi Ikeda, who has solved more problems for me than I can count.

My collaborator Dr. Han Yan has always had a habit of asking me the right questions. It has been especially valuable to me to discuss the work of Chapter 5 with him. Physics discussions with Han are never boring, and I am grateful to have stayed late in the office with him during our time in Okinawa together, and later during video calls.

Prof. Karlo Penc has been an invaluable collaborator. The ideas that led to the results of Chapter 4 originated with Prof. Penc, and part of the analysis in Chapter 4 was done by him. I also acknowledge conversations I have had with Prof. Penc and his student Peter Balla concerning representation theory.

I thank my co-supervisor Prof. Judit Romhányi who has only ever accepted correct answers from me and nothing less. She taught me the fundamentals of group theory and magnetism, but more importantly, working with Prof. Romhányi I learned how to truly have integrity as a scientist, and how to be critical of my own results. Prof. Romhányi has also given invaluable feedback for my thesis.

It goes without saying that I am tremendously indebted to my supervisor Prof. Nic Shannon. Prof. Shannon has been a great source of encouragement for me from the beginning. He has supported me throughout the writing of this thesis and given me much helpful feedback with regards to science and life in general. For his tireless

dedication and countless hours spent on me as his student, I could not thank Prof. Shannon enough. But the completion of this thesis I hope is a good start.

Lastly, I am tremendously thankful to have carried out my PhD in Okinawa. This is a truly amazing place to spend a 5 year PhD programme. The people I have met here are unforgettable. It is also here I found the love and support of Sanae Shimoji.

I dedicate this thesis to my grandfather
Thomas Thomasen
1925 - 2016

Contents

List of Figures

List of Tables

Chapter 1

Introduction: What is topological about band-like excitations and why should you care?

One of the foundations of solid state physics has been the characterization of crystalline materials as electronic insulators or conductors[14, 15]. In the band-theory of electronic solids, the appearance of an energy gap between conduction and valence electrons explains the behavior of many insulators. Before the topological nature of this band-gap was understood, such materials were not considered to form a wide range of phases of matter. But it appears that topology has now given us an entirely new perspective on what these band-insulators do, leaving open a space for us to explore rich new physics, with implications on technology, industry and fundamental physics research [6, 16–18]. Throughout this thesis we will explore some of the developments in this field arriving at its implications on magnetism where our own results apply.

In this Chapter we will briefly review the history of topological band-insulators and the implications it has had on theoretical physics in condensed matter. We will begin by considering the integer quantum Hall effect. Historically the work that originated this field concentrated on the electron transport properties of two-dimensional (2D) materials [19]. We will follow the same route in this chapter and begin by considering the discovery of the quantum Hall effect by von Klitzing [2] and the Laughlin argument for the existence of quantum edge modes [3]. This leads to a description of the TKNN formula [20], which introduces the Chern number explicitly in the Hall response. This is followed by the quantum Hall physics of the Haldane model of spinless electrons [4]. Expanding on the concept of the Chern number we then introduce the Kane and Mele model, which includes the spin degree of freedom of the electron [5]. This enables non-trivial topology due to a global spin-degeneracy in the presence of spin-orbit coupling.

The historical review at this stage has so far focused on electron bands, but although some of the conclusions and phenomena do not carry over exactly, the topological band theory of single-particle excitations may in reality be applied to any kind of band system [21]. Topological excitations can be found in a very wide range of media, since the mathematics describing them is universal. Notable examples are cold atom Bose-Einstein condensates with topological defects[22, 23], mechanical [24, 25] or photonic systems [26]. There is no fundamental need for topologically non-trivial systems or their excitations to be in a coherent quantum state, although examples of those are also found in for instance majorana fermions [27, 28].

The bosonic excitations of magnetic insulators have had a role to play in this story too [29–32]. Unlike their fermionic counterparts, any response resulting from their excitation results from their Berry's curvature being weighted by a Bose factor. Thus strictly speaking, non-zero Chern numbers are not a requirement for transverse transport. This was understood by Katsura, Nagaosa and Lee who presented a theory of the magnon Hall effect in 2010 [33]. That same year the experimental verification followed by Onose [9]. It was later shown that the magnon wave-packet has a rotational and precessional motion, both of which must be considered in the calculation of the thermal Hall effect [34, 35]. Interestingly, whereas the electron wavepacket is affected by a Lorentz force due to the magnetic field, the Lorentz force affecting magnon trajectories is the Berry's curvature. It was only later argued that magnonic bands would display the same topological physics as their electronic counterparts, with Chern numbers and associated quantum edge modes [36, 37].

This argument was later applied to more exotic excitations in a study of the quantum paramagnet $SrCu_2(BO_3)_2$ by Romhányi, Penc and Ganesh [11]. Here the thermal Hall current was carried by the triplet manifold of excited states existing complementary to the dimer singlet ground state - so called triplons. This is an example of a material which needs a quantum mechanical description to be studied properly.

In the following sections we will go into more detail with each of these developments. In Section 1.1 we will introduce the concept of the topological band-gap as it appeared historically and came to be understood, culminating in the TKNN formula for transport. In Section 1.2 we will then describe the more complete picture of topological insulators as described by Haldane and Kane and Mele. Finally in Section 1.4 we describe the development of topological band-theory in magnetic insulators.

1.1 What is a topological band-gap?

In this section we will go through some of the experimental discoveries and subsequent theoretical breakthrough that led to our understanding of the integer quantum Hall effect. This is the famous quantized transverse conductance of materials which band theory would previously have deemed to be insulating. To better appreciate this, we briefly review the basic band theory of metals and insulators.

1.1.1 Prelude: The band theory of solids

The free-particle model of metals [38] could not properly answer why certain materials could conduct electricity and others could not. However, with the advent of quantum mechanics, it was possible to distinguish between filled and unfilled electronic states based on Fermi statistics [39]. This allowed the concept of a Fermi surface in reciprocal space, i.e. the space of wave-vectors

$$\vec{k} = (2\pi/\lambda_x, 2\pi/\lambda_y, 2\pi/\lambda_z). \tag{1.1}$$

An additional component needed was the description of bands, to which Bloch's theorem is central [40]. It states that given a periodic potential, such as the atomic nuclei of a metal, the single-particle solutions of the Schrödinger equation can be written as

$$\psi_{\vec{k},a} = e^{i\vec{k}\cdot r} u_{\vec{k},a}(r). \tag{1.2}$$

Here bands are indexed with a. Each band represents a separate solution to the real component $u_{\vec{k},a}(r)$ which encodes the magnitude of the wave-function. $u_{\vec{k},a}(r)$ determines the potential energy of each wave-function belonging to index a. Our concept of a band then comes from the quasi-continuous eigenenergy $\epsilon_a(\vec{k})$, which spans a finite range of values in $\vec{k}$-space.

Bands belonging to distinct a may overlap in energy or be separated by a gap. The band-insulator can be understood by considering the case where two bands are gapped, while the chemical potential is within this gap. If that is the case then the lower energy one is completely filled while the upper one is empty. In this case there is no Fermi surface and therefore the material will be insulating (as explained for instance in [15, Chapter 7]).

This powerful concept together with ab initio methods such as density functional theory [41] has remained the starting point for understanding material conductivity. Insulators within this framework were considered to all belong to the same class of materials. However, we now know that they form a very diverse cast with distinct properties [29]. It took physicists by complete surprise when it was discovered in experiment that the seemingly innocuous insulator had been hiding a secret all along: The integer quantum Hall effect.

1.1.2 The integer quantum Hall effect

The integer quantum Hall effect is the appearance of a quantized Hall conductance in an otherwise electronically insulating sample. Its magnitude is determined by natural constants h and e as well as an integer ν. It has the very simple form

$$\sigma_{xy} = \nu e^2/h, \tag{1.3}$$

and when it was discovered by von Klitzing et. al. [2] it changed condensed matter physics in profound ways. Here the integer ν represents a filling factor, i.e. at a certain Fermi level this number of bands are filled completely. This gives a quantized conductance in steps determined only by the fundamental charge e and Planck's constant h. It is important to appreciate that condensed matter systems consist of a myriad of particles interacting in complex ways. The experimental setup of von Klitzing et. al. used a metal oxide field effect transistor (MOSFET) which is made up of a semiconductor material with several regions that are doped separately. The conductance of such a material should ordinarily depend on substrate and dopant

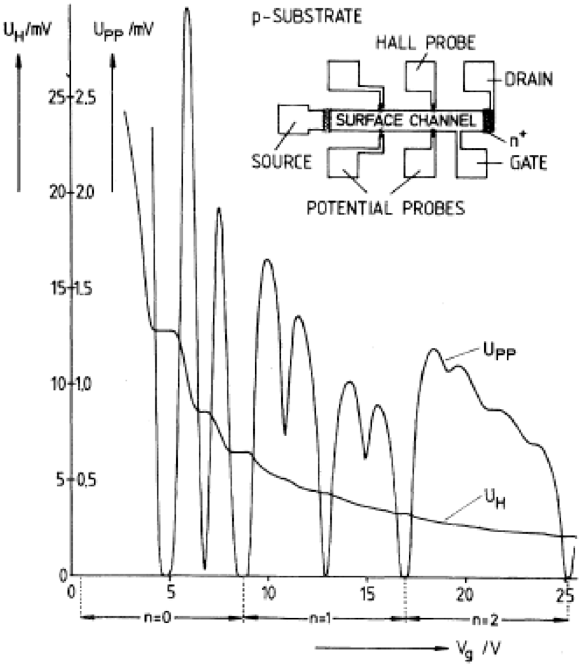

Figure 1.1: Experimental results from the discovery of the quantum Hall effect by von Klitzing et. al. Here the first axis is the gate voltage across a CMOS device, and the second axis is the measured Hall voltage. Figure reproduced from [2]

choice, carrier mobility and density, gate, supply and drain voltages. This is not to mention impurities in the sample. Ordinarily, measuring fundamental physical constants to high precision requires elaborate experiments which have the capability to isolate single quantum particles.

However, von Klitzing found that the fraction e^2/h could be measured to very high precision using this method. They were able to report an accurate determination of the fine structure constant α^{-1} to an accuracy of 6 significant digits, which should be compared to the best methods at the time being about 7.

This mysterious expression was not immediately explained. Why should a Hall response be quantized in this way? Something deeper and more fundamental than what was previously known was suddenly manifesting itself in a band-insulator, a phenomenon that has since been studying in many variants including the fractional quantum Hall effect [42–46].

In von Klitzing's experiment using a metal oxide semi-conductor, the Fermi-level was tuned with an applied gate voltage to alternately lie in a region with a high density of states and within the gap between Landau levels (see figure 1.1). Although von Klitzing did realize that the observed quantized Hall effect was caused by the quantization of Landau levels, the exact mechanism was unclear and the fact that conductivity relied solely on universal constants shocked the physics community. Transport equations normally relied on technically involved and difficult derivations using Green's functions involving carrier density, applied potentials and external magnetic fields. The universality of this result meant that there was fundamental physics that had gone unnoticed until this point.

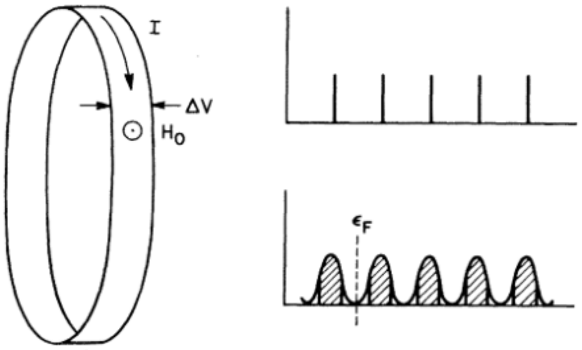

Figure 1.2: The loop geometry considered by Laughlin is depicted here. Included is also a simplified view of the Landau levels, which explains the physics of the integer quantum Hall effect in the absence of edge effects. The broadening due to impurities on the bottom right inset is taken into account when explaining the effect in real materials. Figure reproduced from [3]

It was then argued by Laughlin [3] that this effect could be explained by the long-range coherence of an electronic wave-function and that gauge-invariance together with an energy gap would be sufficient to explain the quantum Hall effect. The argument of Laughlin can be summarized for single-particle wave-functions by considering the effect of having them stretched across a loop-like geometry as seen in figure 1.2. The path around the loop is described by the coordinate $x \in [0, L)$. We consider then a flux ϕ through the loop with a corresponding vector potential defined along the positive x-direction along it. Therefore any gauge transformation caused by ϕ on the wave-function, i.e.

$$\psi_{k,a} \to e^{ieAx/\hbar c}\psi_{k,a} \tag{1.4}$$

is constrained by

$$A = n\frac{hc}{eL}. \tag{1.5}$$

Here n is some integer. This gauge symmetry allows us to consider transformations that take the system into itself.

Laughlin considered the Hamiltonian

$$\hat{H} = \frac{1}{2m^*}(\vec{p} - \frac{e}{c}\vec{A})^2 + eE_0 y. \tag{1.6}$$

Here a magnetic field of strength H_0 penetrates the surface of the strip, while E_0 is the electric field across the strip in the y direction. The Landau gauge can be picked for $\vec{A}$. Thus

$$\vec{A} = H_0 y\hat{x}. \tag{1.7}$$

The solutions are the familiar Landau levels

$$\psi_{k,n} = e^{ikx}\phi_n(y - y_k), \quad y_k = \frac{\hbar k}{eH_0}. \tag{1.8}$$

Here the k must due to the periodic boundary conditions be quantized in multiples of some integer j as

$$k = 2\pi j/L. \tag{1.9}$$

The $\phi_n(y - y_k)$ are the bound-state solutions to the Harmonic oscillator equation,

$$\left[\frac{1}{2m^*}\hat{p}_y^2 + \frac{1}{2m^*}\left(\frac{eH_0}{c}\right)^2 y^2\right]\phi_n = (1/2 + n)\hbar\omega_c\phi_n. \tag{1.10}$$

Thus the wave-functions $\psi_{k,n}$ are in this basis a product of a Harmonic oscillator bound state $\phi_n(y - y_k)$ in the y-direction with quantum number n centered around y_k and the x dependent phase-component e^{ikx}.

The effect of introducing a flux $\delta\phi$ through the loop is to change the vector potential by an amount

$$\delta\vec{A} = \delta\phi/L\hat{x}. \tag{1.11}$$

This then has the effect of shifting the center of mass of each Landau wavefunction by an amount

$$\delta y = -\delta\phi/LH_0. \tag{1.12}$$

Notice that each time the flux changes by a single flux quantum,

$$\Delta\phi = hc/e, \tag{1.13}$$

the vector potential changes by an amount

$$\Delta\vec{A} = \frac{hc}{eL}\hat{x}. \tag{1.14}$$

This has the effect of mapping the wave-function back to itself due to the aforementioned gauge symmetry. Note also that

$$\Delta y = \Delta A/H_0 \tag{1.15}$$

is the spacing between Landau levels along the width of the strip. The physical interpretation of this is that as the Landau wave-functions are adiabatically moved through the sample, the system reverts to its initial configuration after each Landau orbital has shifted by exactly one spacing. Thus one elementary charge is moved for each filled Landau level for each flux quantum.

Now, if one considers the threaded flux to be slowly varying, such that the filling of Landau levels below the Fermi energy remains unperturbed, we can examine the electromotive force (EMF) along the strip geometry and compare it with the current generated.

$$\frac{dQ}{dt} = \frac{1}{c}\sigma_{xy}\frac{d\phi}{dt} \tag{1.16}$$

Integrating both sides of this equation and rearranging we obtain

$$\sigma_{xy} = c\frac{\Delta Q}{\Delta\phi} = \nu\frac{e^2}{h}. \tag{1.17}$$

Here ν is the number of filled Landau levels, which at the same time gives the number of charges transferred across the sample.

We see in this case that because the only gauge transformations possible on the wave-function are dictated by the topology of the geometry it is embedded in, and because of the adiabatic transport associated with the Landau levels, we obtain a robust transport which is quantized in terms of fundamental constants. We can therefore understand already that this quantized response comes from the necessary description of the wave-function as a topologically non-trivial map, in this case from x to the gauge of the wave-function. Moreover, one of the most elegant conclusions of this argument is that the gauge-fixing condition of the wave-function must persist even in the presence of impurities (so long as the perturbations thus introduced are not large enough to bridge the Landau levels). This is because gauge-invariance is determined by the geometry of the strip and this cannot be changed by local perturbations.

Interestingly, not only is this edge current therefore robust against sample impurities, in real materials impurities are in fact needed for an integer quantum Hall effect. The conditions and sources of breakdown of the quantum Hall effect have been studied in a number of works by Joynt and Prange [47–50].

It was later argued by Halperin [51] that as well as the bulk Landau levels, there are quasi one-dimensional modes at each edge of a sample which carry a current. These states are robust against perturbations and remain coherent around the edge on which they are defined and they are still the subject of thorough research in a variety of physical systems [52–58]. This is a general feature of topologically non-trivial band-structures, as the confining edge forces the gapped bands to terminate through an edge mode.

The explicit calculation of the transverse transport in 2 dimensions was carried out using the Kubo formula, when the Fermi energy is in a gapped region. This was first done by Aoki and Ando [59]. Later Thouless, Kohmoto, Nightingale and den Nijs [20] showed that this Hall conductance depends on a global integral over the Berry's curvature of each filled Landau level. This results in the appearance of Chern numbers in the response theory, which can be equated to the filling factor of the Landau levels.

The Kubo formula [60] allowed them to write the Hall conductance as

$$\sigma_{xy} = \frac{ie^2}{A_0\hbar} \sum_{\epsilon_\alpha < E_F} \sum_{\epsilon_\beta > E_F} \frac{(\partial\hat{H}/\partial k_1)_{\alpha,\beta}(\partial\hat{H}/\partial k_2)_{\beta,\alpha} - (\partial\hat{H}/\partial k_2)_{\alpha,\beta}(\partial\hat{H}/\partial k_1)_{\beta,\alpha}}{(\epsilon_\alpha - \epsilon_\beta)^2}. \tag{1.18}$$

By taking the spectral decomposition of the Hamiltonian, this can be expressed as

$$\begin{aligned} \sigma_{xy} &= \frac{ie^2}{2\pi h} \sum_{\epsilon < E_F} \int d^2k \int d^2r \Big(\frac{\partial u^*}{\partial k_1} \frac{\partial u}{\partial k_2} - \frac{\partial u^*}{\partial k_2} \frac{\partial u}{\partial k_1} \Big) && (1.19) \\ &= \frac{ie^2}{4\pi h} \sum_{\epsilon < E_F} \oint d\mathbf{k} \cdot \int d^2r \Big(u^* \nabla u - \nabla u^* u \Big). && (1.20) \end{aligned}$$

Note that the u above is written according to the convention of TKNN, where it includes the phase component of the wave-function. It corresponds to $\psi_{k,a}$ rather than $u_{k,a}$ in our notation. While the choice of gauge is in general arbitrary, TKNN showed that due to the translational invariance of the wave-function, the line integral along the Brillouin zone boundary must result in an integral multiple of $4\pi i$. We can therefore define a number

$$c = \frac{1}{i4\pi} \sum_{\epsilon < E_F} \oint d\mathbf{k} \cdot \int d^2 r \Big(u^* \nabla u - \nabla u^* u \Big). \tag{1.21}$$

This is the so-called Chern number, which evaluates to 1 for Landau wave-functions. Therefore the filling factor in the integer quantum Hall effect can be equated to this number (up to a sign difference due to definitions of x and y) to obtain the quantized response

$$\sigma_{xy} = -ce^2/h. \tag{1.22}$$

Thereby it is explicit that an integer must enter the transport equations regardless of the edge-geometry. The integrand of equation (1.20) is the Berry's connection, which when integrated along the edge of the Brillouin zone gives the Chern number. For an elegant and thorough explanation of this see [61]. Not only did the TKNN paper show that such integers are important invariants of the wave-function, which have an effect on the transport theory, they were also able to simultaneously show that the Landau levels of the electron gas carried Chern numbers.

Remarkably, we therefore have two independent arguments leading to the same conclusion. Namely that the transport is governed by a topological quantum number in the band-insulating regime. TKNN directly calculate this using the Kubo formula, which does not depend on the shape of the boundary. This is complementary to the work done by Laughlin, in which the wavefunctions are calculated in an explicit example which shows how the wave-function facilitates this edge current.

The fractional quantum Hall effect, is caused by fractional filling of the Landau levels of Laughlin's analysis. Here the quantization of σ_{xy} takes place at fractional multiples of e/h. This is an interesting effect in its own right which has its origins not in single-particle band theory, but rather in effective field theories [62–64]. This is a state of matter that has the potential to host nonabelian anyons [65], and it's been observed to occur in graphene [66]. There is also an interesting experimental proposal for the realization of $\nu = 1/2$ fractional quantum Hall effect in ultracold dipolar molecules [67].

1.2 The Lattice Models of Haldane and Kane and Mele

The appearance of topological invariants in the response theory gives a more formal way to link very surprising physics with the fundamental mathematics of topologically non-trivial maps. These ideas were expressed very elegantly in the seminal 1988 paper by Haldane [4]. Here the explicit role of crystal symmetries is explored for the first time, and a model is developed which expresses all of the physics discussed so far in this chapter.

Haldane explores a tight-binding model where time-reversal symmetry is bro-

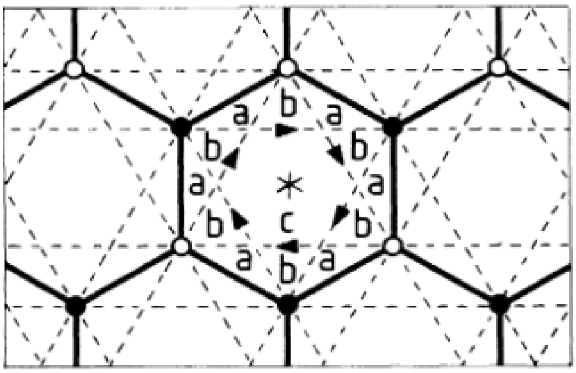

Figure 1.3: This graphic indicates the lattice vectors and the geometry of the Haldane model. Complex hopping occurs along the next-nearest neighbor paths indicated with a dashed line. Figure reproduced from [4].

ken by spontaneous ordering of magnetic moments in a honeycomb lattice. This originates a complex hopping term in the Hamiltonian as charges move through a non-zero vector potential. The Hamiltonian is written as

$$\hat{H} = t_1 \sum_{\langle i,j \rangle} \hat{c}_i^\dagger \hat{c}_j + \text{H. c.} + t_2 e^{i\phi} \sum_{\langle\langle i,j \rangle\rangle} \hat{c}_i^\dagger \hat{c}_j + \text{H. c.} + M \sum_{i\in A, j\in B} (\hat{c}_i^\dagger \hat{c}_i - \hat{c}_j^\dagger \hat{c}_j). \tag{1.23}$$

Here M has been included to study the model when inversion symmetry is broken. The phase ϕ accrued through hopping is equal to the line integral of the vector potential along the hopping direction, i.e.

$$\phi = \int e/\hbar \vec{A} \cdot d\vec{r}. \tag{1.24}$$

The orientation of the vector potential $\vec{A}$ is sketched in figure 1.3. Haldane describes this as originating from a periodic magnetic flux density $\vec{B}(r)$ which lies in the z-direction. This field contributes a zero net flux through the unit cell. It is imagined, that this could originate from some anti-ferromagnetic ordering of local spins.

Because $\vec{A}$ is derived from this field, the phase accrued by hopping along a closed path must equal the total flux enclosed by the loop this path specifies. Since the unit cell encloses zero flux, it is only t_2, the next-nearest neighbor hopping, which is affected by $\vec{A}$.

Haldane originally wrote his model in the two sublattice Fourier basis $(\psi_{k,a}, \psi_{k,b})$ the Hamiltonian becomes

$$\begin{aligned} \hat{H}(\vec{k}) = {} & 2t_2 \cos\phi \Big(\sum_i \cos(\vec{k} \cdot \vec{b}_i) \Big) \boldsymbol{I} + t_1 \Big(\sum_i [\cos(\vec{k} \cdot \vec{a}_i) \boldsymbol{\sigma}_1 + \sin(\vec{k} \cdot \vec{a}_i) \boldsymbol{\sigma}_2] \Big) \\ & + \Big[M - 2t_2 \sin\phi \Big(\sum_i \sin(\vec{k} \cdot \vec{b}_i) \Big) \Big] \boldsymbol{\sigma}_3. \end{aligned} \tag{1.25}$$

This is what one obtains by projecting the Hamiltonian of equation (1.23) onto the space of single-electron wave-functions. Here the lattice vectors $\vec{a}_i$ and $\vec{b}_i$ correspond to the solid and dashed lines respectively of figure 1.3. The σ_i are Pauli matrices acting on the sub-lattice basis states.

Using this model, Haldane is able to formulate the topological map from a two-dimensional k-space to the coefficient space of the three Pauli matrices which is determined by the terms in the Hamiltonian. The crux of the argument here is that there is no way to trivially map these two spaces, since one of them is a sphere and the other is a torus (see Chapter 3).

This is an extremely important insight. The Hamiltonian is written as

$$\hat{H}_{\vec{k}} = \vec{d}(\vec{k}) \cdot \vec{\sigma} \tag{1.26}$$

where we have discarded diagonal terms. Each d_i is a coefficient belonging to the corresponding σ_i as they appear in equation (1.25). The orientation of $d_i(\vec{k})$ defines a point on the Bloch sphere, which in turn defines a pair of spinors that satisfy the Schrödinger equation. We have to therefore define the wavefunction $\psi : \vec{k} \to A(\vec{k}) \left|\psi_{\vec{k}}\right\rangle$. However, this map cannot be completed without introducing a phase discontinuity because the wavefunction has to be defined for each point on a sphere, whereas the quasi-momenta exist on a torus. The torus and the sphere are examples of closed surfaces which do not have the same genus. As such, any map between them is not homeomorphic.

The Chern numbers associated with this map are what appear in the TKNN formula, which gives a non-zero transverse conductance in the insulating state. It is remarkable that we can think of the quantum Hall effect as a consequence of the topology of the band-structure. Because of the universality of this result, the Haldane model has been recast in a large variety of systems including ultra-cold fermions, localized spins and magnetic excitations [68–74]. Models for the fractional Chern insulator, that is a lattice model for the fractional quantum Hall effect, have also been discussed [75, 76].

It was later realized that in systems with time-reversal symmetry, electron transport could still facilitate topological bands. The celebrated model introduced by Kane and Mele [5, 77] showed that spin-orbit coupling allowed for a topological band-gap whilst keeping the spin components degenerate.

$$\begin{aligned}\hat{H} =& t_1 \sum_{\langle ij\rangle\alpha} \hat{c}^{\dagger}_{i,\alpha}\hat{c}_{j,\alpha} + i\lambda_{SO} \sum_{\langle\langle ij\rangle\rangle\alpha\beta} \nu_{ij}\hat{c}^{\dagger}_{i,\alpha}\hat{s}^{z}_{\alpha\beta}\hat{c}_{j,\beta} \\ &+ i\lambda_r \sum_{\langle ij\rangle\alpha\beta} \nu_{ij}\hat{c}^{\dagger}_{i,\alpha}\mathbf{s}\times\mathbf{d}_{ij}\ \hat{c}_{j,\beta} + \lambda_v \sum_i \xi\hat{c}^{\dagger}_i\hat{c}_i\end{aligned} \tag{1.27}$$

Here $\nu_{ij} = \mathbf{d}_i \times \mathbf{d}_j$, where these vectors are unit vectors lying in the direction of the two bonds which the electron traverses going from site i to site j. Here the complex hopping term of the Haldane model is replaced with a spin-dependent time-reversal symmetric spin-orbit term. We see that the above Hamiltonian implements complex hopping by acting on each spin-component with a conjugate interaction due to the

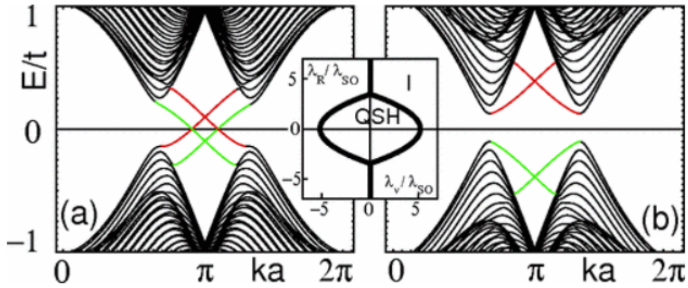

Figure 1.4: The band-structure of the Kane and Mele model in the quantum spin Hall state (left) and insulating state (right). The inset shows a phase diagram with relative strengths of the spin-orbit interaction λ_{SO}, Rashba spin-orbit λ_R and inversion symmetry breaking potential λ_v. Figure reproduced from [5].

$\hat{s}^z$ operator. The Hamiltonian commutes with s^z and we can therefore treat each spin-component completely separately. Here we also include the Rashba spin-orbit term with the coefficient λ_r and the staggered sublattice potential with coefficient λ_v.

The spinor wavefunction we use is $(\psi_{k,a,\sigma}, \psi_{k,b,\sigma})$. Here we include a spin index σ, but this is otherwise similar to the Haldane model. This can be most easily seen when the Rashba spin orbit term and staggered sublattice potential are excluded from the model, in which case the model can be formulated analogously to the Haldane model in k-space.

$$\begin{aligned}\hat{H}(\vec{k}) = t_1 &\left(\sum_i \left[\cos(\vec{k} \cdot \vec{a}_i) \boldsymbol{\sigma}_1 + \sin(\vec{k} \cdot \vec{a}_i) \boldsymbol{\sigma}_2 \right] \right) \\ &+ 2\sigma\lambda_{SO} \left(\sum_i \sin(\vec{k} \cdot \vec{b}_i) \right) \boldsymbol{\sigma}_3. \end{aligned} \tag{1.28}$$

Thus we may in this very clean system where time-reversal and inversion symmetry are both preserved describe this system as a spin-full Haldane model. Since the spin-orbit interaction here takes the role of the magnetic field in the Haldane model, the analogy is completed by considering each time-reversed partner experiencing the exact opposite Berry curvature and conjugate complex hopping amplitudes, which in this case is analogous to a reversed magnetic field.

The quantum Hall effect of this material is a spin-Hall effect, as there is no actual net charge current associated with it, but only a spin current. This is because each spin-component contributes an opposite charge current, since they carry like charges, but because their spins are opposite there is a finite net spin current. There is a $\mathcal{Z}_2$ topological invariant associated with this type of response, which is defined by considering a time-reversal polarization, which is analogous to the charge polarization of the flux-threading argument introduced by Laughlin. The filling factor of the integer quantum Hall effect determined exactly the change in charge polarization when a quantum of flux was introduced to that system. Likewise here, the $\mathcal{Z}_2$ topological invariant will tell us the change in time-reversal polarization.

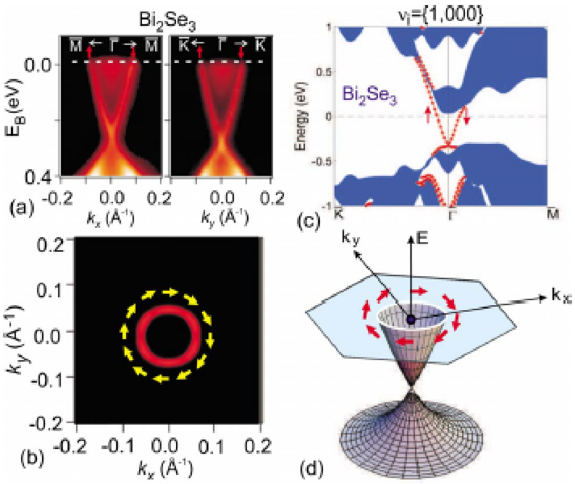

Figure 1.5: (a) ARPES data for Bi_2Se_3 with a spin-polarized Dirac cone. (b) Here the spin-polarization of the Fermi-surface is shown with its chiral texture. (c) Here the surface spectrum of Bi_2Se_3 has been computed with the local density approximation. (d) Generic dispersion of Bi_2X_3 class compounds with spin-polarized surface-states. Figure reproduced from [6].

If a time-reversal symmetry preserving Rashba spin-orbit term is introduced, then $\hat{s}^z$ is no longer conserved and equation (1.28) is no longer valid. The Laughlin argument can no longer be applied here either, as transport may no longer be described purely by the charge polarization. That being said there are still topological edge modes in the presence of perturbations, as long as they do not close the bulk band-gap. This is depicted on figure 1.4, where a phase diagram is included in an inset showing the transition between topologically trivial and non-trivial bands.

The quantum spin Hall effect and $\mathcal{Z}_2$ topological invariant have been under investigation in a wide variety of systems both theoretically [78–83] and experimentally [84–89] and the QSH state has been predicted to arise in several materials [90–92]. Similarly to the edge-states of the Chern insulator the quantum spin Hall helical edge modes have also been predicted to be dissipationless and robust towards local scattering potentials, although here the Krämers protection mechanism is responsible. This robustness has been studied theoretically as well [93].

A promising candidate for the realization of the spin-Hall topological insulator is Bi_2Se_3 and several variants thereof with different admixtures of Se [94–100]. Spin polarized angle resolved photo-emission spectroscopy (ARPES) has been used to demonstrate that the electronic band-structure of this material has a chiral spin-polarized Dirac cone (see figure 1.5). This is a hallmark of the quantum spin Hall state, since such a Dirac cone exhibits the features expected of a non-trivial dispersing band-structure with Krämers' pairs. Bismuth bilayers too have been proposed to support a quantum spin Hall state [101] and in the experiments by Sabater et. al., it was found that exfoliating these bilayers allowed the measurement of a Hall conductance plateaus at room temperature [102].

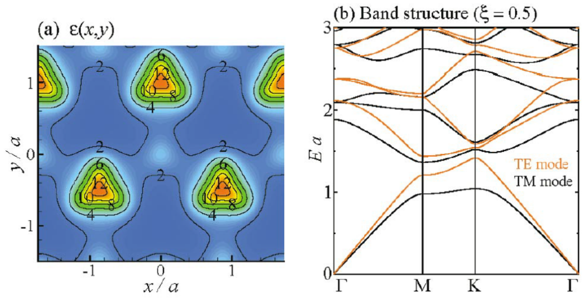

Figure 1.6: (a) Dielectric function $\epsilon(r)$ of a photonic crystal with a triangular unit cell. (b) Corresponding band structure of TE and TM modes. Figure reproduced from [7].

1.3 The universality of topological insultators

The topological band-structures discussed in electronic systems so far are remarkable due to the direct link between fundamental physics and topology, a link which is made unambiguous by the simplicity of the quantized Hall conductance seen in experiments. The physics of topological insulators is dual to many systems in nature, even where experimental results do not as clearly reveal fundamental physical constants. Some of these ideas have therefore opened up entire new fields in physics, whereas others provide surprising examples where topological invariants manifesting themselves in macroscopic systems.

In photonic systems, i.e. optically refracting materials which can be engineered to have a wide range of spatially non-constant refractive indeces $n(r)$, many of the same features seen in condensed matter systems reappear. Especially 2-dimensional waveguides, in which light is trapped by total internal reflection, have seen much research interest in recent years due to the freedom with which periodic structures can be engineered, as well as non-linear optics which introduce photon-photon interactions [18, 26, 54].

The Berry's connection for a photonic band in such a system is

$$[\Lambda_k]_{\lambda,\lambda'} = -i\vec{e}^{\dagger}_{\lambda k}\nabla_k\vec{e}_{\lambda' k}. \tag{1.29}$$

Here λ and λ' index the polarization of the photon as either clockwise or counter-clockwise circular, and $\vec{e}$ is a two-component unit vector describing the polarization of the photon. It has been shown by Onoda, Murakami and Nagaosa [7] that a photonic wave-guide with transverse electric (TE) and transverse magnetic (TM) Bloch bands has an associated Hall effect. Although it is not quantized it is anomalous in that it arises as a consequence of the Berry's curvature. Figure 1.6 shows the scalar dielectric permeability of the waveguide, which forms a triangular lattice. The resulting TE and TM modes have topological band-gaps due to the Berry's curvature, which here arises from a globally homogeneous gradient of the refractive index.

A very interesting example of a topological insulator is found in the vibrational modes of a LEGO structure as shown by [8]. As is well known LEGO bricks are a commodity allowing for play by construction of elaborate structures. Due to precise

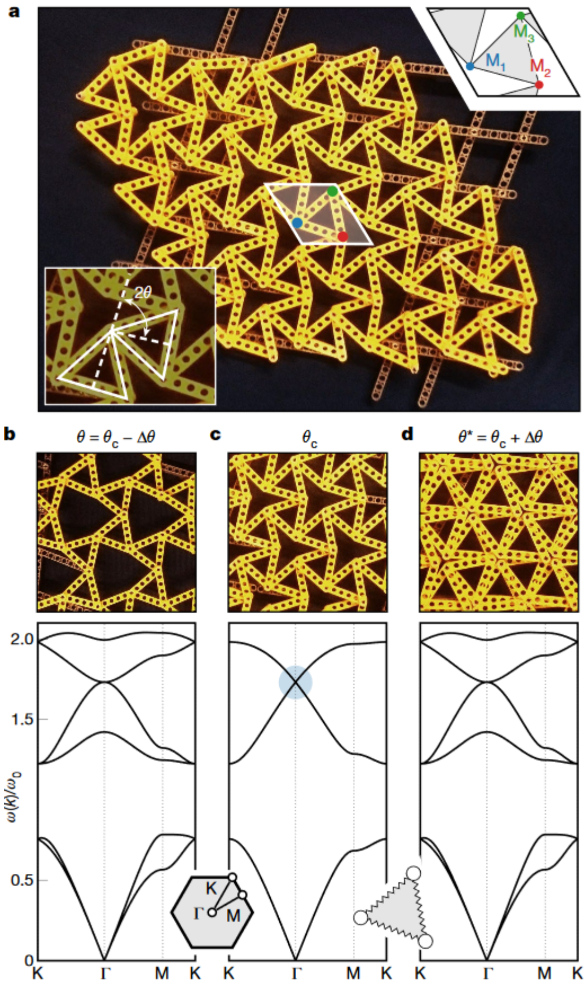

Figure 1.7: (a) A twisted kagome lattice built out of LEGO with a tunable twisting angle θ. (b) and (d) are dual points with identical vibrational modes. (c) The self-dual point which is found when the angle θ is halfway between two dual points such as (b) and (d). Here the vibrational spectrum is globally degenerate due to some hidden symmetry which arises at the self-dual point. At the Γ point a double Dirac cone appears. Figure reproduced from [8].

manufacturing of pieces with movable joints it is possible to build a structure such as the one seen in figure 1.7. Here it is modeling a twisted kagome lattice with a variable twisting angle.

The vibrational modes of this structure were calculated and as shown in figure 1.7, there is a duality transform defined by reflecting the twisting angle θ through some critical angle θ_c. Interestingly, if θ_c is chosen as the twisting angle, the band-structure of figure 1.7.c is obtained, which is globally doubly degenerate. This situation is similar to the Krämers' degeneracy of time-reversal invariant electron transport systems.

Here it is not time-reversal invariance which gives us a degenerate spectrum, but it is rather the duality transformation itself which the system is now invariant with respect to. Instead of spin degrees of freedom, we can think of this system as having two equivalent decompositions of its vibrational modes. In addition to this the spectrum has the usual three sublattices of the kagome lattice resulting in three bands in the non-interacting theory. The reason this LEGO structure is dual to a krämers' degenerate electron system is that the duality transform acting on the space of the vibrational modes is an anti-unitary matrix which commutes with the dynamical matrix of the system.

To complete this analogy, one may introduce inversion asymmetry without removing this duality transform symmetry. This introduces a topological band-gap at the dual Dirac cone of figure 1.7.c with a Hall effect dual to the spin-Hall effect of Kane and Mele [5] as well as topological edge modes.

There are many other interesting examples for the curious reader. Using classical Newtonian physics, Süsstrunk and Huber were able to show how a large lattice of coupled pendula exhibits helical edge-confined modes [24]. The topological protection of these modes is demonstrated. Another analogy is found in electronic circuits made up of RLC blocks. Here the Su-Schrieffer-Heeger model is reproduced with a topological band-gap [103].

1.4 Topological bands in magnets

As the previous examples show, it appears that topological insulators may be found in a wide range of physical systems beyond condensed matter. We now turn to the topologically insulating bands of magnetic excitations which are the focus of this thesis. As with photonic systems, magnetic excitations are bosonic in nature. Therefore the responses are not neatly quantized as they are in the electron transport literature, and in order to observe a Hall effect in a magnetic band excitation, it is enough that this band displays a Berry's curvature, not necessitating topologically non-trivial bands.

The magnon Hall effect was investigated by Katsura, Nagaosa and Lee in 2010 [33] who derived a transverse thermal Hall conductivity analogous to the TKNN formula. It took the form

$$\kappa^{xy} = -\frac{1}{2T}\Im\sum_{\alpha}\int_{BZ}\frac{d^2k}{(2\pi)^2}n_\alpha(\vec{k})\,\langle\partial_{k_x}u_\alpha(\vec{k})|(\mathcal{H}(\vec{k})+\omega_\alpha)|\partial_{k_y}u_\alpha(\vec{k})\rangle\,. \tag{1.30}$$

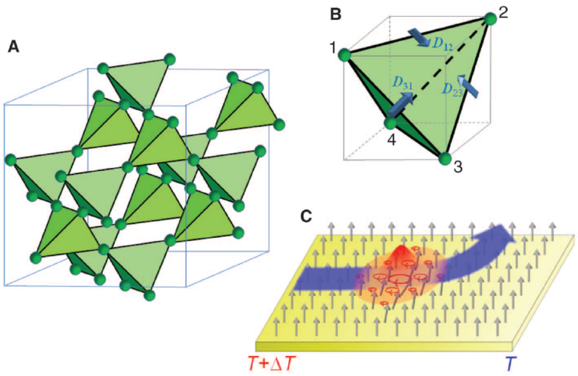

Figure 1.8: This graphic shows (A) the unit cell of $Lu_2V_2O_7$ which is composed of cornersharing tetrahedra. (B) The symmetry allowed orientation of the Dzyaloshinskii-Moriya interaction vector $\mathbf{D}_{i,j}$, which facilitates anti-symmetric exchange between spins i and j. (C) The magnon Hall effect. A wave-packet of magnons is deflected by the Dzyaloshinskii-Moriya interaction which here takes on the role of a vector potential. Figure reproduced from [9].

Here $n_\alpha(\vec{k}) = (1 - e^{\beta\omega_\alpha(\vec{k})})$ is the Bose distribution. This is in contrast to the TKNN expression, which assumes a band gap with a Fermi energy. At low temperatures the lower bands are therefore assumed to be filled completely with the upper bands being empty.

In the bosonic case here however, the Bose-distribution allows a much more complicated response. The above expression does not reduce to an unweighted integral over a Berry's curvature and will therefore be non-zero in general, even when the bands are topologically trivial. An important conclusion is therefore that the presence of a thermal Hall response does not necessarily imply topologically non-trivial bands or topological edge modes.

The existence of a magnon Hall effect was verified by Onose et. al. that same year [9] in $Lu_2V_2O_7$. This was supplemented by a theoretical analysis which showed that the Dzyaloshinskii-Moriya interaction affects the magnons of the spin-wave Hamiltonian in much the same way as the tight-binding electrons of the Haldane model are affected by a vector potential.

This can be seen by writing out the Hamiltonian in its spin-wave expansion. Similarly to the tight-binding model, we now have a hopping Hamiltonian, where matrix elements describe the on-site energy in case of diagonal terms and hopping amplitudes otherwise. Hopping of a magnon from site i to j can be written as

$$\begin{aligned}\langle i| - J\vec{S}_i \cdot \vec{S}_j + D_{i,j} \cdot (\vec{S}_i \times \vec{S}_j)_z |j\rangle &= \langle i| \frac{-J + iD}{2} (S_i^+ S_j^- + S_i^- S_j^+) |j\rangle \\ &= -\frac{\tilde{J}}{2} e^{i\phi_{i,j}}. \end{aligned} \tag{1.31}$$

Thus we see the reappearance of a complex hopping similar to the Haldane model. As such the Dzyaloshinskii-Moriya interaction can be thought of as a type of orbital magnetism arising due to spin-orbit coupling.

It was later argued by Matsumoto and Murakami [34] that the rotational motion as well as orbital motion of a magnon wave-packet would have an influence on its thermal Hall response. Their argument is based on semi-classical equations of motion. The center of mass coordinates of a wave-packet in real and reciprocal space are related by

$$\begin{aligned}\dot{\mathbf{r}}_n &= \frac{1}{\hbar}\frac{\partial \epsilon_{n,k}}{\partial \mathbf{k}} - \dot{\mathbf{k}} \times \mathbf{\Omega}_n(\mathbf{k}) \\ \hbar \dot{\mathbf{k}} &= -\nabla U(\mathbf{r}).\end{aligned} \tag{1.32}$$

The edge of the sample is modeled with a confining potential. Thus it is seen here that the Berry's curvature takes on the role of the Lorentz force with skipping cyclotron orbits appearing due to it at the edge of the sample in analogy to the electron. Another effect of the Berry's curvature is to cause the wavepacket to rotate. At mesoscopic scales, the wavepacket can be thought of as an area of the sample in which magnetic moments are canted with respect to one-another. Such canting is associated with the appearance of an electric polarization in duality to the appearance of magnetic dipoles due to rotating electric charges. It thus induces orbital angular momentum onto itself through its rotation. This orbital motion can also be taken into account as a deviation of the current operator in the linear response theory.

The full derivation may be found in [35]. It arrives at a corrected thermal Hall coefficient

$$\kappa^{xy} = \frac{2k_B^2 T}{\hbar V} \sum_{n,\mathbf{k}} c_2(\rho_n)\Omega_{n,k}. \tag{1.33}$$

Here

$$c_2(\rho) = (1+\rho)(\log\frac{1+\rho}{\rho})^2 - (\log\rho)^2 - 2\mathrm{Li}_2(-\rho). \tag{1.34}$$

For magnons the above equations show that topological invariants are not necessary to guarantee a thermal Hall effect. Here it arises from a finite Berry's curvature which may arise on a single band. The contributions from this band are weighted by a Bose factor and therefore even when the Chern number is zero a finite response may arise.

However, the band topology of magnons has been investigated too, and it was argued by Shindou [36, 37] that topological band-gaps in magnonic crystals should be accompanied with protected topological edge modes. The Chern number is defined for the generalized Bogoliubov de Gennes (BdG) Hamiltonian which must be considered when anti-ferromagnetic order is studied.

The Hamiltonian considered by Shindou is the generalized generic BdG Hamiltonian

$$\hat{H} = \frac{1}{2}\sum_k [\beta_k^\dagger, \beta_{-k}]\mathbf{H}_k \begin{bmatrix}\beta_k \\ \beta_{-k}^\dagger\end{bmatrix} \tag{1.35}$$

Here it is defined for some n-sublattice model reflected by the length of each vector

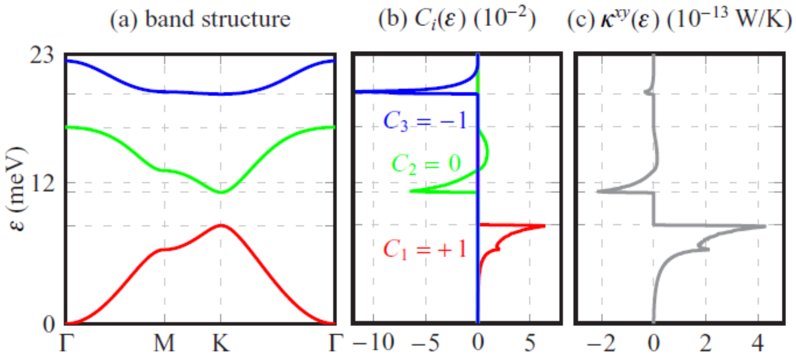

Figure 1.9: Topologically non-trivial magnon bands of the kagome magnet with Dzyaloshinskii-Moriya interaction is shown here. (a) The dispersion relation with high symmetry points indicated. (b) The Chern numbers are indicated as well as the Berry's curvature of each band. (c) Here the contributions of each band per unit energy to the transverse conductance is shown. Figure reproduced from [10].

β_k. The matrix $\mathbf{H}_k$ will then contain four $n \times n$ sub-matrices and be of the form

$$\mathbf{H}_k = \begin{bmatrix} a_k & b_k \\ b^*_{-k} & a^*_{-k} \end{bmatrix}. \tag{1.36}$$

The anomalous b_k matrices describe particle-particle and hole-hole channels, which are necessary when considering for instance an anti-ferromagnetically ordered state. Due to their appearance in the BdG Hamiltonian the solution must be obtained by a para-unitary transformation (see Chapter 2).

Shindou shows how one may calculate the Chern numbers of a magnonic wave-function after obtaining the correct para-unitary transformation and constructs a topological phase-diagram for the dipolar magnetic thin-film of an iron-YIG magnonic crystal.

In Mook's 2014 paper [104] the appearance of topological edge modes is investigated on a kagome magnet which is cut into a loop like geometry similarly to the argument by Laughlin. The quantum edge modes are obtained by explicit calculation of the semi-infinite geometry. This also allows the authors to show the appearance of hybridized topological modes, which are composed of the trivial edge modes, when their energy is such that they lie in the band-gap. In the same year the thermal Hall effect of topologically non-trivial bands in such systems was investigated in detail as well [10]. In figure 1.9 the thermal Hall effect of a kagome magnet is reproduced. It shows how the distribution of Berry's curvature in energy-space contributes to the thermal Hall coefficient. Notably, because the response is weighted by a temperature dependent Bose-distribution, there is a gradual decreasing dependence on the Berry's curvature at higher energies. On the experimental side, it is now possible to resolve the thermal Hall effect of magnons down to the switching of the Berry's curvature between bands [105, 106]. Topological bands can arise from interactions of magnon bound states [107] or material strain [108, 109], and a number of studies have described instances of the magnon thermal Hall effect [110, 111]. There are

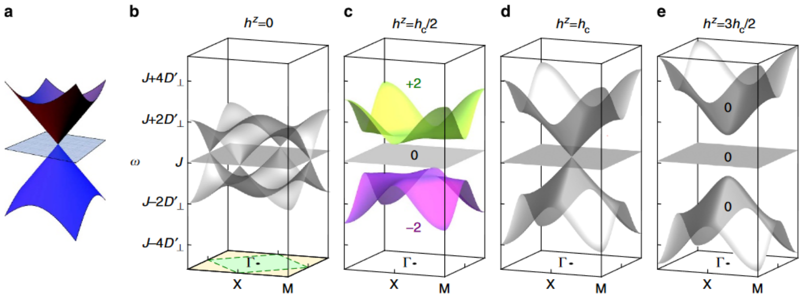

Figure 1.10: The triplon band-structure of $SrCu_2(BO_3)_2$ with Dzyaloshinskii-Moriya interaction. On figure (a) is depicted a generic spin-1 Dirac cone with all three bands touching. A transition between distinct topological phases can be identified by a band-touching transition, in which this cone appears at high symmetry points (b) - (e). The bands are tuned by an applied magnetic field, which acts differently on the $s_z = \pm 1$ components of the spin-space, thus breaking the degeneracy of the model at high symmetry points. Figure reproduced from [11].

now studies which speculate about the use of topological magnons in spintronics based on the Shastry-Sutherland lattices [112–114] and finally even $\mathcal{Z}_2$ topological insulators have been discussed [13, 115, 116].

The dimerized quantum paramagnet $SrCu_2(BO_3)_2$ has also been investigated for its topological excitations [11, 117]. This material is to a very good approximation an ideal quantum dimer magnet [118–121] as it only has small finite anisotropic interactions in the form of Dzyaloshinskii-Moriya. The ground state of such a magnet is a product state of dimer singlets, where each unit cell has one such bond. Thus, possible excitations in such a system come from the triplet levels of those bonds. These are in general dispersive and are referred to in the literature as triplons [122–126].

It was shown through an application of bond-wave theory, a generalized treatment of magnetic band-theory, that the topology of the resulting band-structure could be tuned by application of a magnetic field to have distinct Chern numbers [11]. These bands carry a thermal Hall effect similar to conventional ordered magnets, but since the ground state does not break time-reversal symmetry, an applied magnetic field is here required to engineer such a response.

In figure 1.10 the tuning of this model between distinct topological phases is depicted. The bands acquire a finite Berry's curvature as soon as time-reversal symmetry is broken. As the field approaches a critical value h_c, which is determined by the strength of the Dzyaloshinskii-Moriya interaction, the bands touch and form a trivial band structure. Interestingly the breaking up of the spin-1 Dirac cone into topologically non-trivial bands results in Chern numbers $c = \pm 2$.

In addition to the magnon and triplon Chern insulator, bilayer materials have been proposed for the realization of a magnetic $\mathcal{Z}_2$ topological insulator. The classically ordered stacked honeycomb lattice with a pseudo time-reversal symmetry was a first example of this [127–129]. Recently an example has been proposed which uses the triplon excitations of a quantum paramagnet on a bilayer honeycomb magnet [130]. It is worth mentioning also that topological magnons have been envisioned to have applications in hybrid excitations [131, 132] and as accomplices in chiral phonon transport [133, 134] as well as analogues to Weyl magnons [135–137].

1.5 Conclusion

In this chapter we have briefly reviewed the history of topological insulators, starting with the quantum Hall effect and following the theoretical developments from the vantage point of electronic insulators. We have described how these ideas carry over to a wide class of materials and how transport theories were developed in the field of magnetic insulators.

The quantum Hall effect caught the attention of the physics community because there was clearly a connection between fundamental physics and macroscopic measurable quantities that hadn't yet been understood. A physical response which was quantized in units of fundamental constants required entirely new insights to properly understand. These were provided by gauge invariance and topologically invariant transport equations. With the band-gaps of these systems were also associated topological edge modes.

Lattice models which combined all of these features were later explored. They would for the first time explicitly discuss the role of symmetries in relation to the appearance of topological invariants. Thus a more systematic classification of topological insulators became possible. The lattice models of Haldane and Kane and Mele are dual to the magnetic insulators discussed later in this thesis.

Heat transport in magnets with insulating magnon bands is subject to a Hall effect which has been investigated theoretically and experimentally. However, with Bose-statistics there is no quantized response, which depends on the filling of topologically non-trivial bands. Indeed, even topologically trivial magnon bands may still support a thermal Hall response, as long as there is a finite Berry's curvature. One of the central questions of this thesis is therefore whether or not other signatures of topological bands exist that more directly reveal the topology.

An interesting feature of magnetic insulators is that the types of excitations that may appear depend on their ground-state structure. An example of this is the triplon excitation which is a dispersive excited state that appears in certain quantum disordered magnets. These carry spin degrees of freedom as well as energy, and have been shown to realize a magnetic analogue of the Kane and Mele model. This leads to the other main topic in this thesis, namely the triplon $\mathcal{Z}_2$ topology and the validity of this topological phase of matter in a bilayer kagome magnet.

In Chapter 2 we will elaborate in more detail on magnetic insulators and their band-theory. We will show how the Pauli exclusion principle together with Coulomb repulsion gives rise to the anti-ferromagnetic Heisenberg interaction in magnetic insulators. From here we will describe certain dispersive magnetic excitations including magnons and some more non-trivial ones. We will conclude with some worked examples.

In Chapter 3 we will give a more complete treatment of topological excitations. This allows us to understand the appearance of topological-edge modes as well as give a theoretical description of the topological band-gap as a consequence of the non-trivial parametrization of the wave-function in k-space. We will also here introduce the pseudo-time-reversal operator and discuss how it is needed to protect a $\mathcal{Z}_2$ topological phase.

In Chapter 4 we review our work on the bilayer kagome interlayer antiferromagnet. We describe this lattice from a dimer singlet ansatz in which the dimers connecting each layer is in a singlet state in the ground state. We describe the allowed interactions and show that when bond-nematic interactions are accounted for, the $\mathcal{Z}_2$ topology is destroyed.

In Chapter 5 we show that there is a link between magnon band-topology and half-moon neutron scattering features in field aligned kagome. This connection is shown by constructing a representation theory for the $D_{6h}(C_{6h})$ magnetic point group on the space of magnon wave-functions. This gives us a way to analyze the symmetry allowed components of the spin-wave Hamiltonian and thereby show that both topological bands and half-moons arise as a natural consequence of the lattice symmetry.

Chapter 2

Quantum magnets and their band-like excitations

Before discussing the topology of band-like magnetic excitations, we will in this chapter elaborate on their origin and various ways they manifest in materials with exchange interaction. We will begin by elaborating on the Mott-insulating state and explain the origin of the exchange interaction. This is followed by a treatment of spin-wave excitations in magnetically ordered materials. We generalize upon this by describing the triplet excitations of a magnetically disordered quantum paramagnet. This is then followed by a brief introduction to representation theory, where we elaborate on some of the representations we will use in the rest of this work.

2.1 Mott-insulators and magnets

After its inception, the conventional band-theory of electrons was quickly recognized to have great predictive power regarding the conductivity of certain materials. It seemed to give a minimum criterion for a material to be conductive, namely that the Fermi level would intersect the bands or be near enough to them that conduction electrons and holes would be thermally excited.

There are certain phases where band-theory alone cannot account for whether or not a material is conductive. An example of this is the well-known insulator CoO [138]. If only band-theory without the Coulomb interaction between electrons is taken into account, CoO would be classed as an insulator. Below we present the Hubbard model, which gives an intuitive way to introduce such interactions through a second quantized representation of localized orbitals.

The Hubbard model is a tight-binding model of electrons with an added Coulombic interaction term.

$$\hat{H} = -t \sum_{\langle i,j \rangle} \sum_{\sigma} (\hat{c}^{\dagger}_{j\sigma} \hat{c}_{i\sigma} + \text{H. c.}) + U \sum_{i} \hat{n}_{i\uparrow} \hat{n}_{i\downarrow} + \epsilon_{\text{at}} \sum_{i} \hat{n}_{i}. \tag{2.1}$$

Here the Hamiltonian is written using fermionic field operators $\hat{c}^{\dagger}_{i}$ ($\hat{c}_{i}$), which create (annihilate) a Wannier state around site i. The Wannier basis is a set of position

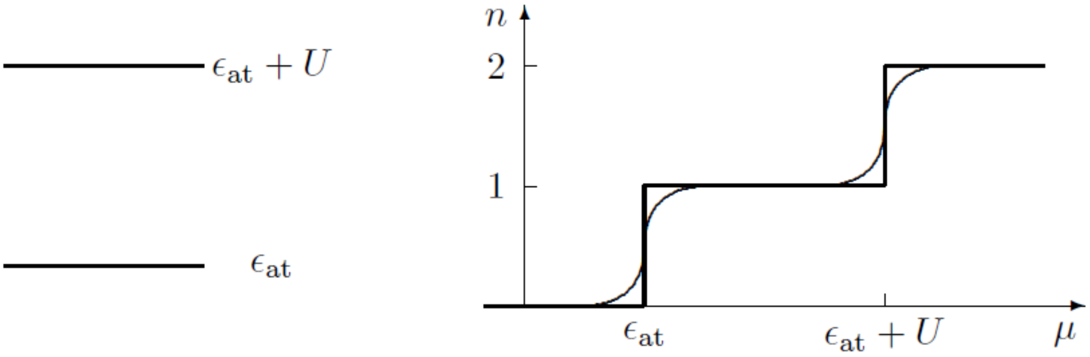

Figure 2.1: This image shows (left) the energy levels in the atomic limit of the Hubbard model in terms of the onsite energy. (Right) the average band-occupation at a given chemical potential. Figure reproduced from [12].

localized states. They are defined as the Fourier transform of the electronic Bloch band $\psi_k(\vec{r})$ [139],

$$\phi_R(\vec{r}) = \frac{1}{\sqrt{N}} \sum_k e^{-ik \cdot R} \psi_k(r). \tag{2.2}$$

Here the gauge of $\psi_k(r)$ is chosen so as to maximally localize $\phi_R(r)$. The reason the Wannier basis is chosen is that it provides a convenient basis to express short range interactions, which can here be expressed through the Hubbard interaction U.

The field operators obey the following commutation rules

$$\begin{aligned} \{\hat{c}_i, \hat{c}_j^\dagger\} &= \delta_{i,j} \\ \{\hat{c}_i, \hat{c}_j\} &= \{\hat{c}_i^\dagger, \hat{c}_j^\dagger\} = 0, \end{aligned} \tag{2.3}$$

and the number operators are

$$\hat{n}_{i,\sigma} = \hat{c}_{i,\sigma}^\dagger \hat{c}_{i,\sigma}. \tag{2.4}$$

ϵ_{at} is the Fourier transformed band energy, now expressed as an onsite potential energy. U is the on-site averaged Coulomb potential, which can be calculated as

$$U = \int d\vec{r}_1 \int d\vec{r}_2 |\phi(\vec{r}_1)|^2 |\phi(\vec{r}_2)|^2 \frac{e^2}{|\vec{r}_1 - \vec{r}_2|}. \tag{2.5}$$

The importance of U lies in stabilizing an insulating phase, known as the Mott-insulating phase. U introduces a step-like energy distribution that plateaus at integer site-fillings. In the limit of $U \gg t$, as soon as each site is filled, the energy cost of adding another electron is approximately U. We can define the free energy Hamiltonian

$$\hat{F} = \hat{H} - \mu \sum_i \hat{n}_i. \tag{2.6}$$

Now, tuning the chemical potential μ, we can add or remove particles to the system.

The first barrier to adding single particles to the system is the onsite potential ϵ. When μ is comparable in magnitude, the electronic bands of the system will start to get filled until $\langle \hat{n} \rangle = 1$.

This is the lowest Mott sub-band. There is a gap to further excitations which depends on the value of U. The Mott-insulating phase occurs when this band is completely filled. This is because although the single-band picture would here tell us that the electrons are dispersive, they are pinned due to the onsite interaction, which acts as a barrier preventing hopping. This now describes why materials such as CoO whose bands are half-filled, have a gap to excitations which cannot be seen by a band-theory that does not take interactions into account.

This situation is illustrated in figure 2.1. In the atomic limit ($t/U \sim 0$) the energy depends only on the occupation number of each site. Here there is a gap between states with $\langle \hat{n} \rangle = 1, 2$ of size U. While the lower band is partially filled or empty, addition of an electron costs ϵ_{at}. We can imagine the lower band being completely filled when $\mu > \epsilon_{\text{at}}$ after which the cost of adding an electron is $\epsilon_{\text{at}} + U$. Now, increasing the hopping amplitude t introduces dispersion to the picture. The sub-bands are broadened in a fashion similar to what is illustrated in figure 2.1. The thin line does not come from an exact calculation of the band structure, but shows qualitatively the result of a finite energy gain caused by the kinetic term. While a subband is partially filled the electrons can hop, but in the completely filled $\langle n \rangle = 1$ state the kinetic term vanishes as $\langle \hat{c}_i^\dagger \hat{c}_j + \text{H. c.} \rangle = 0$. This is the Mott-insulating phase [12].

If t is comparable to U the Mott-insulating phase may break down, as the kinetic term may be large enough to connect the bands. Interestingly, there is a broad range of values of t/U for which the Mott-insulating phase persists at half-filling. In this phase the bulk conductivity of the material vanishes, but as we show below, this can give rise to antiferromagnetic ordering.

We can derive an effective spin Hamiltonian in the following way. First we will consider two neighboring sites in the Mott-insulating phase. The full Hilbert space of this two body problem is then spanned by the states

$$\begin{aligned}
|\uparrow\downarrow, 0\rangle &= \hat{c}_{1\downarrow}^\dagger \hat{c}_{1\uparrow}^\dagger |0\rangle \\
|\uparrow, \uparrow\rangle &= \hat{c}_{1\uparrow}^\dagger \hat{c}_{2\uparrow}^\dagger |0\rangle \\
|\uparrow, \downarrow\rangle &= \hat{c}_{1\downarrow}^\dagger \hat{c}_{2\uparrow}^\dagger |0\rangle \\
|\downarrow, \uparrow\rangle &= \hat{c}_{1\downarrow}^\dagger \hat{c}_{2\uparrow}^\dagger |0\rangle \\
|\downarrow, \downarrow\rangle &= \hat{c}_{1\downarrow}^\dagger \hat{c}_{2\downarrow}^\dagger |0\rangle \\
|0, \uparrow\downarrow\rangle &= \hat{c}_{2\downarrow}^\dagger \hat{c}_{2\uparrow}^\dagger |0\rangle
\end{aligned} \tag{2.7}$$

In the $t = 0$ limit, the four singly occupied states are degenerate ground-states. We can now include the hopping through perturbation theory. To first order this gives us a basis of perturbed states

$$\begin{aligned}
|\uparrow,\uparrow\rangle^{(1)} &= |\uparrow,\uparrow\rangle \\
|\uparrow,\downarrow\rangle^{(1)} &= |\uparrow,\downarrow\rangle + \frac{t}{U}\big(|\uparrow\downarrow,0\rangle + |0,\uparrow\downarrow\rangle\big) \\
|\downarrow,\uparrow\rangle^{(1)} &= |\downarrow,\uparrow\rangle - \frac{t}{U}\big(|\uparrow\downarrow,0\rangle + |0,\uparrow\downarrow\rangle\big) \\
|\downarrow,\downarrow\rangle^{(1)} &= |\downarrow,\downarrow\rangle
\end{aligned} \tag{2.8}$$

The above form is needed, since without the double-occupancy correction to the ground state, the spins are effectively non-interacting. However, in this basis we can calculate the matrix elements of the Hubbard Hamiltonian as

$$\begin{aligned}
{}^{(1)}\langle\uparrow,\downarrow|\hat{H}|\uparrow,\downarrow\rangle^{(1)} &={}^{(1)}\langle\downarrow,\uparrow|\hat{H}|\downarrow,\uparrow\rangle^{(1)} = -2t^2/U \\
{}^{(1)}\langle\uparrow,\downarrow|\hat{H}|\downarrow,\uparrow\rangle^{(1)} &={}^{(1)}\langle\downarrow,\uparrow|\hat{H}|\uparrow,\downarrow\rangle^{(1)} = 2t^2/U.
\end{aligned} \tag{2.9}$$

The diagonal terms above can be expressed as

$$\hat{H}_{\text{diag}} = -2\frac{t^2}{U}\big(1/2 - 2\hat{S}_i^z\hat{S}_j^z\big). \tag{2.10}$$

The off-diagonal terms can be expressed through spin raising and lowering operators as

$$\hat{H}_{\text{off}} = 2\frac{t^2}{U}\big(\hat{S}_i^+\hat{S}_j^- + \hat{S}_i^+\hat{S}_j^-\big). \tag{2.11}$$

They will have the usual commutator

$$[\hat{S}_i^+, \hat{S}_j^-] = 2\delta_{i,j}\hat{S}_i^z \tag{2.12}$$

Taken together this can be expressed as the effective Hamiltonian

$$\hat{H} \approx 4\frac{t^2}{U}(\vec{S}_i \cdot \vec{S}_j - 1/4). \tag{2.13}$$

This is the isotropic Heisenberg Hamiltonian, which accounts for spin interactions in magnetically ordered Mott-insulators. It is noteworthy that this arises purely from the Hubbard interaction U, which is a Coulomb potential, and the Fermionic statistics of the electron, which prevent hopping from the $|\uparrow,\uparrow\rangle$ and $|\downarrow,\downarrow\rangle$ states. U is necessarily positive, and because of this the Mott insulator in the half-filling limit results in an anti-ferromagnetic interaction.

In this derivation, because we have only allowed for a single electronic orbital, the resulting exchange interaction must have a positive interaction strength $J = 4\frac{t^2}{U}$. However, effective exchange models similar to this may be derived while taking orbital degrees of freedom into account, in which case $J < 0$ is also possible [12].

In the following we will briefly visit the ferromagnetic Heisenberg model with

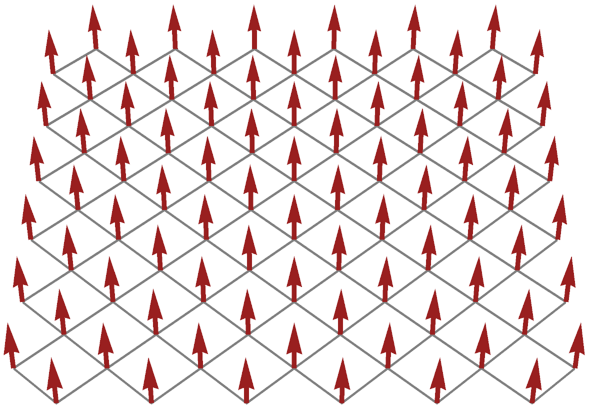

Figure 2.2: A depiction of ferromagnetic order on the square lattice. Spins are represented by arrows.

$J < 0$ to give an illustrative introduction into spin-wave theory. We will then shift our focus back to $J > 0$ models for the remainder of this chapter.

2.2 Spin-waves

In this section we follow closely the treatment of [12]. The nearest neighbor Heisenberg Hamiltonian is

$$\hat{H} = J \sum_{\langle i,j \rangle} \vec{S}_i \cdot \vec{S}_j. \tag{2.14}$$

Considering first the ferromagnetic case with $J < 0$, the ground state of this model is obtained when all spins are oriented the same, as seen in figure 2.2. With L being the number of sites in the system, there are $2LS + 1$ different spin-states which satisfy this rule, and they only differ in the orientation of the collective spin. When calculating quantities such as the magnetization this poses an interesting problem. Since statistical mechanics tells us that each orientation ought to be weighted with equal probability, we might make the naive conclusion that the magnetization is

$$m = \langle m \rangle = 0. \tag{2.15}$$

In practice, the statistical mechanics of spontaneously ordered magnets has an important caveat. The $2LS + 1$ ground states are many spin-flips removed from each other, and in the thermodynamic limit, no finite amount of changes to single spins will connect a pair of them.

Even in a small finite lattice, the probability of a random walk from one ground state arriving at another implies first taking a path through several excited states, which implies a transition probability that tends exponentially to zero with system size (except for 1-dimensional spin-chains). Because of this the ground state is very stable, and the magnetization is not going to drift.

The approach is now to select one of these ground states and consider transitions to low-lying excitations around this state obtained by a small number of spin-flips.

In general such excitations are dispersive. They manifest as waves in the magnetization density, and are referred to as spin-waves. A single quantum of these waves is referred to as a magnon.

For convenience the $\langle \hat{S}^z \rangle = S$ state is typically chosen to be the ground state. We define second quantized magnon creation and annihilation operators $\hat{a}_j^\dagger$ and $\hat{a}_j$, where j is an index selecting the jth site, we have the commutation relations

$$\left[\hat{a}_j, \hat{a}_i^\dagger\right] = \delta_{i,j}, \quad \left[\hat{a}_j, \hat{a}_i\right] = \left[\hat{a}_j^\dagger, \hat{a}_i^\dagger\right] = 0. \tag{2.16}$$

Due to how we have defined the ground state, the magnons will be $\hat{S}^z$ eigenstates. In terms of the magnon creation and annihilation operators

$$\hat{S}_j^z = S - \hat{a}_j^\dagger \hat{a}_j. \tag{2.17}$$

Now the objective is to be able to express the spin raising and spin lowering operators $\hat{S}_j^+$ and $\hat{S}_j^-$ in terms of $\hat{a}_j^\dagger$ and $\hat{a}_j$ while keeping the angular momentum algebra consistent. One must consider that

$$\begin{aligned} S(S+1)\left|m\right\rangle &= \vec{S}_j^2 \left|m\right\rangle & (2.18)\\ &= \frac{1}{2}(\hat{S}_j^+ \hat{S}_j^- + \hat{S}_j^- \hat{S}_j^+)\left|m\right\rangle + m^2 \left|m\right\rangle. & (2.19)\\ &= \frac{1}{2}(\hat{S}_j^+ \hat{S}_j^- + \hat{S}_j^- \hat{S}_j^+)\frac{1}{\sqrt{n}}(\hat{a}_j^\dagger)^n \left|0\right\rangle + (S-n)^2 \frac{1}{\sqrt{n}}(\hat{a}_j^\dagger)^n \left|0\right\rangle. & (2.20) \end{aligned}$$

In the last equality we have here switched from the $\hat{S}^z \left|m\right\rangle = m\left|m\right\rangle$ basis to the second quantized representation of the magnon.

In order to fulfill the above requirement, and requiring that $\hat{S}^- = (\hat{S}^+)^\dagger$ we must have

$$\begin{aligned} \hat{S}_i^+ &= \sqrt{2S}\left(1 - \frac{\hat{a}_i^\dagger \hat{a}_i}{2S}\right)^{1/2} \hat{a}_i \\ \hat{S}_i^- &= \sqrt{2S}\hat{a}_i^\dagger \left(1 - \frac{\hat{a}_i^\dagger \hat{a}_i}{2S}\right)^{1/2}. \end{aligned} \tag{2.21}$$

This is the well-known Holstein-Primakoff transformation of linear spin-wave theory. Utilizing this language the Hamiltonian can be written in second quantized notation up to any desired order in S. Typically a Taylor-expansion of the square-root term is performed around the state with $\langle \hat{a}^\dagger \hat{a} \rangle = 0$. To first order

$$\left(1 - \frac{\hat{a}_i^\dagger \hat{a}_i}{2S}\right)^{1/2} \approx \left(1 - \frac{\hat{a}_i^\dagger \hat{a}_i}{4S}\right). \tag{2.22}$$

The appearance of the $1/S$ term gives us a way to express fluctuations about the ground state. The single-particle picture of a magnon is only valid up to small fluctuations in the ground state, where this term is small. When the system is sufficiently thermally excited the magnon picture loses its meaning and we can no longer

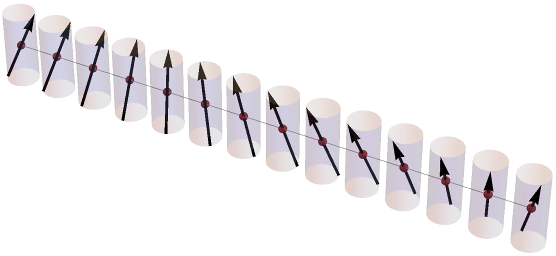

Figure 2.3: A depiction of a magnon on a one-dimensional lattice. This is the Bloch-wave associated with a dispersive spin-flip excitation on a magnetically ordered lattice.

expect this expansion to be valid.

Translationally invariant models may be solved with Bloch waves. We therefore introduce the Fourier transformed operators

$$\begin{aligned}\hat{b}^{\dagger}_{\vec{k}} &= \frac{1}{\sqrt{L}}\sum_{\vec{j}} e^{-i\vec{k}\cdot\vec{j}}\hat{a}^{\dagger}_{\vec{j}} \\ \hat{b}_{\vec{k}} &= \frac{1}{\sqrt{L}}\sum_{\vec{j}} e^{i\vec{k}\cdot\vec{j}}\hat{a}_{\vec{j}}\end{aligned} \tag{2.23}$$

If the only interaction of the given model is a nearest neighbor spin-exchange term as in equation (2.14) then the Hamiltonian can be written as

$$\hat{H} = -\frac{1}{2}JzS^2L + \frac{JzS}{2}\left[2\hat{b}^{\dagger}_{\vec{k}}\hat{b}_{\vec{k}} - (\gamma_{\vec{k}} + \gamma_{-\vec{k}})\hat{b}^{\dagger}_{\vec{k}}\hat{b}_{\vec{k}}\right] + \mathcal{O}(1/S). \tag{2.24}$$

Here z is the coordination number and

$$\gamma_{\vec{k}} = \frac{1}{z}\sum_{\vec{\delta}} e^{i\vec{\delta}\cdot\vec{k}}. \tag{2.25}$$

$\vec{\delta}$ is here the vector displacement between two spins.

It is thus fairly straightforward to diagonalize the linear spin-wave Hamiltonian of a ferromagnetic material. Interestingly the dispersion becomes

$$\omega_{\vec{k}} = -JzS\left[1 - (\gamma_{\vec{k}} + \gamma_{-\vec{k}})/2\right]. \tag{2.26}$$

In the long-wavelength limit this is quadratic in $|\vec{k}|$.

Due to the formulation of $\hat{b}_{\vec{k}}$ we can think of the $\vec{k} \sim 0$ state as an equally distributed single-magnon over the whole lattice. This is equivalent to application of the spin lowering operator to the global spin, which does not incur an energy cost as the Hamiltonian is symmetric with respect to changes to the orientation of the total magnetic moment.

This is in fact the famous Goldstone mode, also known as the symmetry restoring

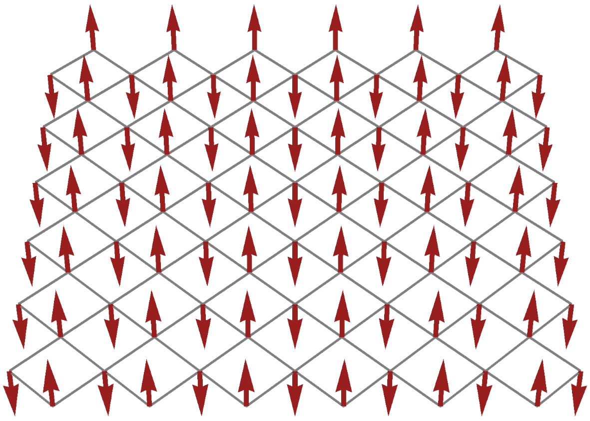

Figure 2.4: The antiferromagnetic state on the square lattice.

mode of the lattice. It occurs as a consequence of the spontaneous breaking of the global $SU(2)$ symmetry of the Heisenberg model [12].

2.2.1 Anti-ferromagnets

In the preceding discussion the Heisenberg model was expanded around a ferromagnetically ordered ground state. This is a true ground state of that Hamiltonian even including quantum fluctuations. However, with $J > 0$, this approach is no longer valid. We consider here a bipartite lattice with antiferromagnetic order as depicted in figure 2.4.

The difficulty in determining the ground state arises from quantum fluctuations. A single pair of $S = 1/2$ magnetic ions form a singlet in the ground state. This minimizes its energy through the spin-flip terms

$$\hat{S}_i^+ \hat{S}_j^- + \text{H. c.}. \tag{2.27}$$

The Néel state is not an eigenstate of this operator, so the true ground state must contain some quantum fluctuation. These effects are most relevant for small spins and the relative correction to the ground state energy is $\mathcal{O}(1/S)$.

If the Hamiltonian is expanded around the Néel state, two Holstein-Primakoff bosons are needed. On sublattice A it is $\hat{S}^-$ which lowers the spin and thereby creates a magnon. On sublattice B the spin has to be increased by $\hat{S}^+$ in order to create a magnon. This is expressed as

$$\hat{S}_A^+ = \sqrt{2S}\left(1 - \frac{\hat{a}^\dagger \hat{a}}{2S}\right)^{1/2} \hat{a} \qquad \hat{S}_A^- = \sqrt{2S}\hat{a}^\dagger \left(1 - \frac{\hat{a}^\dagger \hat{a}}{2S}\right)^{1/2} \tag{2.28}$$

$$\hat{S}_B^+ = \sqrt{2S}\hat{b}^\dagger \left(1 - \frac{\hat{b}^\dagger \hat{b}}{2S}\right)^{1/2} \qquad \hat{S}_B^- = \sqrt{2S}\left(1 - \frac{\hat{b}^\dagger \hat{b}}{2S}\right)^{1/2} \hat{b}. \tag{2.29}$$

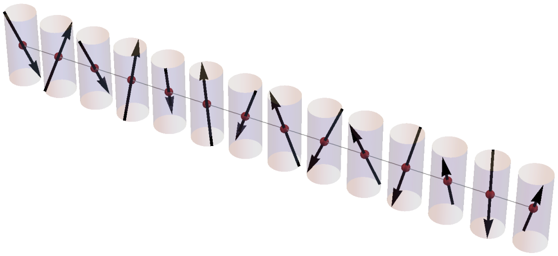

Figure 2.5: A magnon is depicted here as a linear combination of two sublattice bosons.

The propagating single-particle bosonic operators are then

$$\hat{c}_k^\dagger = \sqrt{\frac{2}{L}} \sum_{j \in A} e^{-ik\cdot j} \hat{a}_j^\dagger \tag{2.30}$$

$$\hat{d}_k^\dagger = \sqrt{\frac{2}{L}} \sum_{j \in B} e^{-ik\cdot j} \hat{b}_j^\dagger . \tag{2.31}$$

Both sublattices together now form the repeating unit cell of the lattice, and therefore the Bloch-waves will be formed by some linear combination of the above states. But k remains a good quantum number for our bosons. However, notice that this gives a phase and magnitude degree of freedom between the two sublattices.

Now the spin-wave expansion can be calculated. Following the same approach as before and expanding spin operators in terms of Holstein-Primakoff operators up to bilinear order, the Hamiltonian becomes

$$\hat{H} = JzS \sum_k \left[\gamma_k (\hat{c}_k \hat{d}_{-k} + \hat{c}_{-k}^\dagger \hat{d}_k^\dagger) + (\hat{c}_k^\dagger \hat{c}_k + \hat{d}_k^\dagger \hat{d}_k) \right]. \tag{2.32}$$

This expression is not diagonal in the bosonic operators because the spin-flip terms couple $\hat{c}_k^\dagger$ and $\hat{d}_{-k}$. The Hamiltonian does not commute with the number operators of the c and d bosons and because of this they are not conserved. But we can construct a mixed eigenoperators which contain contributions from both.

To do so, first the Hamiltonian must be reorganized so that

$$\begin{aligned} \hat{H} &= JzS \sum_k \left[\gamma_k (\hat{c}_k \hat{d}_{-k} + \hat{c}_k^\dagger \hat{d}_{-k}^\dagger) + (\hat{c}_k^\dagger \hat{c}_k + \hat{d}_{-k}^\dagger \hat{d}_{-k}) \right] && (2.33) \\ &= \mathbf{v}_k^\dagger M_k \mathbf{v}_k && (2.34) \end{aligned}$$

with the kernel matrix M_k and

$$\mathbf{v}_k^\dagger = [\hat{c}_k, \hat{d}_{-k}^\dagger]. \tag{2.35}$$

The solution at k is now a boson $\hat{\alpha}_k$ which is defined as a linear combination of $\hat{c}_k^\dagger$

and $\hat{d}_{-k}$. This should be of the form

$$\begin{aligned}\hat{\alpha}_k &= u_k \hat{c}_k - v_k \hat{d}^\dagger_{-k} \\ \hat{\alpha}^\dagger_k &= u_k \hat{c}^\dagger_k - v_k \hat{d}_{-k}.\end{aligned} \tag{2.36}$$

However this needs some care since bosonic commutation relations must be respected. Requiring that

$$[\hat{\alpha}_k, \hat{\alpha}^\dagger_{k'}] = \delta_{k,k'}, \tag{2.37}$$

one obtains

$$u_k^2 - v_k^2 = 1. \tag{2.38}$$

This defines a hyperbolic transform and a new basis in which the Hamiltonian becomes diagonal. This can be done by specifying a mixing angle θ, such that

$$u_k = \cosh\theta \tag{2.39}$$

$$v_k = \sinh\theta. \tag{2.40}$$

Interestingly we have obtained an additional mode

$$\begin{aligned}\hat{\beta}_k &= v_k \hat{c}_k + u_k \hat{d}^\dagger_{-k} \\ \hat{\beta}^\dagger_k &= v_k \hat{c}^\dagger_k + u_k \hat{d}_{-k}.\end{aligned} \tag{2.41}$$

This mode has the property

$$[\hat{\beta}_k, \hat{\beta}^\dagger_{k'}] = -\delta_{k,k'}, \tag{2.42}$$

due to the bosonic condition on $\hat{\alpha}_k$. This is a mathematical artefact of the increased solution space allowed by the Bogoliubov transform, but does not represent any physical modes.

Solving for these eigenmodes of the Hamiltonian the band-energy is

$$\epsilon_k^\pm = 2JzS\sqrt{1-\gamma_k^2} \tag{2.43}$$

$$= 2JzS\sin\delta k. \tag{2.44}$$

This expression thus results in a linear dispersion around the Γ-point.

It's important to point out that in obtaining this solution it is necessary to do a Bogoliubov transform such as equation (2.36). However, in the limit of large S where Néel order is a good approximation, we can apply a classical picture similar to the one adopted for ferromagnetic magnons and express the solution in $\hat{c}$ and $\hat{d}$ space. Thinking of the $\hat{c}$ and $\hat{d}$ bosons as defining orthogonal polarization axes, we can view $\hat{\alpha}$ and $\hat{\beta}$ as two modes of polarization of the propagating magnon. This is depicted in figure 2.5. As pointed out earlier, the addition of another sublattice introduces a phase-degree of freedom, which means that there may be an offset in the rotation of the two sublattice components of the wave-function, so that it need not be as symmetric as depicted here.

2.2.2 Generalized Bogoliubov de Gennes Hamiltonian

In the above section we showed how the Bogoliubov transform results in the correct bosonic field operators, as long as they are normalized correctly. The Heissenberg anti-ferromagnet is a special case where the anomalous pairing terms $\hat{c}_k\hat{d}_{-k}$ are the only dispersing terms in the Hamiltonian. In general, most magnets have more complicated unit cells with anisotropies which result in a large variety of interactions. In such cases it turns out to be very useful to express the problem using a generalized Bogoliubov transformation [140].

Given a unit cell with N sublattice order in a Néel state, we may define N independent magnons with quasi-momentum k as $[\hat{c}_{1,k}, \ldots, \hat{c}_{N,k}]$. Up to bilinear order in the field operators we will then have a Hamiltonian like

$$\hat{H} = \sum_k \left[\sum_{\langle i,j \rangle} (\gamma_{i,j}^{(1)} \hat{c}_{i,k}^\dagger \hat{c}_{j,k} + \gamma_{i,j}^{(2)} \hat{c}_{i,k} \hat{c}_{j,-k} + \text{H. c.}) + \sum_i \epsilon_i \hat{c}_{i,k}^\dagger \hat{c}_{i,k} \right] \tag{2.45}$$

$$= \sum_k \hat{H}_k \tag{2.46}$$

The objective is as usual to get $\hat{H}_k$ in a diagonal form. We rewrite this as

$$\hat{H} = \sum_k (H_k + H_{-k})/2 \tag{2.47}$$

$$\equiv \sum_k H_k^{\text{BdG}} \tag{2.48}$$

$$= \sum_k \vec{v}_k^\dagger M_k^{\text{BdG}} \vec{v}_k. \tag{2.49}$$

Here we have written the Hamiltonian in terms of

$$\vec{v}_k^\dagger = [\hat{c}_{1,k}, \ldots, \hat{c}_{N,k}, \hat{c}_{1,-k}^\dagger, \ldots, \hat{c}_{N,-k}^\dagger]. \tag{2.50}$$

Now the objective is to obtain N independent eigenenergy solutions at each quasi-momentum

$$\hat{\alpha}_{i,k}^\dagger = \sum_j a_{j,k}^{(i)} \hat{c}_{j,k}^\dagger + \sum_j b_{j,k}^{(i)} \hat{c}_{j,k}. \tag{2.51}$$

The symmetrization of the Hamiltonian with respect to k means that each k is counted twice. The interactions are halved, which means that we will recover half the eigenenergies. This double-counting of k means that there is an additional branch of eigenenergy solutions expressed by the conjugate eigenstate $\hat{\alpha}_{i,-k}$, which also is a solution to this Hamiltonian. This is a non-physical solution, which arises as an artifact of the problem setup. It introduces an artificial particle-hole symmetry to the Hamiltonian, since it will have opposite eigenenergy.

We can express the eigenstates through the linear transform

$$\vec{\alpha} = T\vec{v}. \tag{2.52}$$

The normalization condition on $\vec{\alpha}$ may now be written as

$$T_k \sigma_3 T_k^\dagger = \sigma_3. \tag{2.53}$$

Here σ_3 is a diagonal matrix with the upper left N entries equal to 1 and the rest equal to -1.

We may instead look at the problem in the following way. The equations of motion of $\vec{v}$ obtained from the Schrödinger equation are

$$\dot{\vec{v}} = 2i\sigma_3 M_k^{\mathrm{BdG}} \vec{v}. \tag{2.54}$$

So to obtain the stationary states of the Schrödinger equation it suffices to diagonalize the matrix

$$\tilde{M}_k^{\mathrm{BdG}} = \sigma_3 M_k^{\mathrm{BdG}}. \tag{2.55}$$

Note that although this matrix is non-Hermitian, because it is the product of two non-singular matrices, it too will be non-singular and can always be diagonalized.

When T_k is found which diagonalizes $\tilde{M}_k$, it gives

$$T_k \tilde{M}_k T_k^{-1} = \begin{bmatrix} \omega_{1,k}/2 & & & & & \\ & \ddots & & & & \\ & & \omega_{N,k}/2 & & & \\ & & & -\omega_{1,k}/2 & & \\ & & & & \ddots & \\ & & & & & -\omega_{N,k}/2 \end{bmatrix}. \tag{2.56}$$

If some numerical routine is used to diagonalize $\tilde{M}_k$, then each $\vec{t}_{i,k}$ column of T_k will be normalized with respect to its Euclidian norm. The correct normalization can be enforced by requiring that

$$\vec{t}_{i,k} = \vec{t}_{i,k} / |\sigma_z \vec{t}_{i,k}|. \tag{2.57}$$

The introduction of the Bogoliubov transform is important for the discussion of unconventional magnetic models and it is necessary in the description of triplet excitations. We shall go into detail with this after one more concrete example of anti-ferromagnetic ordering.

2.2.3 The triangular anti-ferromagnet

An interesting case arises with the triangular anti-ferromagnet. For the pure Heissenberg model, the $\vec{S} \cdot \vec{S}$ interaction of each bond adds a competing interaction. Due to the arrangement of the spins in equilateral triangles, it is impossible to minimize the energy of each bond simultaneously, even in the large S limit. We here give the linear spin-wave treatment of the problem. For a treatment of this problem in-field see [141], and see also a detailed treatment of higher order processes such as decay and two-magnon continua in the two papers [142, 143].

The lattice can be represented as a decorated triangular lattice in which each

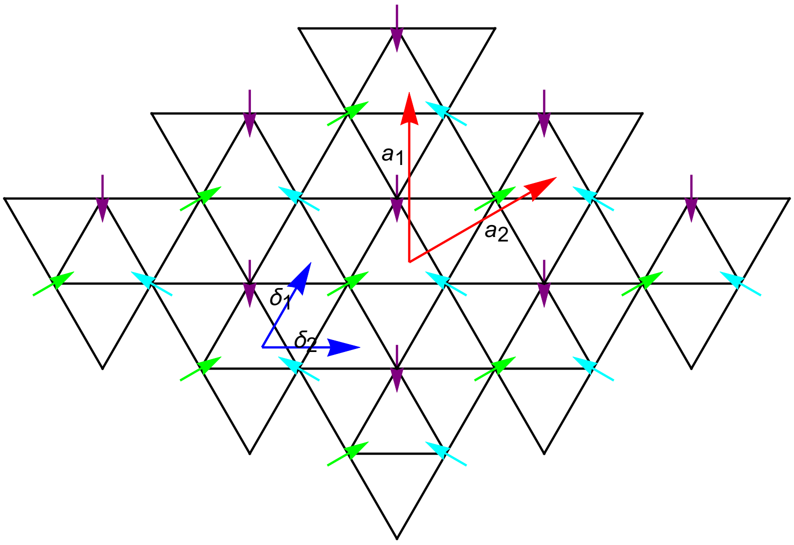

Figure 2.6: Triangular lattice with 120° order indicated. Also shown are lattice vectors δ_j, a_j of the chemical and magnetic unit cell.

point is an actual triangular configuraton of three spins that are oriented 120° with respect to each other, defining three different axes of quantization. Excitations on top of these spins are represented by three Holstein-Primakoff bosons $\hat{a}_i, \hat{b}_i, \hat{c}_i$.

The Holstein-Primakoff transformation now gives

$$\begin{aligned}
\hat{S}^x_{a_i} &= S\left(\hat{a}^\dagger_i\sqrt{1-\frac{\hat{a}^\dagger_i\hat{a}_i}{2S}}+\sqrt{1-\frac{\hat{a}^\dagger_i\hat{a}_i}{2S}}\hat{a}_i\right)\\
\hat{S}^y_{a_i} &= S\left(i\hat{a}^\dagger_i\sqrt{1-\frac{\hat{a}^\dagger_i\hat{a}_i}{2S}}-i\sqrt{1-\frac{\hat{a}^\dagger_i\hat{a}_i}{2S}}\hat{a}_i\right)\\
\hat{S}^z_{a_i} &= S-\hat{a}^\dagger_i\hat{a}_i
\end{aligned}\tag{2.58}$$

The operator $\hat{S}^z_{a_i}$ may be taken to define the quantization axes in the positive y-direction of the plane. In terms of a set of spin operators $\hat{S}^\alpha_i$, then $\hat{a}$ actually creates a $-S$ eigenstate of the $\hat{S}^y_i$ operator. This means we have performed a rotation of basis to rotate the spin z-axis into the y-axis. Therefore we must have

$$\begin{aligned}
\hat{S}^x_{a_i} &= \hat{S}^x_i\\
\hat{S}^y_{a_i} &= -\hat{S}^z_i\\
\hat{S}^z_{a_i} &= \hat{S}^y_i
\end{aligned}\tag{2.59}$$

We may obtain this by

$$\mathbf{S}_{a_i} = \begin{bmatrix} 1 & 0 & 0 \\ 0 & 0 & -1 \\ 0 & 1 & 0 \end{bmatrix} \mathbf{S}_i \tag{2.60}$$

$$= R_x\Big(-\frac{\pi}{2}\Big)\mathbf{S}_i \tag{2.61}$$

Where $R_x(\phi)$ is a rotation about the x-axis in euclidian space. In the same way, the other spins are described as eigenfunctions of the $\hat{S}_z$ after a rotation of the $\hat{S}_a^z$ operator in the (x,y)-plane. Thus

$$\mathbf{S}_{b_i} = R_z\Big(-\frac{2\pi}{3}\Big)\mathbf{S}_{a_i} \tag{2.62}$$

$$= \begin{bmatrix} -\frac{1}{2} & -\frac{\sqrt{3}}{2} & 0 \\ \frac{\sqrt{3}}{2} & -\frac{1}{2} & 0 \\ 0 & 0 & 1 \end{bmatrix} \mathbf{S}_{a_i}. \tag{2.63}$$

Bearing in mind that $R_i(\phi)^T = R_i(-\phi) = R_i(\phi)^{(-1)}$ holds for continuous rotations in a Lie group, an expression for the Hamiltonian may be derived by considering that there are three types of bonds, all of which have the following form

$$\mathbf{S}_{r_i} \cdot \mathbf{S}_{r_j} = \mathbf{S}_{r_i}^T \mathbf{S}_{r_j} \tag{2.64}$$

$$= \mathbf{S}_{a,r_i}^T R_x\Big(-\frac{\pi}{2}\Big) R_x\Big(\frac{\pi}{2}\Big) R_z\Big(\frac{2\pi}{3}\Big)\mathbf{S}_{b,r_j} \tag{2.65}$$

$$= \mathbf{S}_{a,r_i}^T R_z\Big(\frac{2\pi}{3}\Big)\mathbf{S}_{b,r_j}. \tag{2.66}$$

Now each $\hat{S}_{a,b,c}^{(i)}$ may be expanded in terms of its Holstein-Primakoff bosons.

If the above approach is followed correctly and all of the bonds accounted for, while $S = 1/2$ one may arrive at a Hamiltonian of the form

$$\hat{H} = \sum_k \hat{H}_k \tag{2.67}$$

with

$$\hat{H}_k = \frac{J}{16} \begin{bmatrix} \mathbf{v}_k \\ \mathbf{v}_{-k}^{\dagger} \end{bmatrix}^T \begin{bmatrix} h_k^{\mathrm{D}} & h_k^{\mathrm{ND}} \\ h_k^{\mathrm{ND}} & h_k^{\mathrm{D}} \end{bmatrix} \begin{bmatrix} \mathbf{v}_k^{\dagger} \\ \mathbf{v}_{-k} \end{bmatrix}. \tag{2.68}$$

Here we have

$$h_k^{\mathrm{D}} = \begin{bmatrix} 12 & \gamma^{(k)} & {\gamma^{(k)}}^* \\ {\gamma^{(k)}}^* & 12 & \gamma^{(k)} \\ \gamma^{(k)} & {\gamma^{(k)}}^* & 12 \end{bmatrix} \tag{2.69}$$

and

$$h_k^{\text{ND}} = \begin{bmatrix} 0 & -3\gamma^{(k)} & -3\gamma^{(k)*} \\ -3\gamma^{(k)*} & 0 & -3\gamma^{(k)} \\ -3\gamma^{(k)} & -3\gamma^{(k)*} & 0. \end{bmatrix}. \tag{2.70}$$

The vector

$$\mathbf{v}_k = \begin{bmatrix} \hat{a}_k \\ \hat{b}_k \\ \hat{c}_k \end{bmatrix}. \tag{2.71}$$

Also

$$\gamma^{(k)} = e^{i\delta_1 \cdot k} + e^{-i\delta_2 \cdot k} + e^{i(\delta_2 - \delta_1)\cdot k}. \tag{2.72}$$

The objective is now to determine the eigenstates of this Hamiltonian by a generalized Bogoliubov transformation. As it is written right now, the problem looks very difficult, since it involves a 6 × 6 matrix. However, there are also a lot of nice features to this matrix, which one may take advantage of to make the problem more tractable to analytical solution.

The matrices $h_k^{\text{D}}, h_k^{\text{ND}}$ are both Hermitian 3 × 3 matrices. By inspection

$$h_k^{\text{D}} = -h_k^{\text{ND}}/3 + 12 \cdot \mathbb{1}_{3\times 3}. \tag{2.73}$$

It is clear that the two matrices commute and therefore share eigenvectors. Denoting the eigenvalues $\epsilon_{\eta,k}^{\text{D}}$, $\epsilon_{\eta,k}^{\text{ND}}$, we infer that

$$\epsilon_{\eta,k}^{\text{D}} = -\epsilon_{\eta,k}^{\text{ND}}/3 + 12. \tag{2.74}$$

Here $\eta \in \{1, 2, 3\}$ is an index running over the (possibly degenerate) eigenvalues corresponding to each of three orthonormal eigenvectors, $\mathbf{u}_{\eta,k}$ that appear in the solutions.

The eigenvectors are

$$\mathbf{u}_{\eta,k} = \begin{bmatrix} 1 \\ \omega^{\eta-1} \\ \omega^{-\eta+1} \end{bmatrix}, \quad \omega = -\frac{1}{2} + i\frac{\sqrt{3}}{2}. \tag{2.75}$$

The corresponding eigenvalues are

$$\begin{aligned}
\epsilon^{\mathrm{D}}_{1,k} =& 12 + 2(\cos(k_x) + \cos(\frac{\sqrt{3}}{2}k_y - \frac{1}{2}k_x) + \cos(-\frac{\sqrt{3}}{2}k_y - \frac{1}{2}k_x)) \\
\epsilon^{\mathrm{D}}_{2,k} =& 12 - \cos(k_x) - \cos(\frac{\sqrt{3}}{2}k_y - \frac{1}{2}k_x) - \cos(-\frac{\sqrt{3}}{2}k_y - \frac{1}{2}k_x)) \\
&+ \sqrt{3}(\sin(k_x) + \sin(\frac{\sqrt{3}}{2}k_y - \frac{1}{2}k_x) + \sin(-\frac{\sqrt{3}}{2}k_y - \frac{1}{2}k_x)) \qquad (2.76) \\
\epsilon^{\mathrm{D}}_{3,k} =& 12 - \cos(k_x) - \cos(\frac{\sqrt{3}}{2}k_y - \frac{1}{2}k_x) - \cos(-\frac{\sqrt{3}}{2}k_y - \frac{1}{2}k_x)) \\
&- \sqrt{3}(\sin(k_x) + \sin(\frac{\sqrt{3}}{2}k_y - \frac{1}{2}k_x) + \sin(-\frac{\sqrt{3}}{2}k_y - \frac{1}{2}k_x))
\end{aligned}$$

Eigenstates of the Hamiltonian must be created by bosonic operators of the form

$$\hat{\alpha}^\dagger_k = e\hat{a}^\dagger_k + f\hat{b}^\dagger_k + g\hat{c}^\dagger_k + h\hat{a}_{-k} + i\hat{b}_{-k} + j\hat{c}_{-k}. \qquad (2.77)$$

We write down the Bogoliubov de Gennes Hamiltonian as discussed in the previous section.

$$M_k \equiv \begin{bmatrix} \mathbf{1}_{3\times3} & \mathbf{0}_{3\times3} \\ \mathbf{0}_{3\times3} & -\mathbf{1}_{3\times3} \end{bmatrix} \begin{bmatrix} h^{\mathrm{D}}_k & h^{\mathrm{ND}}_k \\ h^{\mathrm{ND}}_k & h^{\mathrm{D}}_k \end{bmatrix} \qquad (2.78)$$

$$= \begin{bmatrix} h^{\mathrm{D}}_k & h^{\mathrm{ND}}_k \\ -h^{\mathrm{ND}}_k & -h^{\mathrm{D}}_k \end{bmatrix}. \qquad (2.79)$$

We know that the physical solutions are the positive eigenvalues of M_k, and that for each one of them there exists a non-physical solution with the same magnitude but opposite sign. We therefore guess the following form for a useful eigenvalue equation

$$\lambda_{\eta,k} \begin{bmatrix} \alpha \\ \beta \end{bmatrix} \otimes \mathbf{u}_{\eta,k} = \frac{J}{8} \begin{bmatrix} h^{\mathrm{D}}_k & h^{\mathrm{ND}}_k \\ -h^{\mathrm{ND}}_k & -h^{\mathrm{D}}_k \end{bmatrix} \left(\begin{bmatrix} \alpha \\ \beta \end{bmatrix} \otimes \mathbf{u}_{\eta,k} \right) \qquad (2.80)$$

$$= \frac{J}{8} \left(\begin{bmatrix} \epsilon^{\mathrm{D}}_{\eta,k} & \epsilon^{\mathrm{ND}}_{\eta,k} \\ -\epsilon^{\mathrm{ND}}_{\eta,k} & -\epsilon^{\mathrm{D}}_{\eta,k} \end{bmatrix} \begin{bmatrix} \alpha \\ \beta \end{bmatrix} \right) \otimes \mathbf{u}_{\eta,k}. \qquad (2.81)$$

Here the factor of $J/8$ has been added so that $\lambda_{\eta,k}$ become the actual eigenenergies. In this way we have reduced the problem of diagonalizing a 6×6 matrix to a 3×3 and a 2×2 one. Here $\otimes$ is the tensor product operator which we have used to simplify notation, such that the vector in the left hand side of equation (2.80) is 6-dimensional containing the eigenvector $\mathbf{u}_{\eta,k}$ repeated, and α, β are scalars that solve the above equation. By writing the characteristic polynomial of the above matrix, we get

$$\lambda_{\eta,k} = \pm\frac{J}{8}\sqrt{{\epsilon^{\mathrm{D}}_{\eta,k}}^2 - \epsilon^{\mathrm{ND}2}_{\eta,k}}. \qquad (2.82)$$

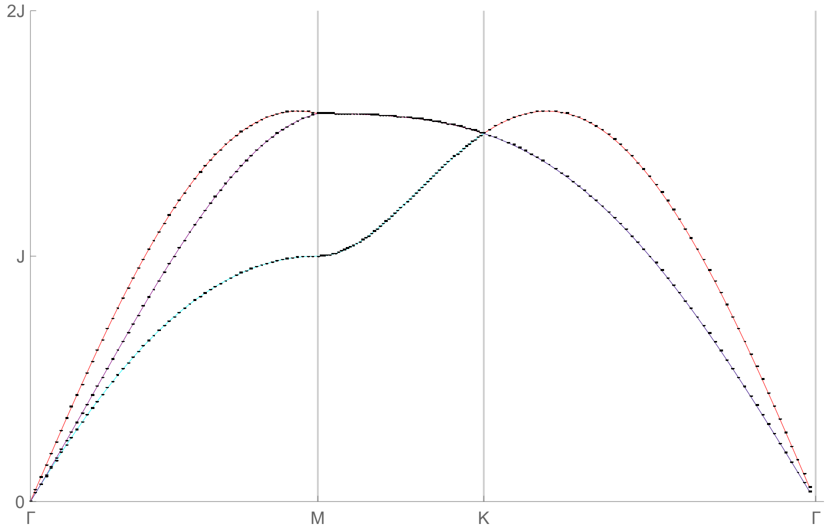

Figure 2.7: This graphic shows the magnon dispersion relation of the anti-ferromagnetic triangular lattice. High symmetry points are marked with letters Γ, *M* and *K*. The solid lines have been obtained from the analytical expression of equation (2.83) and the dots are the result of numerically diagonalizing the generalized Bogoliubov de Gennes Hamiltonian.

Therefore the eigenenergies are

$$\omega_{\eta,k} = \frac{J}{4}\sqrt{{\epsilon^{\mathrm{D}}_{\eta,k}}^{2} - \epsilon^{\mathrm{ND}2}_{\eta,k}}. \tag{2.83}$$

Figure 2.7 shows the dispersion of the triangular lattice. One of the interesting features of the analytic solution is that each band is equivalent. The three bands that are seen in the 1st Brillouin zone can all be obtained by continuing the analytic expression obtained from equation (2.83) of a single band into neighbouring Brillouin zones. By tracing a single band as it crosses the zone border it can be shown that it smoothly merges into one of the other two bands, depending on where it crossed. Thus the entire band structure can be obtained from a single band that is folded in on itself.

2.3 Triplons and other generalized excitations

In certain materials classical order does not occur. In fact there are some materials in which the ground state is disordered because a quantum mechanical state is preferred. This occurs for instance in the well-known quantum paramagnet $SrCu_2(BO_3)_2$, whose ground state is a dimer singlet product state [144–146].

The simplest model for magnetism in $SrCu_2(BO_3)_2$ is the famous Shastry-Sutherland model [147] shown in figure 2.8. This is a $S = 1/2$ model of orthogonal dimers. The

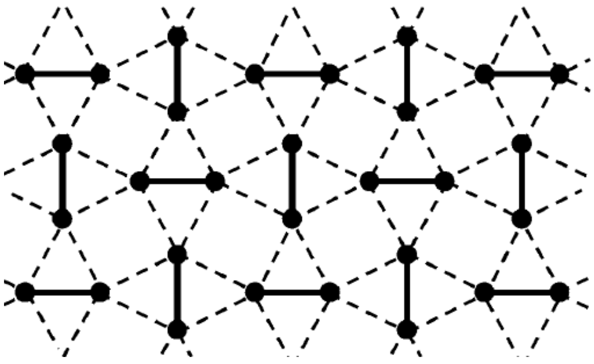

Figure 2.8: This drawing shows the Shastry-Sutherland lattice. The bold bonds are the dimers.

Hamiltonian is

$$\hat{H} = J \sum_{\langle i,j\rangle \in \ddagger} \vec{S}_i \cdot \vec{S}_j + J' \sum_{\langle i,j\rangle \notin \ddagger} \vec{S}_i \cdot \vec{S}_j. \tag{2.84}$$

Here the sum with the dominant interaction J is taken over the solid dimer bonds of figure 2.8 and $S = 1/2$.

If the dominant interaction in the system is $J > 0$, we can adopt a strategy where the dimer bond energy is minimized and the inter-dimer bonds describe hopping. First we consider a single dimer Hamiltonian

$$\hat{H}_{\langle i,j\rangle \in \ddagger} = J\vec{S}_i \cdot \vec{S}_j \tag{2.85}$$

$$= J/2\left[(\vec{S}_i + \vec{S}_j)^2 - \vec{S}_i^2 - \vec{S}_j^2\right] \tag{2.86}$$

$$= J/2\left[\vec{S}_\ddagger^2 - 3/2\right]. \tag{2.87}$$

Here we introduced the total dimer spin $\vec{S}_\ddagger = \vec{S}_i + \vec{S}_j$. We can associate a spin quantum number $S_\ddagger$ with this vector quantity, so that

$$\vec{S}_\ddagger^2 = S_\ddagger(S_\ddagger + 1). \tag{2.88}$$

In the case of the $S = 1/2$ dimer this is diagonal in the basis[1]

$$\begin{aligned} |s\rangle &= |S_\ddagger = 0, S^z = 0\rangle = (|\uparrow,\downarrow\rangle - |\downarrow,\uparrow\rangle)/\sqrt{2} \\ |t_1\rangle &= |S_\ddagger = 1, S^z = 1\rangle = |\uparrow,\uparrow\rangle \\ |t_0\rangle &= |S_\ddagger = 1, S^z = 0\rangle = (|\uparrow,\downarrow\rangle + |\downarrow,\uparrow\rangle)/\sqrt{2} \\ |t_{-1}\rangle &= |S_\ddagger = 1, S^z = -1\rangle = |\downarrow,\downarrow\rangle\,. \end{aligned} \tag{2.89}$$

The S^z quantity above is the eigenvalue of the bond operator

$$\hat{S}_\ddagger^z = \hat{S}_i^z + \hat{S}_j^z, \tag{2.90}$$

---

[1] See also the bond-operator formulation as it was originally presented by Sachdev et. al. [148].

which is diagonal in this basis. The ground state energy in the $J \gg J'$ limit is minimized by the singlet state $|s\rangle$. We can now write the Hamiltonian in terms of interacting dimers whose on-site energy is given by

$$\hat{H}_{\substack{\bullet\\|\\\bullet}} = J\big[-3/4\hat{s}^\dagger\hat{s} + 1/4\sum_{m=-1}^{1}\hat{t}_m^\dagger\hat{t}_m\big]. \tag{2.91}$$

Here we have used bosonic field operators for the dimer singlet and triplet states. The inter-dimer coupling then needs to be written by expanding the on-site spin operators in this basis. This results in

$$\begin{aligned} \hat{S}_i^z &= \frac{1}{2}\big(\hat{t}_1^\dagger\hat{t}_1 - \hat{t}_{-1}^\dagger\hat{t}_{-1}\big) - \frac{(-1)^i}{2}\big(\hat{t}_0^\dagger\hat{s} + \hat{t}_0\hat{s}^\dagger\big) \\ \hat{S}_i^\pm &= \frac{1}{\sqrt{2}}\big(\hat{t}_\pm^\dagger\hat{t}_0 + \hat{t}_0^\dagger\hat{t}_\mp\big) \pm \frac{(-1)^i}{\sqrt{2}}\big(\hat{t}_\pm^\dagger\hat{s} - \hat{s}^\dagger\hat{t}_\mp\big). \end{aligned} \tag{2.92}$$

Here the i is 0 or 1 depending on whether the operator is applied to the first or second spin in the dimer. For a discussion of quantum phase transitions on the Shastry-Sutherland model using the series expansion method see [146] where a quantum phase transition to an ordered state is predicted at $J'/J = 0.677(2)$, or the later iPEPS study [149], which locates the transition at $J'/J = 0.677(2)$.

Now the Hamiltonian is written out by taking the sum over each dimer and counting its coupling to sites. This bond-wave formalism [148] treats each strongly coupled pair of spins as a composite particle. By diagonalizing the Hamiltonian exactly at the bond level it is possible to express quantum mechanical effects, such as entanglement exactly at the local level. The triplet states then propage in a fashion similar to regular spin-waves. These quasiparticles are referred to as *triplons*. They carry topological transport signatures such as the thermal Hall effect [11], and as we shall see in Chapter 4 spin Nernst as well.

To diagonalize the Hamiltonian of this system we can make use of the hard-core constraint on each dimer

$$\hat{s}^\dagger\hat{s} + \sum_{i=-1}^{1}\hat{t}_i^\dagger\hat{t}_i = 1. \tag{2.93}$$

This can be expressed through the Holstein-Primakoff transform

$$\hat{s} = \hat{s}^\dagger = \sqrt{1 - \sum_{i=-1}^{1}\hat{t}_i^\dagger\hat{t}_i}. \tag{2.94}$$

This now gives us a way to express propagation of triplons in the background of a quantum mechanically disordered singlet product state. Due to the global $SU(2)$ symmetry of the model the triplet spectrum is three-fold degenerate. Although the unit cell contains two dimers, it can be reduced to an effective square lattice model with a single site per unit cell. Here it is enough to imagine the dimers of figure 2.8

as being contracted to single points. The spectrum can be worked out as

$$\omega(\vec{k}) = \sqrt{J^2 - JJ'(\cos k_x - \cos k_y)}. \tag{2.95}$$

The triplet picture breaks down when $J' \geq J/2$, as the singlet is no longer energetically favorable due to the inter-dimer couplings.

In this chapter we have given an overview of the Heisenberg model and how spin-wave theory can be used to treat magnon physics. We also gave a brief introduction to generalized spin-waves and the treatment of triplon dispersion. Having established these concepts we are ready to discuss the topology of magnon bands and how it may be affected by the Dzyaloshinskii-Moriya interaction.

Chapter 3

Topological bands in insulating magnets

In the previous chapter we discussed band-like excitations in magnetically ordered solids and introduced key generalizations upon conventional spin-wave theory which allow a description of excitations in quantum paramagnets. Having a theory of dispersing quasi-particles in magnets we can investigate the topology of these bands, which is the topic of this chapter. With this we will be able to discuss the core research questions of this thesis.

We start this chapter by introducing key concepts from topological band-theory. As a first example of how topology plays a role in the physics of single particles we consider the Hamiltonian of a generic two-level system. This will allow us to define the Berry phase and curve as well as Chern numbers. In later chapters we will frequently return to this prototypical system by reducing our analyses to effective theories which are dual to this problem. For concreteness we derive all of these quantities for the lattice Chern insulator as well. This allows us to discuss the role of time-reversal symmetry breaking and robust topological features. Finally, we will discuss $\mathcal{Z}_2$ invariants and the psuedo-time-reversal operator relevant for magnetic excitations.

3.1 Generic two-level systems and their topology

In this section we will describe a generic two-level quantum system. A detailed analytical description is very straightforward in such systems. It is also very informative as we may easily derive the Chern number, which is a topological invariant which directly determines the quantum Hall coefficient of electronic insulators.

The strength of this approach lies in its ability to describe bandgaps caused by some finite anisotropic interaction. Even in models with multiple sub-lattices, often effective spinor models can be derived to which these concepts are applicable. For a very thorough treatment of the content of this section see [21].

Given a two-level system with some set of parameters $\mathbf{x}$, we can generically write its Hamiltonian as

$$\hat{H}(\mathbf{x}) = \epsilon(\mathbf{x})\boldsymbol{I} + \vec{d}(\mathbf{x}) \cdot \vec{\sigma}. \tag{3.1}$$

Here the $\vec{\sigma} = (\boldsymbol{\sigma}_x, \boldsymbol{\sigma}_y, \boldsymbol{\sigma}_z)$ are the Pauli matrices acting on the arbitrarily labelled Hilbert space $\{|0\rangle, |1\rangle\}$. The exact solution to this Hamiltonian can be found by considering the vector $\vec{d}(\mathbf{x})$. We can parametrize it as

$$\begin{aligned} d_1 &= d_0(\mathbf{x}) \sin\big[\theta(\mathbf{x})\big] \cos\big[\phi(\mathbf{x})\big] \\ d_2 &= d_0(\mathbf{x}) \sin\big[\theta(\mathbf{x})\big] \sin\big[\phi(\mathbf{x})\big] \\ d_3 &= d_0(\mathbf{x}) \cos\big[\theta(\mathbf{x})\big]. \end{aligned} \tag{3.2}$$

Here the angles are in the ranges $\theta(\mathbf{x}) \in [0;\pi]$ and $\phi(\mathbf{x}) \in [0;2\pi)$. This can be diagonalized by the eigenstates

$$\begin{aligned} |\psi_+\rangle(\mathbf{x}) &= e^{i\phi(\mathbf{x})/2} \cos[\theta(\mathbf{x})/2] |0\rangle + e^{-i\phi(\mathbf{x})/2} \sin[\theta(\mathbf{x})/2] |1\rangle \\ |\psi_-\rangle(\mathbf{x}) &= e^{i\phi(\mathbf{x})/2} \sin[\theta(\mathbf{x})/2] |0\rangle - e^{-i\phi(\mathbf{x})/2} \cos[\theta(\mathbf{x})/2] |1\rangle. \end{aligned} \tag{3.3}$$

Their eigen-energy is very simply

$$E_\pm = \epsilon(\mathbf{x}) \pm d_0(\mathbf{x}). \tag{3.4}$$

The eigenenergies are determined only by d_0 and the diagonal ϵ whereas the angles θ and ϕ determines the eigenstates. However, this parametrization may not be possible for all $\mathbf{x}$ since as soon as $d_0 = 0$ these angles are undefined.

Now, when we define the eigenstates, we are implicitly making a gauge choice for them as well. There are certain situations where this gauge cannot be defined continuously. Due to this phase singularity a Berry phase appears. We can define this as follows. Imagine that the Hamiltonian is taken through an adiabatic change of parameters. Then the eigenstates evolve as

$$\hat{H}\big(\mathbf{x}(t)\big) e^{-i\theta(\mathbf{x}(t))} |\psi_\pm\big(\mathbf{x}(t)\big)\rangle = i\frac{d}{dt} e^{-i\theta(\mathbf{x}(t))} |\psi_\pm\big(\mathbf{x}(t)\big)\rangle \tag{3.5}$$

$$= ie^{-i\theta(\mathbf{x}(t))} \frac{d}{dt} |\psi_\pm\big(\mathbf{x}(t)\big)\rangle + \Big(\frac{d}{dt}\theta\big(\mathbf{x}(t)\big)\Big) e^{-i\theta(\mathbf{x}(t))} |\psi_\pm\big(\mathbf{x}(t)\big)\rangle. \tag{3.6}$$

From this we recover an expression for the phase change during a time evolution as

$$\Delta\theta = \int_0^t \frac{d}{dt'} \theta\big(\mathbf{x}(t')\big) dt' \tag{3.7}$$

$$= \int_0^t dt' E_\pm\big(\mathbf{x}(t')\big) + \gamma_\pm \tag{3.8}$$

Here we have the dynamical phase resulting from changes in the eigenergy $E_\pm$ as well as a Berry phase which for some adiabatic change in parameters $\mathbf{x}(t)$ is

$$\gamma_{\pm} = i \int_0^t \langle \psi_{\pm} | \frac{d}{dt'} | \psi_{\pm} \rangle \, dt' \tag{3.9}$$

$$= i \int_{\mathbf{x}(t)} \langle \psi_{\pm} | \nabla_{\mathbf{x}} | \psi_{\pm} \rangle \cdot d\mathbf{x} \tag{3.10}$$

$$= i \int \left\langle \psi_{\pm} \middle| \frac{\partial}{\partial \theta} \middle| \psi_{\pm} \right\rangle d\theta + i \int \left\langle \psi_{\pm} \middle| \frac{\partial}{\partial \phi} \middle| \psi_{\pm} \right\rangle d\phi \tag{3.11}$$

The change in coordinates from $\mathbf{x}$ to θ and ϕ is valid here because the wave-function is a function of the parameters θ and ϕ, which are uniquely determined by $\mathbf{x}$. This motivates a definition of the Berry connection in terms of

$$\begin{aligned} A_{\theta,\pm} &\equiv i \left\langle \psi_{\pm} \middle| \frac{\partial}{\partial \theta} \middle| \psi_{\pm} \right\rangle \\ A_{\phi,\pm} &\equiv i \left\langle \psi_{\pm} \middle| \frac{\partial}{\partial \phi} \middle| \psi_{\pm} \right\rangle \end{aligned} \tag{3.12}$$

as the vector

$$\vec{A}_{\pm} = \begin{bmatrix} A_{\theta,\pm} \\ A_{\phi,\pm} \end{bmatrix}. \tag{3.13}$$

We observe that the Berry phase is a line integral, which may or may not be closed. If the integral is over a closed curve C then

$$\gamma_{\pm} = i \oint_C \vec{A}_{\pm} \cdot d\mathbf{v} \tag{3.14}$$

$$= i \iint_D \nabla \times \vec{A}_{\pm} d\theta d\phi. \tag{3.15}$$

Here the 2D curl of $\vec{A}_{\pm}$ is the Berry curvature

$$F_{\theta,\phi} = \partial_\theta A_\phi - \partial_\phi A_\theta. \tag{3.16}$$

We have here used Stokes' theorem to convert the line integral of $\vec{A}$ over the closed curve c into an integral over the domain D enclosed by the Berry curvature. It is worthwhile noticing that the Berry connection in general is gauge-dependent. This can be shown quite easily as if we transform the wave-function $|\psi\rangle \to e^{i\alpha} |\psi\rangle$, we will also get

$$\vec{A} \to \nabla \alpha + \vec{A} \tag{3.17}$$

Now the vector field defined by the gradient $\nabla \alpha$ is by definition a conservative one. Its curl must be zero. Therefore the Berry curvature is gauge invariant. Using the Berry curvature is often more convenient as we can diagonalize the Hamiltonian without having to take into account the derivatives of the gauge we define.

The two-level Hamiltonian we introduced here in order to parametrize the wave-function in terms of θ and ϕ is a generic one. Thus the exact Berry curvature in this situation is also a general expression for two-level systems, given that such a parametrization exists. We obtain for each eigenstate

$$F_{\pm,\theta\phi} = \partial_\theta \langle \psi_\pm | \partial_\phi | \psi_\pm \rangle - \partial_\phi \langle \psi_\pm | \partial_\theta | \psi_\pm \rangle \tag{3.18}$$

$$= \pm \frac{\sin(\theta)}{2}. \tag{3.19}$$

We may now compute the integral. However, we should think carefully about how this is done and there are some special cases that warrant our attention.

Each combination of θ and ϕ defines an eigenstate of the Hamiltonian. Thus, the parametrization of the Hamiltonian may form a sphere if every combination of θ and ϕ are accounted for. This is the so-called Bloch sphere, and interestingly due to this parametrization, the gauge at the poles is undetermined. This is because the polar-angle ϕ is ill-defined here, in exact analogy to the compass needle, which cannot be oriented at the exact north and south poles of a globe. This phase-singularity cannot be removed by some clever choice of gauge as long as the full globe is covered. This is fundamentally because the topology of the sphere and the torus defined by the product space of θ and ϕ are inequivalent closed surfaces. Although we could construct a one-to-one map between them, this map would not be homeomorphic, so if we define a unique gauge for every point on the Bloch sphere, there will always be some discontinuity in the phase of the wave-function. We shall see more consequences of this below.

3.1.1 Enclosed topological charge

The Berry curvature can be generalized to yield an important intuition which will help us characterize it. In terms of $\vec{d}$ we define a three-dimensional vector field with components

$$\mathbf{F}_{\pm,i} = \epsilon_{i,j,k} \partial_{d_j} \langle \psi_\pm | \partial_{d_k} | \psi_\pm \rangle \tag{3.20}$$

$$= \pm \frac{1}{2} d_i / {d_0}^3. \tag{3.21}$$

Now we can define a 2-dimensional closed surface in **d**-space. We denote it by S and require that it is given by the angular parametrization $\mathbf{d}_S(\theta, \phi) \in S$. We imagine that this is the $\vec{d}$ which defines the Hamiltonian of a given problem, and now we are interested in evaluating the Berry phase associated with this parameter space. The Berry curvature is given by the flux-density of the above defined **F** through that surface. We can take the surface integral

$$\gamma_\pm = \iint_S \mathbf{F}_\pm \cdot d\mathbf{S}. \tag{3.22}$$

We notice that the field F_i is the field of a monopole centered at $\vec{d} = \vec{0}$. When we take the surface integral over a S we get

$$\gamma_\pm = \pm 2\pi n. \tag{3.23}$$

Here n is the Chern number [21]. The topological charge is centered at the origin, so if the surface $\mathbf{d}_S$ encloses the origin then n will be nonzero. If the surface is a sphere then n will be 1, but in general $\mathbf{d}_S$ could be parameterized for instance in such a way that the ϕ angle is wound around twice during integration. Then $n = 2$.

In summary, whenever our Hamiltonian can be written as a spinor-model we can simply look at the enclosed topological charge. Our Hamiltonian is defined by some parametrized surface in $\vec{d}$ space and this parameterization determines the Berry curvature.

To see the full derivation of equation (3.22) please see Appendix B, where we also discuss some generic cases where this formulation is applicable.

3.2 Chern Insulators

Chern insulators are a class of materials characterized by having topological properties arising from the breaking of time-reversal symmetry. The prototypical lattice model describing this phenomenon is the Haldane model of spinless electrons on the honeycomb lattice. As introduced in Section 1.2 the Hamiltonian is given by

$$\hat{H} = t_1 \sum_{\langle i,j \rangle} \hat{c}_i^\dagger \hat{c}_j + \text{H. c.} + t_2 e^{i\phi} \sum_{\langle\langle i,j \rangle\rangle} \hat{c}_i^\dagger \hat{c}_j + \text{H. c.} + M \sum_{i \in A, j \in B} (\hat{c}_i^\dagger \hat{c}_i - \hat{c}_j^\dagger \hat{c}_j) \tag{3.24}$$

The Hamiltonian of equation (3.24) is a tight-binding model of spinless electrons in the presence of a magnetic field. The magnetic field in this case can arise from spontaneous ordering of magnetic moments embedded in the honeycomb lattice. This gives rise to a complex hopping between next-nearest neighbor sites, whose sign depends on whether the hopping direction is clockwise or counterclockwise around the hexagon of the honeycomb lattice. The complex phase of the hopping ϕ is the line integral of the field taken from one site to its next-nearest neighbor.

In the spinor space of the two sub-lattices $\vec{v}_{\vec{k}} = (\psi_{A,\vec{k}}, \psi_{B,\vec{k}})^T$ we expand this through a Fourier transform to give

$$\begin{aligned} \hat{H} &= \sum_{\vec{k}} \vec{v}_{\vec{k}}^\dagger \hat{H}(\vec{k}) \vec{v}_{\vec{k}} \qquad (3.25) \\ &= 2t_2 \cos\phi \Big(\sum_i \cos(\vec{k} \cdot \vec{b}_i) \Big) \boldsymbol{I} + t_1 \Big(\sum_i [\cos(\vec{k} \cdot \vec{a}_i) \boldsymbol{\sigma}_1 + \sin(\vec{k} \cdot \vec{a}_i) \boldsymbol{\sigma}_2] \Big) \\ &\quad + \Big[M - 2t_2 \sin\phi \Big(\sum_i \sin(\vec{k} \cdot \vec{b}_i) \Big) \Big] \boldsymbol{\sigma}_3. \qquad (3.26) \end{aligned}$$

Here each σ_i is a Pauli matrix describing the mixing of the two sub-lattices. In terms of the coefficients of each Pauli matrix, the exact eigenstates can be found. We can rewrite the Hamiltonian as

$$\hat{H}_k = \epsilon(\vec{k}) \boldsymbol{I} + \vec{d}(\vec{k}) \cdot \vec{\sigma}. \tag{3.27}$$

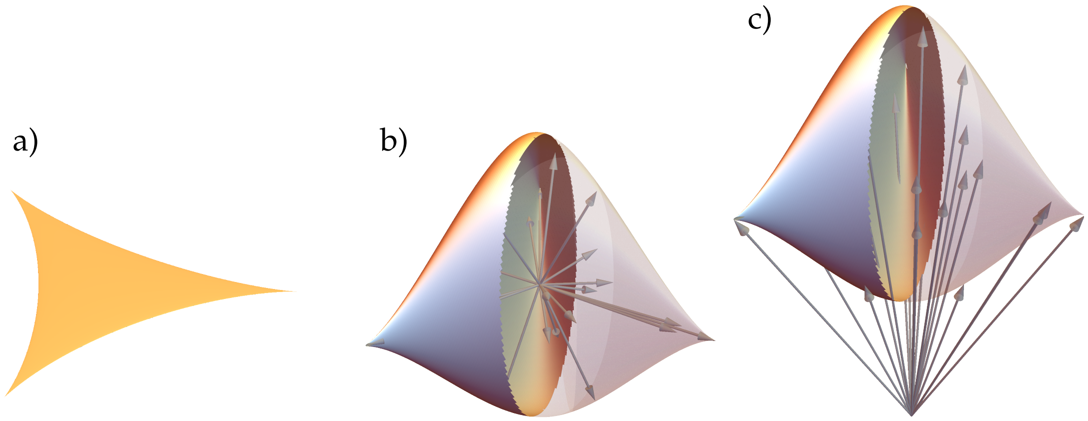

Figure 3.1: We here show the surface drawn out by the vector $\vec{d}(k)$ defined by the Haldane model (see equation (3.26) and equation (3.28)) parametrized by $\vec{k}$. These surfaces are drawn by evaluating $\vec{d}(k)$ at every point in the Brillouin zone, and the origin corresponds to $\vec{d}(k) = 0$. (a) with inversion and time-reversal symmetry, the d_3 component is zeroed out completely, and the surface drawn out by the d-vector is flat and does not enclose any volume. (b) Here breaking of time-reversal symmetry allows a finite d_3. We draw the field $\mathbf{F}_\pm$ with gray arrows from the origin out to the surface defined by $\vec{d}(\vec{k})$. With the topological charge enclosed, the Berry's curvature will here integrate up to $\pm 2\pi n$. (c) Both time-reversal and inversion symmetry is broken thus allowing for an M term. Here the M term is large enough so that field $\mathbf{F}_\pm$ no longer originates from the surface of $\vec{d}(\vec{k})$, so the Berry's curvature will integrate up to zero.

Each d_i is a coefficient belonging to the corresponding $\boldsymbol{\sigma}_i$ as they appear in equation (3.26).

We parametrize the vector $\vec{d}$ as

$$\begin{aligned} d_1 &= \alpha_{\vec{k}} = t_1 \sum_i \cos(\vec{k}\cdot\vec{a}_i) \\ d_2 &= \beta_{\vec{k}} = t_1 \sum_i \sin(\vec{k}\cdot\vec{a}_i) \\ d_3 &= \kappa_{\vec{k}} = M - 2t_2 \sin\phi \left(\sum_i \sin(\vec{k}\cdot\vec{b}_i) \right) \end{aligned} \tag{3.28}$$

Now we can discuss the role of time-reversal (τ) and inversion (i) symmetries in a similar vein to Haldane's original work [4]. To be clear, for the honeycomb lattice we will discuss the inversion through the center of each bond. We describe their action on the system in terms of their action on $\vec{k}$ and the Pauli matrices $\boldsymbol{\sigma}_1$, $\boldsymbol{\sigma}_2$ and $\boldsymbol{\sigma}_3$.

We have

$$\begin{aligned} \tau &: \vec{k} \to -\vec{k} & i &: \vec{k} \to -\vec{k} \\ \tau &: \boldsymbol{\sigma}_1 \to \boldsymbol{\sigma}_1 & i &: \boldsymbol{\sigma}_1 \to \boldsymbol{\sigma}_1 \\ \tau &: \boldsymbol{\sigma}_2 \to -\boldsymbol{\sigma}_2 & i &: \boldsymbol{\sigma}_2 \to -\boldsymbol{\sigma}_2 \\ \tau &: \boldsymbol{\sigma}_3 \to \boldsymbol{\sigma}_3 & i &: \boldsymbol{\sigma}_3 \to -\boldsymbol{\sigma}_3 \end{aligned} \tag{3.29}$$

The $\alpha_{\vec{k}}$ term is even under time-reversal since it is co-sinusoidal in $\vec{k}$. The $\beta_{\vec{k}}$ is odd under time-reversal since it is sinusoidal, but $\boldsymbol{\sigma}_2$ is also odd under time-reversal and their product therefore enters the Hamiltonian as an even term. The third term however has a sinusoidal part, which is odd and a constant M which is even.

The Haldane model is an example where topological bands are caused by the breaking of TR symmetry. The M arises from a constant on-site potential which can appear in inversion asymmetric honeycomb lattices. This by itself introduces a band-gap which has the effect of turning the Haldane model into a conventional band-insulator. But the TR breaking second term in $\kappa_{\vec{k}}$ is inversion symmetric.

In summary, when τ and i are both symmetries of the Haldane model, $d_3(k)$ must both be even and odd in k, and therefore it has to be zero. When only τ is broken, t_2 may be non-zero, which opens up the volume inside the surface defined by $\vec{d}(k)$. If inversion symmetry too is broken then a non-zero M term may have the effect of moving this volume up or down in $\vec{d}$-space along the third axis. If $|M|$ is sufficiently large the surface will intersect the origin, meaning that there will be some point in k-space where the two bands are degenerate. If it is larger still there will be a topological phase transition to a trivial phase. This is evident from the fact that the volume now does not enclose the origin in $\vec{d}$-space. These three different cases are summarized in figure 3.1.

3.3 Complex hopping and the Dzyaloshinskii-Moriya interaction

In discussing the Haldane model in Section 1.1 we briefly visited how a complex hopping is needed in order to originate topologically non-trivial bands. Specifically it is the term

$$it_2 \sin\phi \sum_{\langle i,j \rangle} \hat{c}_i^\dagger \hat{c}_j \tag{3.30}$$

which allows a finite z-component of the $\vec{d}$-vector. This term has to be generated by some time-reversal breaking field, and in Haldane's original paper it is speculated that this could be achieved by spontaneous magnetic ordering of the lattice.

In real electronic conductors this type of interaction is difficult to realize, however in insulating magnets the combination of magnetic order and spin-orbit coupling naturally gives rise to such terms in the magnon hopping Hamiltonian.

In Chapter 2 we did not give an account of the different types of spin interactions generally present in magnets. In general, we may define the interaction of two spins through the tensor $\boldsymbol{J}$ as

$$\hat{H}_J = \vec{S}_i \boldsymbol{J} \vec{S}_j. \tag{3.31}$$

Now the exact form of $\boldsymbol{J}$ will depend on the symmetries present in the lattice. For instance, consider the case where bond-inversion is present on the lattice. Bond inversion has the effect of swapping the indices i and j, which is equivalent to transposing $\boldsymbol{J}$. In other-words bond inversion requires $\boldsymbol{J}$ to be a symmetric matrix. Therefore it could take the form

$$\boldsymbol{J} = \begin{bmatrix} J^{xx} & J^{xy} & J^{xz} \\ J^{xy} & J^{yy} & J^{yz} \\ J^{xz} & J^{yz} & J^{zz} \end{bmatrix}. \tag{3.32}$$

We are left with terms that are even under permutation of spin-indices. If the model preserves global $SU(2)$ symmetry, then the diagonal terms will be equal and the off-diagonal terms will be zero. That will leave us with the isotropic Heisenberg model,

$$\boldsymbol{J} = \begin{bmatrix} J & 0 & 0 \\ 0 & J & 0 \\ 0 & 0 & J \end{bmatrix}. \tag{3.33}$$

We can now consider what happens when interactions are allowed which break bond-inversion symmetry. All we have to do is consider a more general form of $\boldsymbol{J}$. This is accomplished by considering off-diagonal terms of the form $J^{\alpha\beta} = -J^{\beta\alpha}$, which would not have been allowed with bond-inversion symmetry. Such terms are summarized in the Dzyaloshinskii-Moriya (DM) interaction which is defined as

$$\hat{H}_{\text{DM}} = \vec{D} \cdot \vec{S}_i \times \vec{S}_j. \tag{3.34}$$

Now we can consider how these terms are expressed in a BdG Hamiltonian after a Holstein-Primakoff expansion is carried out as described in Section 2.2. We first consider the case where only the z-component of $\vec{D}$ is non-zero. This is for instance the case when our lattice has a horizontal mirror plane symmetry. In this situation $\hat{S}^z$ commutes with the DM interaction, and therefore it does not prevent the ground state of the model from being ferro-magnetically ordered. Assuming that the spins are ordered with their magnetization axes aligned we have

$$\begin{aligned} \hat{H}_{\text{DM}} &= D^z(\hat{S}_i^x \hat{S}_j^y - \hat{S}_i^y \hat{S}_j^x) & (3.35) \\ &= -2S^2 D^z \left[\left(1 - \frac{\hat{a}_i^\dagger \hat{a}_i}{2S}\right)\left(1 - \frac{\hat{a}_j^\dagger \hat{a}_j}{2S}\right)\right]^{1/2} (i\hat{a}_i^\dagger \hat{a}_j + \text{H. c.}) & (3.36) \\ &\approx -2S^2 D^z (i\hat{a}_i^\dagger \hat{a}_j + \text{H. c.}). & (3.37) \end{aligned}$$

The DM interaction originates from Anderson super-exchange with spin-orbit coupling taken into account [150], and it is time-reversal invariant, as can be seen from the way it is defined in equation (3.34). It is therefore interesting that it can give rise to an imaginary hopping, which a route to bands with non-zero Chern numbers.

The DM interaction can be thought of as acting like an effective Lorentz force on the magnons much in the same way that the actual Lorentz force would affect the electrons of the Haldane model. Its presence therefore results in a deflection of the magnon wave-packet in much the same way. To understand how this is possible without the DM interaction intrinsically breaking TR-symmetry, we can look at the sign of the interaction. In equation (3.37) we implicitly defined the magnetization axis to lie in the positive $\hat{S}^z$ direction. However, we could have equally well chosen the opposite polarization. If we had done so the result would have been

$$\hat{H}_{\mathrm{DM}} \approx 2S^2 D^z (i\hat{a}_i^\dagger \hat{a}_j + \mathrm{H.\,c.}). \tag{3.38}$$

In other words, the DM interaction acting on spin-up and spin-down magnons is equal and opposite. TR-breaking comes from the spontaneous ordering of the lattice, but intrinsically there is no reason for the bands to be Chern insulating unless there is spontaneous or polarized order. If we have spin-up and spin-down magnons existing side-by-side therefore the topology of the bands will be $\mathcal{Z}_2$ invariant similar to electrons with spin-orbit coupling.

DM interaction appears in lattices where there is no bond-inversion symmetry, and therefore it is quite common in magnetically insulating materials. As it is a relativistic effect, it is largest with heavier elements which support f electrons. The kagome lattice model is a prime example of an interesting model which allows DM and has many material realizations. Below we shall investigate its topological properties in the presence of DM and how it specifically affects the heat transport in $Lu_2V_2O_7$.

3.4 Magnon Chern insulators

The kagome lattice Heisenberg model is an important example of a magnon Chern insulator. The lattice is composed of corner sharing triangular plaquettes , as depicted on figure 3.2. Kagome planes are realized in some 2D layered structures, or in the ubiquitous pyrochlores, they can be found by taking planar cuts of the 3D structure.

In works by Mook, Henk and Mertig [10, 104] the Hamiltonian with DM interaction was considered. It can be written as

$$\hat{H} = \sum_{\langle i,j \rangle} J \vec{S}_i \cdot \vec{S}_j + \sum_{\langle i \to j \rangle} \vec{D}_{i \to j} \cdot \vec{S}_i \times \vec{S}_j - \sum h \hat{S}^z. \tag{3.39}$$

Here it is worthwhile to discuss the orientation of $\vec{D}$ dictated by symmetry. Figure 3.2 shows a kagome lattice in the plane which has horizontal mirror symmetry. We have

$$\begin{aligned} \sigma_{xy} &: \hat{S}^x \to -\hat{S}^x \\ \sigma_{xy} &: \hat{S}^y \to -\hat{S}^y \\ \sigma_{xy} &: \hat{S}^z \to \hat{S}^z. \end{aligned} \tag{3.40}$$

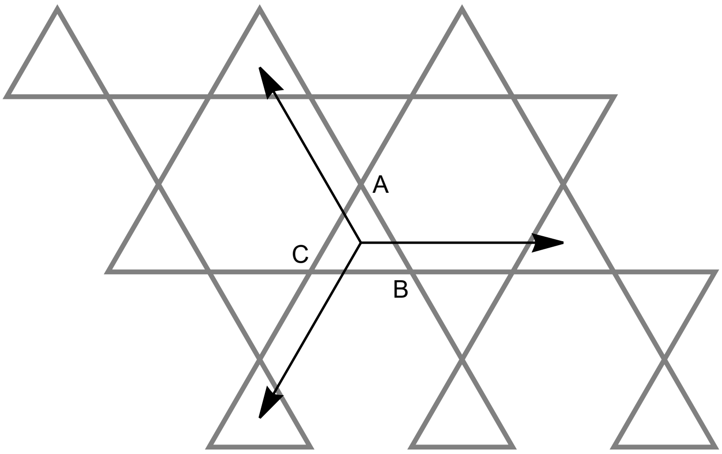

Figure 3.2: The kagome lattice with unit vectors and sublattices indicated.

When applied to the DM term, the above transformation can be absorbed into $\vec{D}$ as

$$\begin{aligned}\sigma_{xy} &: D^x \rightarrow -\hat{D}^x \\ \sigma_{xy} &: D^y \rightarrow -\hat{D}^y \\ \sigma_{xy} &: D^z \rightarrow \hat{D}^z.\end{aligned} \tag{3.41}$$

Since the Hamiltonian must be invariant under this transformation if the mirror is a symmetry of the lattice, we can only have a non-zero D^z. However, in general this may not be the case. If there is no horizontal mirror plane the transformation rules are instead determined by the C_{3v} symmetry of the lattice.

Considering first the bond connecting sublattices B and C , as seen on figure 3.2, there is a vertical mirror plane σ^{yz}, which in addition to reversing $\hat{S}^y$ and $\hat{S}^z$ also swaps B and C, so that the sign of $\vec{D}$ is reversed again. The result is that now the y and z component only are allowed.

What we have done so far is simply to restate two of Moriya's rules governing $\vec{D}$ in [150]. The vector $\vec{D}$ must lie in the mirror plane that bisects the bond between B and C. This rule is true in general of $\vec{D}$ defined on a bond which has a mirror perpendicular to the bond orientation located at its bisector. We will therefore have

$$\begin{aligned}\vec{D}_{BC} &= \hat{y}D_y + \hat{z}D_z \\ \vec{D}_{AB} &= (-\sqrt{3}/2\hat{x} - 1/2\hat{y})D_y + \hat{z}D_z \\ \vec{D}_{CA} &= (\sqrt{3}/2\hat{x} - 1/2\hat{y})D_y + \hat{z}D_z.\end{aligned} \tag{3.42}$$

If the DM vector is further constrained by some embedding geometry, such as a pyrochlore lattice, then the relationship between D_y and D_z may be fixed. This is the case for pyrochlore as pointed out in [10].

For now we consider the effect of having only a finite D_z component of the DM interaction. When the spins in the ground-state are ordered, either through spin-polarization or spontaneous ordering, the single-magnon band-theory does not express terms originated by D_y. Those terms manifest as third order terms in the spin-wave expansion, so for investigating the topology of magnon bands we neglect them.

We derive a spin-wave Hamiltonian of the form

$$\hat{H} = \sum_k \vec{v}_k^\dagger \boldsymbol{M}_k \vec{v}_k. \tag{3.43}$$

Here the vector

$$\vec{v}_k = [\hat{a}_k, \hat{b}_k, \hat{c}_k]^T \tag{3.44}$$

and

$$\boldsymbol{M}_k = \begin{bmatrix} \eta & \gamma_1^* \delta_{3,k}^* & \gamma_1 \delta_{2,k} \\ \gamma_1 \delta_{3,k} & \eta & \gamma_1^* \delta_{1,k}^* \\ \gamma_1^* \delta_{2,k}^* & \gamma_1 \delta_{1,k} & \eta \end{bmatrix} \tag{3.45}$$

with

$$\begin{aligned} \eta &= h - 2J \\ \gamma_1 &= iD_z + J \\ \delta_{i,k} &= e^{i\lambda_i \cdot k/2} \cos(\lambda_i \cdot k/2). \end{aligned} \tag{3.46}$$

The complex prefactor of each $\delta_{i,k}$ can be removed by applying a gauge transformation to the magnons, but the cost of doing so is to extend the Brillouin zone. It is for the current analysis better not to do so, as we would have to define the wavefunction as a periodic function of k on this enlarged space. In general this could contain a n additional topological charge for each original Brillouin zone it enclosed. λ_i are lattice vectors of the kagome unit cell. In units of the lattice spacing, they are

$$\begin{aligned} \lambda_1 &= [1, 0]^T \\ \lambda_2 &= [-1/2, \sqrt{3}/2]^T \\ \lambda_3 &= [-1/2, -\sqrt{3}/2]^T \end{aligned} \tag{3.47}$$

At the Γ-point of the lattice we have

$$\boldsymbol{M}_\Gamma = \begin{bmatrix} \eta & \gamma_1^* & \gamma_1 \\ \gamma_1 & \eta & \gamma_1^* \\ \gamma_1^* & \gamma_1 & \eta \end{bmatrix}. \tag{3.48}$$

The eigenenergies at this point are

$$\begin{aligned} \epsilon_0 &= \eta + 2\Re\gamma_1 = h \\ \epsilon_\pm &= \eta + 2\Re\omega^{\mp 1}\gamma_1 = h - 3J \pm \sqrt{3}D_z. \end{aligned} \tag{3.49}$$

Here $\omega = (\omega^*)^{-1} = -1/2 - i\sqrt{3}/2$. We can define a basis for this problem based on the eigenstates at the Γ-point, which are the magnon basis functions

$$\begin{aligned}\hat{\psi}_0^\dagger &= (\hat{a}_\Gamma^\dagger + \hat{b}_\Gamma^\dagger + \hat{c}_\Gamma^\dagger)/\sqrt{3}\\ \hat{\psi}_\pm^\dagger &= (\hat{a}_\Gamma^\dagger + \omega^{\pm 1}\hat{b}_\Gamma^\dagger + \omega^{\mp 1}\hat{c}_\Gamma^\dagger)/\sqrt{3}.\end{aligned} \tag{3.50}$$

The $\psi_\pm$ bands are split by the perturbative DM interaction. Although we consider the magnitude of the DM term to be lower than J it is important to note that this is not always the case as the DM interaction for 4f electrons for instance can be the dominant component [151, 152]. There is a gap of size $3J$ to the upper ψ_0 band. Near the Γ point we can therefore construct an effective two-band model to see how the DM term mixes those two bands and what it means for the topology. We first define

$$U = \begin{bmatrix} 1 & 1 & 1 \\ 1 & \omega & \omega^* \\ 1 & \omega^* & \omega \end{bmatrix} /\sqrt{3}. \tag{3.51}$$

In this basis the kernel matrix is

$$\tilde{\boldsymbol{M}}_k = U\boldsymbol{M}_k U^\dagger \tag{3.52}$$

We extract the low-energy subspace by projecting down onto the lower right 2×2 block of this matrix. Doing so gives us

$$\tilde{\boldsymbol{M}}_{\text{eff},k} = (h - (2 + \delta_k/3)J)I + \vec{d}(\vec{k}) \cdot \vec{\sigma}, \tag{3.53}$$

where

$$\vec{d}(\vec{k}) = \begin{bmatrix} J/3(2\cos(\lambda_1 \cdot k) - \cos(\lambda_2 \cdot k) - \cos(\lambda_3 \cdot k)) \\ J/3(-\sqrt{3}\cos(\lambda_2 \cdot k) + \sqrt{3}\cos(\lambda_3 \cdot k)) \\ \sqrt{3}(D_z\delta_k + J\tilde{\delta}_k) \end{bmatrix}. \tag{3.54}$$

Here

$$\begin{aligned}\delta_k &= \frac{1}{3}\sum_i \cos^2(\lambda_i \cdot k/2)\\ \tilde{\delta}_k &= \frac{1}{3}\sum_i \sin(\lambda_i \cdot k/2)\cos(\lambda_i \cdot k/2)\end{aligned} \tag{3.55}$$

This effective field model is only valid close to the Γ-point where the energy separation between the lower bands and the top one is large. We therefore cannot at the moment say exactly what happens throughout the entire Brillouin zone, but we can infer the existence of a topological charge.

We can analyze the equations of this field for $D_z \ll J$. In the vicinity of the Γ point, the third component of $\vec{d}$ is to a good approximation a constant $\sqrt{3}D_z$. The first and second component can be found through a second order expansion in k.

We obtain the approximate

$$\vec{d}(\vec{k}) \approx \begin{bmatrix} \frac{J}{32}({k_x}^2 - {k_y}^2 + \sqrt{3}k_x k_y) \\ \frac{J}{32}(\sqrt{3}{k_x}^2 - \sqrt{3}{k_y}^2 - k_x k_y) \\ \sqrt{3}D_z \end{bmatrix} \tag{3.56}$$

The asymptotic form of the above field is that of a doubly-wound vortex. In other words, if we fix $|\vec{k}|$ at a sufficiently large value and draw the resulting $\vec{d}$ on the circle, it will wind twice around the equator of the Bloch sphere. If D_z is small compared to J then this asymptotic form will be reached close to Γ. However at the Γ-point $\vec{d}$ will be oriented to the north pole of the Bloch sphere.

In Section B.1 we describe this scenario, where due to a broken symmetry (in this case bond-inversion) a perturbative interaction can add a finite third component to $\vec{d}$ resulting in a Berry phase

$$\gamma_\pm = \pm\pi n \tag{3.57}$$

Here n is the winding number of the polar angle $\phi(\vec{k})$, which in the above case is 2.

This rudimentary analysis suggests that the bands are each endowed a Berry curvature that integrates to $\pm 2\pi$. If there are no further contributions to the Berry curvature on the given band, then this is sufficient to obtain the Chern number of each band. However, we also have to consider topological charges elsewhere in the Brillouin zone. Although the case described here is the one where $D_z \ll J$, as long as the bands do not close, the topology will remain the same.

At the K and K' points we may carry out a similar analysis. Here the kernel Matrix is

$$\boldsymbol{M}_{\pm K} = \begin{bmatrix} \eta & \gamma_1^* \omega^{\mp 1/2}/2 & \gamma_1 \omega^{\pm 1/2}/2 \\ \gamma_1 \omega^{\pm 1/2}/2 & \eta & \gamma_1^* \omega^{\mp 1/2}/2 \\ \gamma_1^* \omega^{\mp 1/2}/2 & \gamma_1 \omega^{\pm 1/2}/2 & \eta \end{bmatrix}. \tag{3.58}$$

The basis we defined earlier again diagonalizes the Hamiltonian. At the K and K' points we retain the C_3 subgroup of the $C_{3v}(C_3)$ magnetic point group governing the lattice. When applied to the magnon wave-function this has identical basis functions, which is why the Hamiltonian is diagonalized in the same way.

The eigenenergies are

$$\begin{aligned} \epsilon_\pm &= h - 5J/2 \pm \sqrt{3}D_z/2 \\ \epsilon_0 &= h - 3J. \end{aligned} \tag{3.59}$$

It is now the two higher energy bands that are gapped by the DM interaction. We may again expand $\tilde{\boldsymbol{M}}_k$ in k, however this time the dispersion around the gap is linear. We find to first order in k

$$\vec{d}(\vec{k}) = \begin{bmatrix} \beta J k_x + \alpha J k_y \\ -\alpha J k_x + \gamma J k_y \\ \frac{\sqrt{3}}{2} D_z \end{bmatrix}. \tag{3.60}$$

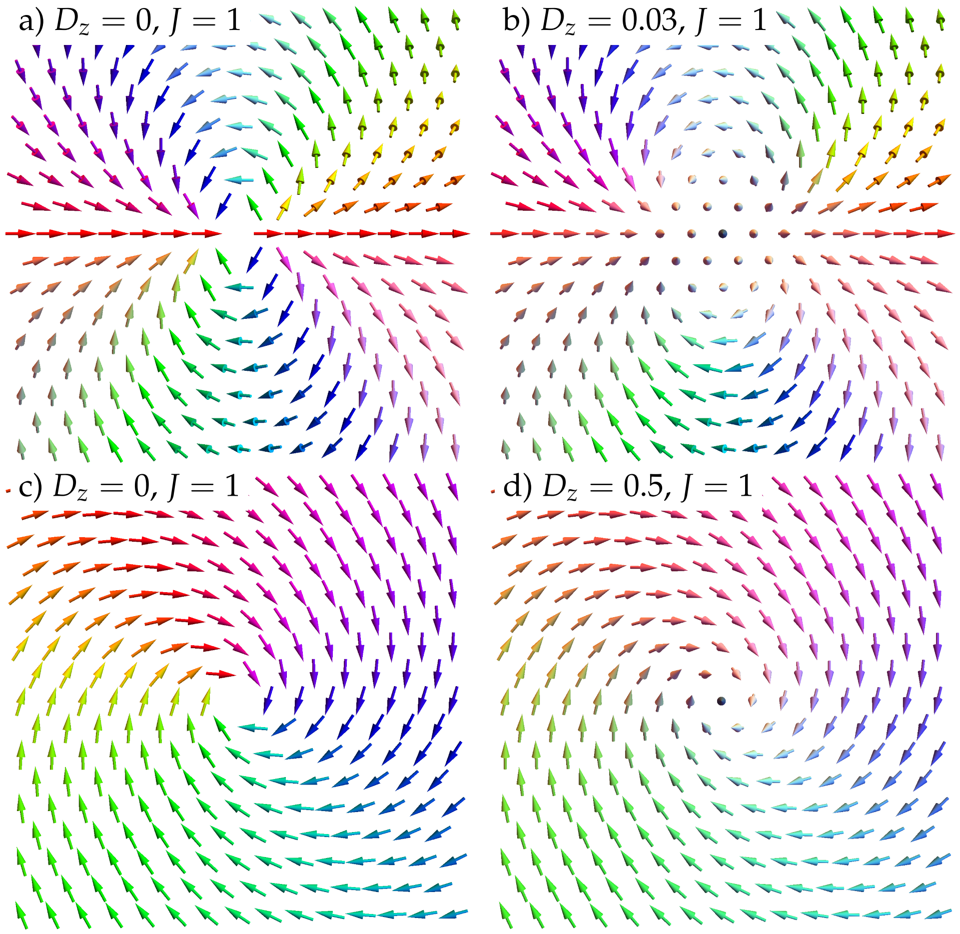

Figure 3.3: We plot the effective field $\vec{d}$ in the vicinity of the Γ-point (a-b) and the K, K'-points (c-d) respectively with a finite DM interaction (b), (d). Note that $\vec{d}$ winds twice around the Γ-point, whereas it winds a single time around K and K'.

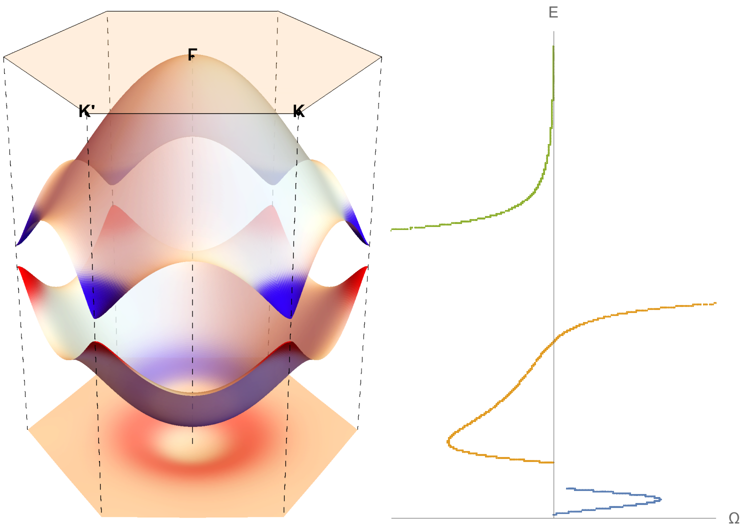

Figure 3.4: (Left) we here plot the magnon bands of the kagome lattice with $J = 1$, $D_z = 0.1$ and $h = 5$. The bands are colored according to the local Berry curvature. (Right) The Berry curvature pr. unit energy is plotted here for the bands pictured.

Here we have made use of the parameters

$$\begin{aligned} \alpha &= \frac{3}{8} + \frac{\pi}{36\sqrt{3}} \\ \beta &= -\frac{\sqrt{3}}{8} + \frac{\pi}{36} \\ \gamma &= -\frac{\sqrt{3}}{8} - \frac{\pi}{48}. \end{aligned} \tag{3.61}$$

The texture drawn out by $\vec{d}(\vec{k})$ here winds once around the K point. It therefore contributes $\pm\pi$ to each band. The same texture exists at the K' point though, and it is define on those same bands. It therefore contributes the same Berry curvature which in total integrates up to $\pm 2\pi$. However, here it is the top band which now gains a Chern number $+1$, whereas the middle band gains -1. Therefore the total Chern number is now expected to be 0 for the middle band, where the top and bottom band get $+1$ and -1 respectively.

In figure 3.4 we plot the magnon bands of the spin-polarized kagome with $J = 1$, $D_z = 0.1$ and $h = 5$. The bands are colored according to the local Berry curvature. We note that the Berry curvature is concentrated near the band-gaps. Additionally the middle band, while having a Berry curvature which integrates up to 0 is distributed comparatively broadly in energy-space. The lower part of the band will carry a higher statistical weight and therefore contribute more to the thermal Hall coefficient. The Berry curvature of a two-band effective mode is given by

$$F_{\pm,\theta\phi} = \pm\frac{\sin\theta}{2}. \tag{3.62}$$

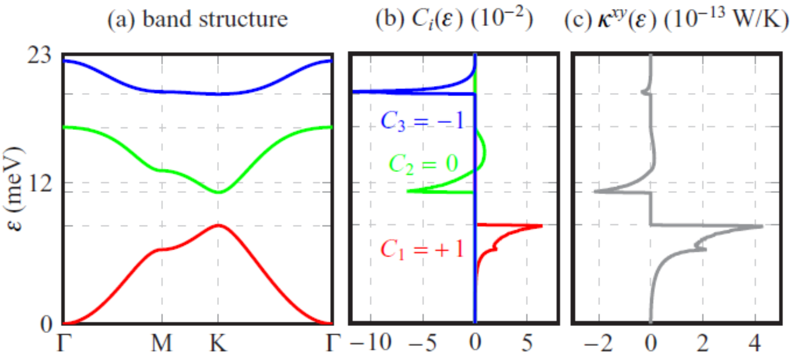

Figure 3.5: Topologically non-trivial magnon bands of the kagome magnet with Dzyaloshinskii-Moriya interaction is shown here. (a) The dispersion relation with high symmetry points indicated. (b) The Chern numbers are indicated as well as the Berry curvature of each band. (c) Here the contributions of each band pr. unit energy to the transverse conductance is shown. Figure reproduced from [10].

Here θ is the azimuthal angle that $\vec{d}$ makes with the origin. In our effective models on kagome D_z is a constant coefficient of σ_3. Therefore, we can reason that the Berry curvature will be highly concentrated around the high symmetry points in the cases where $D_z \approx 0$. Now if the Berry curvature is highly concentrated near a band-gap and each of the bands carry equal and opposite curvature, while the band-gap itself is small, then the contributions to the thermal Hall coefficient given by each band will in the extreme case cancel out. We therefore see in contrast to the electronic systems that there is here a gradual dependence of the Hall coefficient on system parameters and it will in general vary smoothly from 0 when a topological band-gap appears.

In summary, we can view each band-gap as defining a surface $\vec{d}(\vec{k})$ through which the flux of a topological charge centered at the origin determines the Berry curvature. If the gap is closed, then $\vec{d}(\vec{k})$ must at some point intersect the origin, and the flux intersecting it is zero. Passing through this point completely inverts the flux as we see in the above examples with kagome. This intuition gives us a way to understand and predict the Chern numbers arising on each band. However, the above expressions are only approximate solutions near the band-gap and Chern numbers are a global property of each band, which is obtained from integrating the Berry curvature throughout the Brillouin zone. It is also possible to have a Berry curvature that does not integrate up to 0, but here unlike in the electron band-theory this may still cause a finite Hall effect.

3.4.1 The thermal Hall effect of $Lu_2V_2O_7$

In electronic band-theory the quantum Hall-effect is a consequence of the Berry curvature integrating up to an integral multiple of 2π as well as the fact that occupation of each band is determined by Fermi statistics. In response to an applied voltage the conductivity is related to the Chern number through TKNN's formula [60].

In the case of bosonic chargeless excitations, although they do not give rise to

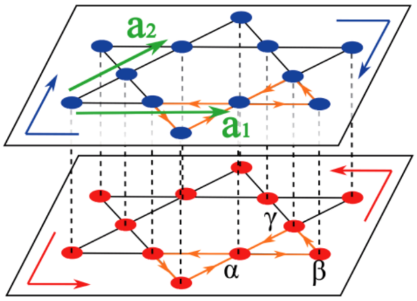

Figure 3.6: This figure shows the bilayer kagome lattice with staggered magnetic order. Figure reproduced from [13].

an electronic current, a heat gradient will result in a flow of energy mediated by magnon excitations. This energy flow too will be subject to a Lorentz force determined by the Berry curvature. As stated in Chapter 1 this is given by the thermal Hall coefficient

$$\kappa^{xy} = \frac{2k_B^2 T}{\hbar V} \sum_{n,\mathbf{k}} c_2(\rho_n)\Omega_{n,k}. \tag{3.63}$$

Here the Boltzmann factor of the n'th band is ρ_n. It must be enveloped by the function c_2 which is found by solving

$$c_q(\rho_n) = \int_0^{\rho_n} (\log \frac{1+t}{t})^q dt. \tag{3.64}$$

Even without the c_2 function, this expression does not yield $2\pi n$ due to a topological band-gap. This was explained elegantly in [10]. In figure 3.5 the band-structure of the kagome is depicted. In the vicinity of each gap the Berry curvature is sharply peaked, however the thermal activation of the magnon bands depends on the temperature and therefore the bands do not contribute equally. In fact the second band, which has a Chern number of 0 gives a finite non-zero contribution to k^{xy}, which can be seen by plotting the energy density of k^{xy} as it is distributed on this band. In [10] κ^{xy} is compared with the experimental study of $Lu_2V_2O_7$ carried out by Onose et. al. in [9], and it is shown to exhibit the same field dependence. Importantly, it also switches sign with the field, and there is a sharp transition at exactly zero field.

3.5 In search of $\mathcal{Z}_2$ index for magnetic insulators

Spontaneous TR symmetry breaking together with spin-orbit coupling results in the complex hopping of magnons needed for them to display a thermal Hall effect. They do so in analogy to the quantum Hall effect of electrons and we can map the hopping Hamiltonian of the magnons to the Haldane model. Remarkably the interactions needed are not that uncommon in magnetic insulators. The Haldane model in contrast requires some kind of exotic magnetic order. In some sense the magnetic analogue of the Haldane model is therefore more realistic.

A natural next question is then what happens if TR symmetry is unbroken? Is there a way to also realize an analogue of the Kane and Mele model and a quantum spin Hall state in magnetic insulators? For this to happen, we require a model which hosts both spin lowering and raising excitations. We also require some kind of symmetry which acts to define pairs of these excitations, similar to Krämers pairs of electrons and thereby prevent them from hybridizing. However, magnons by definition only appear in TR breaking models. In place of TR symmetry there could be some other symmetry operation that protects them.

In [13] the question of what this symmetry operator is was considered for bilayer magnetic insulators with staggered magnetic order. Here the layers are coupled with an antiferromagnetic exchange interaction which ensures that the spontaneously ordered state has opposite magnetization on each layer. Thereby the imaginary component of hopping caused by the DM interaction will have opposite signs for each layer, and in effect, they realize two Chern insulators with an opposite thermal Hall effect. However, we can consider that they necessarily contribute the same spin-current. As depcited in figure 3.6, the bilayer kagome with staggered ferromagnetic order supports spin-down magnons in the top layer and spin-up magnons in the bottom layer. If a temperature gradient is applied to the material the top layer will contribute a thermal Hall signal which is opposite to the bottom one because the excitations experience an opposite deflection due to the Berry curvature. However, since they also carry opposite spin, they contribute the same spin-Hall signal.

In general we can consider the BdG Hamiltonian of a bilayer lattice to be of the form

$$\hat{H} = \sum_k \vec{v}_k^\dagger \boldsymbol{M}_k \vec{v}_k \tag{3.65}$$

Here

$$\vec{v}_k^\dagger = \left[\hat{a}^\dagger_{\uparrow,0,k}, \hat{a}^\dagger_{\uparrow,1,k}, \ldots, \hat{a}_{\downarrow,N,-k}\right]. \tag{3.66}$$

The operator $\hat{a}^\dagger_{\sigma,i,k}$ creates a magnon on the σ layer's ith sublattice with quasi-momentum k.

On the space of these magnon wavefunctions, we can define the pseudo-time-reversal (PTR) operator by its matrix form

$$\Theta = (\sigma_z \otimes i\sigma_y \otimes \boldsymbol{I}_{N+M})K. \tag{3.67}$$

Here the Pauli matrix σ_z acts on the particle-hole space of the BdG Hamiltonian whereas σ_y acts to interchange the two layers and K is complex conjugation. The identity operator acts on N spin-up and M spin-down sublattices of the bottom layer. In the top layer these spins are reversed.

Clearly $\Theta^2 = -1$, as opposed to TR which for bosons squares to 1. Now, requiring that $-\hat{\Theta}\hat{H}_k\hat{\Theta} = \hat{H}_{-k}$ is in matrix form expressed as

$$-\Theta\Sigma_z \boldsymbol{M}_k \Theta = \Sigma_z \boldsymbol{M}_{-k}. \tag{3.68}$$

Here

$$\Sigma_z = \begin{bmatrix} \boldsymbol{I}_{2(N+M)} & 0 \\ 0 & -\boldsymbol{I}_{2(N+M)} \end{bmatrix}. \tag{3.69}$$

The most general Hamiltonian allowed by equation (3.68) is given by

$$\boldsymbol{M}_k = \begin{bmatrix} h_1(k) & h_2(k) & \Delta_2(k) & \Delta_1(k) \\ h_2(k)^\dagger & h_1^*(-k) & \Delta_1^*(-k) & -\Delta_2^\dagger(k) \\ \Delta_2^\dagger(k) & \Delta_1^*(-k) & h_1^*(-k) & h_2^*(-k) \\ \Delta_1(k) & -\Delta_2(k) & h_2^T(-k) & h_1(k) \end{bmatrix} \tag{3.70}$$

An example of an ordered state which we can apply this operator to is the bilayer kagome lattice ferromagnet with interlayer antiferromagnetic interactions. Here the ground state is ordered such that the top layer has spins aligned ferromagnetically in the positive $\hat{S}^z$ direction and the bottom layer is ordered oppositely.

The $h_1(k)$ block corresponds to the kernel matrix derived earlier for the monolayer kagome, i.e.

$$h_1(k) = \begin{bmatrix} \eta & \gamma_1^* \delta_{3,k}^* & \gamma_1 \delta_{2,k} \\ \gamma_1 \delta_{3,k} & \eta & \gamma_1^* \delta_{1,k}^* \\ \gamma_1^* \delta_{2,k}^* & \gamma_1 \delta_{1,k} & \eta \end{bmatrix}. \tag{3.71}$$

The difference here being the diagonal $\eta = 2J + J'$, where J and J' are the ferromagnetic and anti-ferromagnetic coupling respectively.

Since the bottom lattice magnons have a hopping Hamiltonian given by $h_1^*(-k)$, it is as though they simply have an opposite DM interaction. This is enforced by the PTR symmetry. The block coupling the two layers is $h_2(k)$. This matrix is in general non-zero, even when PTR is included. It is worth considering the case where $h_2(k) = 0$ though. We also require that the Δ_1 blocks are zero.

As there are no matrix elements connecting the top and bottom layer magnons, the two layers are effectively disconnected. Each realizes a magnon Chern insulator with an exactly opposite κ_{xy} due to psuedo-time-reversal symmetry. This is the simplest sense in which we can realize $\mathcal{Z}_2$ topology. In the Chern insulators a topological band-gap was associated with an edge-mode which connects the two bulk gaps. In this case the bulk gaps are composed of degenerate ↓ and ↑ magnons, each of which carries an edge-mode. The edge-modes are partners connected by PTR and because of this they carry opposite quasi-momentum, but are degenerate. Following the approach of [13] we can write the Berry connection and curvature of each PTR pair as

$$\mathbf{A}_{n,\sigma}(\mathbf{k}) = \sum_{l=1,2} \mathbf{A}_{n,l,\sigma}(\mathbf{k}), \tag{3.72}$$

$$\Omega_{n,\sigma}(\mathbf{k}) = \sum_{l=1,2} \Omega_{n,l,\sigma}(\mathbf{k}). \tag{3.73}$$

Here the sum of the Berry connection and curvature is taken over each layer. The band index is n and the particle-hole index is σ. The $\mathcal{Z}_2$ index may then be calculated as

$$D_{n,\sigma} = \frac{1}{2\pi} \left[\oint_{\partial \mathrm{EBZ}} d\mathbf{k} \cdot \mathbf{A}_{n,\sigma}(\mathbf{k}) - \int_{\mathrm{EBZ}} d^2 k \Omega_{n,\sigma}(\mathbf{k}) \right] \qquad \mathrm{mod}\ 2 \tag{3.74}$$

Here EBZ refers to the effective Brillouin zone, which has half the area of the first

Brillouin zone. Each point in EBZ is associated with a time reversed point outside of EBZ, which when taken together defines the full Brillouin zone.

The $\mathcal{Z}_2$ index defined here is valid also in the case where $\hat{S}^z$ is not a good quantum number (in contrast to the spin Chern number which we define in Chapter 4). and it also gives a rather intuitive view of the $\mathcal{Z}_2$ index in terms of the pseudo-Krämer's pairs' Berry curvature and Berry connection. Another formulation can be taken by considering the matrix elements of the PTR operator.

$$\begin{aligned} \langle \psi_i(-k)|\Sigma_z\Theta|\psi_j(k)\rangle &= -\langle \psi_j(-k)|\Sigma_z\Theta|\psi_i(k)\rangle && (3.75)\\ &= P(k). && (3.76) \end{aligned}$$

Here the ψ_i is the ith band wave-function. Each band defines a 2×2 subspace whose components can be connected by PTR. Especially, at the pseudo-time-reversal invariant points where $H(k) = H(-k)$, $|P(k)| = 1$. In the general case the zeros of $P(k)$ must be counted for each band l. From the definition of $P(k)$ it is easily seen that a zero at k^* implies an additional zero at $-k^*$. The number of pairs of zeros modulo 2 is a topological invariant of $P(k)$. The reason is that each zero defines a vorticity in $P(k)$, which will be opposite at each $\pm k^*$. A single pair of zeros cannot annihilate unless they cross through a time-reversal invariant point, but at these points $|P(k)| = 1$ trivially, so an uneven number of pairs of zeros can never annihilate. This feature is protected by PTR symmetry.

Although this in principle puts the PTR for magnons on even footing with TR for electrons, it is unclear what physical symmetries actually result in a PTR operator. In fact, for the bilayer kagome model presented here, in general anisotropic terms are allowed which break PTR symmetry, while not breaking TR symmetry. This destroys the $\mathcal{Z}_2$ topology of the bands in the given problem. How exactly the PTR symmetry can be realized is the subject of Chapter 4 where we study this in the context of a bond-wave Hamiltonian describing a quantum paramagnet on a bilayer kagome lattice.

Chapter 4

Bilayer kagome quantum paramagnet with triplon $\mathcal{Z}_2$ topology

As we have seen in Chapter 3 the Dzyaloshinskii Moriya interaction in a magnet can generate a complex hopping, which acts similarly to the complex hopping of electrons in the Haldane model [150]. By analyzing the bands it is clear that they thereby obtain a non-trivial topology [104]. It could thus be said that these magnets facilitate a bosonic version of the Haldane model. A natural next question is then whether a bosonic version of the Kane and Mele model also exists.

It has been proposed in previous works that such a system should exist in a bilayer honeycomb lattice [130] where it could be mediated by triplet excitations or by conventional magnons in bilayer kagome or honeycomb lattices [13]. We may then imagine that these systems could be accompanied by a spin Nernst effect, in analogy to the spin-Hall effect of the Kane and Mele model.

In this chapter we propose a similar triplet bond-wave system, however, we take into account a more general Hamiltonian than [130], where many more symmetry allowed interactions are present. By doing so we find that for the bilayer kagome magnet the $\mathcal{Z}_2$ topological phase breaks down. This is in-spite of the model being TR symmetric. Additionally we investigate the pseudo-time-reversal operator that would be needed to protect the $\mathcal{Z}_2$ topology in analogy to how TR protects it in the Kane and Mele model.

The results described in this chapter are accessible in the preprint [1].

4.1 Symmetry allowed interactions

The point group symmetry of the bilayer kagome lattice we consider is isomorphic to D_{6h}. In figure 4.1 this is indicated graphically. The structure of the lattice is depicted along with the symmetry operators which make up D_{6h}. The bilayer kagome lattice has three sub-lattices A, B and C, and we define an index which specifies the layers too.

In table 4.1 we list the generators of this group and their action on components of spin as well as the sub-lattice and layer indices.

We now treat the symmetry allowed exchange terms of the Hamiltonian. We

Table 4.1: We list the generators of D_{6h}

Generator	E	C_6	C_2	σ_h
Spin component	$\hat{S}^x$	$\frac{1}{2}\hat{S}^x + \frac{\sqrt{3}}{2}\hat{S}^x$	$\hat{S}^x$	$-\hat{S}^x$
	$\hat{S}^y$	$-\frac{\sqrt{3}}{2}\hat{S}^x + \frac{1}{2}\hat{S}^y$	$-\hat{S}^y$	$-\hat{S}^y$
	$\hat{S}^z$	$\hat{S}^z$	$-\hat{S}^z$	$\hat{S}^z$
Dimer label	A	C′	B	A
	B	A′	A	B
	C	B′	C	C
	A′	C	B′	A′
	B′	A	A′	B′
	C′	B	C′	C′
Layer index	1	1	2	2
	2	2	1	1

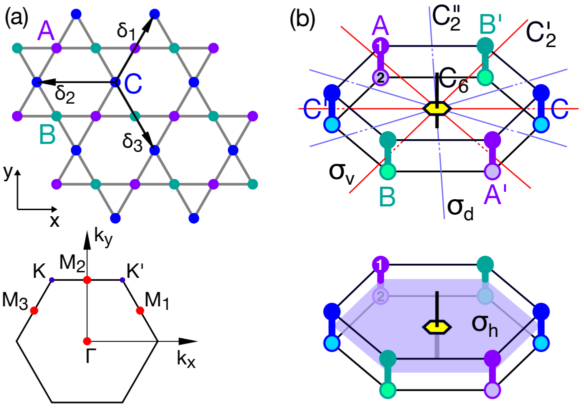

Figure 4.1: The bilayer kagome lattice. (a) is the top-down view of the bilayer lattice with lattice vectors δ_i indicated as well as the high-symmetry points of the Brillouin zone defined by them. (b) shows the point group symmetries. C_6 rotational symmetry about the center of the kagome hexagon is indicated. Red and blue lines going through this centerpoint define simultaneously the C_2 axes of rotation and vertical planes of reflection. Also indicated is the horizontal plane of reflection σ_h.

will examine interactions which are quadratic in spin-operators. We require that the Hamiltonian transforms according to the A1 irreducible representation of the group. This is ensured if

$$\sum_{g\in D_{6h}} g:\hat{H} = \sum_{g\in D_{6h}} \Gamma^{A}(g)\hat{H}\Gamma^{A}(g)^{-1} \tag{4.1}$$

$$= n\hat{H}, \tag{4.2}$$

where n is the order of the group and A is any representation of the group, for instance matrices acting on the spin-space of the kagome lattice. The Hamiltonian can be written as

$$\hat{H} = \hat{H}_{XXZ} + \hat{H}_{\text{DM}} + \hat{H}_{\text{Nematic}}. \tag{4.3}$$

Here the term $\hat{H}_{XXZ}$ contains the diagonal of the tensor, with the $\hat{S}^x\hat{S}^x$ and $\hat{S}^y\hat{S}^y$ terms given equal weight. $\hat{H}_{\text{DM}}$ includes the Dzyaloshinskii-Moriya terms, which form the anti-symmetric part of the exchange tensor. Finally the $\hat{H}_{\text{Nematic}}$ includes anisotropic terms which are invariant under bond-inversion. They include terms composed of the bond-nematic operators

$$\begin{aligned}
\hat{Q}^{x^2-y^2}_{i,j} &= \hat{S}^x_i\hat{S}^x_j - \hat{S}^y_i\hat{S}^y_j \\
\hat{Q}^{xy}_{i,j} &= \hat{S}^x_i\hat{S}^y_j + \hat{S}^y_i\hat{S}^x_j \\
\hat{Q}^{yz}_{i,j} &= \hat{S}^y_i\hat{S}^z_j + \hat{S}^z_i\hat{S}^y_j \\
\hat{Q}^{zx}_{i,j} &= \hat{S}^z_i\hat{S}^x_j + \hat{S}^x_i\hat{S}^z_j .
\end{aligned} \tag{4.4}$$

Below we elucidate which terms are allowed on each bond. The determination of each of these terms is carried out by going through the point group elements of D_{6h} with each term required to obey equation (4.2).

4.1.1 Intra-dimer bonds

The vertical bonds which connect the layers will be referred to as the "dimers" of the lattice. These dimers have contributions from the XXZ anisotropy

$$\hat{H}^{\vdots}_{XXZ} = J_{\|}\sum_j(\hat{S}^x_{j1}\hat{S}^x_{j2} + \hat{S}^y_{j1}\hat{S}^y_{j2}) + J_{\perp}\sum_j\hat{S}^z_{j1}\hat{S}^z_{j2}. \tag{4.5}$$

Additionally intra-dimer nematic terms are allowed

$$\hat{H}^{\vdots}_{\text{nematic}} = K_{\|}\sum_j \mathbf{n}_j\cdot\mathbf{Q}^{\|}_{j1,j2}. \tag{4.6}$$

Here $\hat{Q}^{\|}_{i,j} = (\hat{Q}^{x^2-y^2}_{i,j}, \hat{Q}^{xy}_{i,j})$. The unit vectors $\mathbf{n}_j$ depend on the sub-lattice index. They are

$$\begin{aligned}\mathbf{n}_A &= \left(\frac{1}{2}, \frac{\sqrt{3}}{2}\right)\\ \mathbf{n}_B &= \left(\frac{1}{2}, -\frac{\sqrt{3}}{2}\right)\\ \mathbf{n}_C &= (-1, 0).\end{aligned} \tag{4.7}$$

There is no contribution from the DM-interaction as there is an inversion center on each bond. By Moriya's rules DM interaction is therefore not allowed on these bonds. We thus find that there are in total three independent parameters determining the interactions on the dimers.

4.1.2 Inter-dimer nearest neighbor bonds

On the inter-dimer nearest neighbor bonds the Heisenberg terms have two independent components

$$\hat{H}^{\text{1st}}_{\text{XXZ}} = J'_{\|} \sum_{\substack{\langle i,j\rangle\\ l=1,2}} (\hat{S}^x_{il}\hat{S}^x_{jl} + \hat{S}^y_{il}\hat{S}^y_{jl}) + J'_{\perp} \sum_{\substack{\langle i,j\rangle\\ l=1,2}} \hat{S}^z_{il}\hat{S}^z_{jl}. \tag{4.8}$$

Additionally there are two components to the DM interaction. They are

$$\hat{H}^{\text{1st}}_{\text{DM}} = D'_{\perp} \sum_{\substack{\langle i,j\rangle\\ l=1,2}} \hat{z} \cdot \mathbf{S}_{il} \times \mathbf{S}_{jl} + D'_{\|} \sum_{\substack{\langle i,j\rangle\\ l=1,2}} \mathbf{n}_{il,jl} \cdot \mathbf{S}_{il} \times \mathbf{S}_{jl} \tag{4.9}$$

The out of plane component is simply the third component of $\mathbf{D}$, which is the same for all nearest neighbor bonds. The rules governing the unit vectors $\mathbf{n}_{il,jl}$ in the above expression are that they must lie in the x, y-plane and that they must be perpendicular to the orientation of the il, lj bond. Additionally the vectors must be related to each other by c_6 rotations and in each layer they must have opposite orientations.

There are two symmetry allowed components of the nematic interaction. The first one is the *in-plane* component defined by

$$\hat{H}^{\text{1st}}_{\text{nematic},\|} = K'_{\|} \sum_{\substack{\langle i,j\rangle\\ l=1,2}} \mathbf{n}_{i,j} \cdot \mathbf{Q}^{\|}_{il,jl}. \tag{4.10}$$

The vector $\mathbf{Q}^{\parallel}_{il,jl}$ has the same form as before. The unit vectors now have the form

$$\begin{aligned} \mathbf{n}_{AB'} &= \mathbf{n}_{A'B} = (-1, 0) \\ \mathbf{n}_{BC'} &= \mathbf{n}_{B'C} = \left(\frac{1}{2}, \frac{\sqrt{3}}{2}\right) \\ \mathbf{n}_{CA'} &= \mathbf{n}_{C'A} = \left(\frac{1}{2}, \frac{-\sqrt{3}}{2}\right). \end{aligned} \tag{4.11}$$

Finally the *out-of-plane* component is

$$\hat{H}^{\mathrm{1st}}_{\mathrm{nematic},\perp} = K'_{\perp} \sum_{\substack{\langle i,j \rangle \\ l=1,2}} \mathbf{n}_{i,j} \cdot \mathbf{Q}^{\perp}_{il,jl}. \tag{4.12}$$

Here $\mathbf{Q}^{\perp}_{i,j} = (\hat{Q}^{yz}_{i,j}, \hat{Q}^{zx}_{i,j})$. But now the vectors are

$$\begin{aligned} \mathbf{n}_{AB'} &= -\mathbf{n}_{A'B} = (-1)^{l}(-1, 0) \\ \mathbf{n}_{BC'} &= -\mathbf{n}_{B'C} = (-1)^{l}\left(\frac{1}{2}, \frac{\sqrt{3}}{2}\right) \\ \mathbf{n}_{CA'} &= -\mathbf{n}_{C'A} = (-1)^{l}\left(\frac{1}{2}, \frac{-\sqrt{3}}{2}\right). \end{aligned} \tag{4.13}$$

The interaction is opposite in the two-layers as we indicate with the inclusion of a factor $(-1)^{l}$. In total we obtain 6 independent parameters which govern the interaction on these bonds.

4.1.3 Inter-dimer next-nearest neighbor bonds

Additionally we considered the effect of next-nearest neighbor interactions. They can be defined very similarly to the nearest-neighbor ones. The Heisenberg terms are

$$\hat{H}^{\mathrm{2nd}}_{XXZ} = J''_{\parallel} \sum_{\substack{\langle\langle i,j \rangle\rangle \\ l=1,2}} (\hat{S}^{x}_{il}\hat{S}^{x}_{jl} + \hat{S}^{y}_{il}\hat{S}^{y}_{jl}) + J''_{\perp} \sum_{\substack{\langle\langle i,j \rangle\rangle \\ l=1,2}} \hat{S}^{z}_{il}\hat{S}^{z}_{jl}. \tag{4.14}$$

Additionally there are two independent components to the DM interaction. They are

$$\hat{H}^{\mathrm{2nd}}_{\mathrm{DM}} = D''_{\perp} \sum_{\substack{\langle\langle i,j \rangle\rangle \\ l=1,2}} \hat{z} \cdot \mathbf{S}_{il} \times \mathbf{S}_{jl} + D''_{\parallel} \sum_{\substack{\langle\langle i,j \rangle\rangle \\ l=1,2}} \mathbf{n}_{il,jl} \cdot \mathbf{S}_{il} \times \mathbf{S}_{jl}. \tag{4.15}$$

Once again the out of plane component $D''_{\perp}$ is the same for all of these bonds. The rules governing the unit vectors $\mathbf{n}_{il,jl}$ in the above expression follow the same rules as before, but because the next-nearest neighbor bonds are oriented at different angles, these vectors in general will be different.

We again have an in-plane and an out-of-plane component of the nematic interaction. The in-plane component is

$$\hat{H}^{\text{2nd}}_{\text{nematic},\|} = K''_{\|} \sum_{\substack{\langle\langle i,j\rangle\rangle \\ l=1,2}} \mathbf{n}_{i,j} \cdot \mathbf{Q}^{\|}_{il,jl}. \tag{4.16}$$

The unit vectors are

$$\begin{aligned} \mathbf{n}_{AB} &= \mathbf{n}_{A'B'} = (1,0) \\ \mathbf{n}_{BC} &= \mathbf{n}_{B'C'} = \Big(-\frac{1}{2}, -\frac{\sqrt{3}}{2}\Big) \\ \mathbf{n}_{CA} &= \mathbf{n}_{C'A'} = \Big(-\frac{1}{2}, \frac{\sqrt{3}}{2}\Big). \end{aligned} \tag{4.17}$$

The out of plane component is

$$\hat{H}^{\text{2nd}}_{\text{nematic},\perp} = K''_{\perp} \sum_{\substack{\langle\langle i,j\rangle\rangle \\ l=1,2}} \mathbf{n}_{i,j} \cdot \mathbf{Q}^{\perp}_{il,jl}. \tag{4.18}$$

Again $\mathbf{Q}^{\perp}_{i,j} = (\hat{Q}^{yz}_{i,j}, \hat{Q}^{zx}_{i,j})$. But now the vectors are

$$\begin{aligned} \mathbf{n}_{AB} &= -\mathbf{n}_{A'B'} = (-1)^l(1,0) \\ \mathbf{n}_{BC} &= -\mathbf{n}_{B'C'} = (-1)^l\Big(-\frac{1}{2}, -\frac{\sqrt{3}}{2}\Big) \\ \mathbf{n}_{CA} &= -\mathbf{n}_{C'A'} = (-1)^l\Big(-\frac{1}{2}, \frac{\sqrt{3}}{2}\Big). \end{aligned} \tag{4.19}$$

4.2 Triplon BdG Hamiltonian

We showed in Section 2.3 that the Heisenberg interaction energy of a dimer can be minimized by choosing a singlet state thereby minimizing the collective spin of the dimer. We consider again this approach for our bilayer kagome lattice, but this time focusing on the bonds connecting each layer.

The dominant interaction terms are the Heisenberg exchange terms $\hat{H}_{XXZ}$. These terms all commute with the dimer magnetization, $\hat{S}^z_{i,\vdots} = \hat{S}^z_{i,1} + \hat{S}^z_{i,2}$. Therefore in the limit of strong Heisenberg interaction the eigenstates must be singlets or triplets. If the interactions are anti-ferromagnetic, then the lowest energy state will be the singlet and the triplet states will form dispersive excitations on top of a singlet covered lattice. These excitations are commonly known as triplons, and we will refer to them as such. We therefore express this problem in the basis

$$
\begin{aligned}
\hat{s}_i^\dagger \left|0\right\rangle &= \left|s\right\rangle_i = (\left|\uparrow_1, \downarrow_2\right\rangle_i - \left|\downarrow_1, \uparrow_2\right\rangle_i)/\sqrt{2} \\
\hat{t}_{1,i}^\dagger \left|0\right\rangle &= \left|t_1\right\rangle_i = \left|\uparrow_1, \uparrow_2\right\rangle_i \\
\hat{t}_{0,i}^\dagger \left|0\right\rangle &= \left|t_0\right\rangle_i = (\left|\uparrow_1, \downarrow_2\right\rangle_i + \left|\downarrow_1, \uparrow_2\right\rangle_i)/\sqrt{2} \\
\hat{t}_{-1,i}^\dagger \left|0\right\rangle &= \left|t_{-1}\right\rangle_i = \left|\downarrow_1, \downarrow_2\right\rangle_i .
\end{aligned}
\tag{4.20}
$$

The index i here is the dimer index, where each dimer has two spins in layers 1 and 2. The total basis is then expressed by the vector

$$
\tilde{\mathbf{t}}_k = \left(\hat{t}_{A_{1,k}}, \hat{t}_{B_{1,k}}, \hat{t}_{C_{1,k}}, \hat{t}_{A_{0,k}}, \hat{t}_{B_{0,k}}, \hat{t}_{C_{0,k}}, \hat{t}_{A_{-1,k}}, \hat{t}_{B_{-1,k}}, \hat{t}_{C_{-1,k}}\right) \tag{4.21}
$$

The task is now to represent spin-operators in this basis too. This will allow us to fully develop the bond-wave theory. First we express the operators

$$
\begin{aligned}
\hat{S}_{i,1}^{+} &= \frac{1}{\sqrt{2}}\left[\hat{t}_{1,i}^\dagger(\hat{t}_{0,i} - \hat{s}_i) + (\hat{t}_{0,i}^\dagger + \hat{s}_i^\dagger)\hat{t}_{-1,i}\right] \\
\hat{S}_{i,1}^{-} &= \frac{1}{\sqrt{2}}\left[(\hat{t}_{0,i}^\dagger - \hat{s}_i^\dagger)\hat{t}_{1,i} + \hat{t}_{-1,i}(\hat{t}_{0,i} + \hat{s}_i)\hat{t}_{-1,i}\right] \\
\hat{S}_{i,1}^{z} &= \frac{1}{2}\left[\hat{t}_{1,i}^\dagger\hat{t}_{i,i} + \hat{t}_{0,i}^\dagger\hat{s}_i + \hat{s}_i^\dagger\hat{t}_{0,i} - \hat{t}_{-1,i}^\dagger\hat{t}_{-1,i}\right] \\
\hat{S}_{i,2}^{+} &= \frac{1}{\sqrt{2}}\left[\hat{t}_{1,i}^\dagger(\hat{t}_{0,i} + \hat{s}_i) + (\hat{t}_{0,i}^\dagger - \hat{s}_i^\dagger)\hat{t}_{-1,i}\right] \\
\hat{S}_{i,2}^{-} &= \frac{1}{\sqrt{2}}\left[(\hat{t}_{0,i}^\dagger + \hat{s}_i^\dagger)\hat{t}_{1,i} + \hat{t}_{-1,i}(\hat{t}_{0,i} - \hat{s}_i)\hat{t}_{-1,i}\right] \\
\hat{S}_{i,2}^{z} &= \frac{1}{2}\left[\hat{t}_{1,i}^\dagger\hat{t}_{i,i} - \hat{t}_{0,i}^\dagger\hat{s}_i - \hat{s}_i^\dagger\hat{t}_{0,i} - \hat{t}_{-1,i}^\dagger\hat{t}_{-1,i}\right].
\end{aligned}
\tag{4.22}
$$

This results in a bond-wave BdG Hamiltonian

$$
\hat{H} = \sum_k \begin{bmatrix} \tilde{\mathbf{t}}_k^\dagger \\ \tilde{\mathbf{t}}_{-k} \end{bmatrix} \begin{bmatrix} \tilde{\boldsymbol{M}}_k & \tilde{\boldsymbol{N}}_k \\ \tilde{\boldsymbol{N}}_{-k}^\dagger & \tilde{\boldsymbol{M}}_{-k}^\dagger \end{bmatrix} \begin{bmatrix} \tilde{\mathbf{t}}_k \\ \tilde{\mathbf{t}}_{-k}^\dagger \end{bmatrix} . \tag{4.23}
$$

We note that the above form of the Hamiltonian in general contains terms such as $\hat{t}_{\pm 1,k}^\dagger \hat{t}_{0,k}$. However, if we take into account the horizontal plane of reflection σ_h, then these terms must disappear. The reason is that although σ_h has no effect on $\langle \hat{S}^z \rangle$, it still permutes the spin-1/2 of the top and bottom layer, which introduces a sign. In other words $\sigma_h : \left|\uparrow, \downarrow\right\rangle \to -\left|\downarrow, \uparrow\right\rangle$ so that $\sigma_h : \hat{t}_{0,k} \to -\hat{t}_{0,k}$. The result of this is that the a separate hopping Hamiltonian may be written for the $m = \pm 1$ triplons and the $m = 0$. We write these as

$$
\hat{H}^{(1.-1)} = \sum_k \begin{bmatrix} \mathbf{t}_k^\dagger \\ \mathbf{t}_{-k} \end{bmatrix} \begin{bmatrix} \boldsymbol{M}_k & \boldsymbol{N}_k \\ \boldsymbol{N}_k^\dagger & \boldsymbol{M}_k^\dagger \end{bmatrix} \begin{bmatrix} \mathbf{t}_k \\ \mathbf{t}_{-k}^\dagger \end{bmatrix} \tag{4.24}
$$

and

$$\hat{H}^{(0)} = \sum_k \begin{bmatrix} \mathbf{t}^\dagger_{0,k} \\ \mathbf{t}_{0,-k} \end{bmatrix} \begin{bmatrix} \boldsymbol{M}_{0,k} & \boldsymbol{N}_{0,k} \\ \boldsymbol{N}^\dagger_{0,k} & \boldsymbol{M}^\dagger_{0,k} \end{bmatrix} \begin{bmatrix} \mathbf{t}_{0,k} \\ \mathbf{t}^\dagger_{0,-k} \end{bmatrix}. \tag{4.25}$$

Here

$$\begin{aligned} \mathbf{t}^\dagger_k &= \left(\mathbf{t}^\dagger_{1,k}, \mathbf{t}^\dagger_{-1,k}\right) \\ \mathbf{t}_{-k} &= \left(\mathbf{t}_{-1,-k}, \mathbf{t}_{1,-k}\right) \end{aligned} \tag{4.26}$$

with

$$\mathbf{t}_{m,k} = \left(\hat{t}_{A_{m,k}}, \hat{t}_{B_{m,k}}, \hat{t}_{C_{m,k}}\right). \tag{4.27}$$

For convenience in discussing our results we also define the total z-component of spin

$$\hat{S}^z_T = \mathbf{t}^\dagger_{1,k}\mathbf{t}_{1,k} - \mathbf{t}^\dagger_{-1,k}\mathbf{t}_{-1,k}. \tag{4.28}$$

Interestingly the terms which are zeroed out by this procedure are the *in-plane* DM and *out-of-plane* nematic components of the Hamiltonian. This is a consequence of the fact that we have expressed the problem in the triplet basis defined by H_{XXZ} and treat these other components perturbatively. In general any $\hat{S}^z_i\hat{S}^y_j$ and $\hat{S}^z_i\hat{S}^x_j$ components will due to reflection symmetry cancel in the triplon basis, and these are the terms one obtains through $\hat{H}_{DM,\parallel}$ and $\hat{H}_{DM,\perp}$.

The $\boldsymbol{M}_k$ blocks are 6×6 matrices, which couple the $m = \pm 1$ subspaces. Because the $|t\rangle_0$ subspace is decoupled due to the mirror symmetry, it defines a spinless 3-sublattice bosonic hopping Hamiltonian with the 3×3 block $\boldsymbol{M}_{0,k}$. Both the spinfull and spinless blocks have associated pairing terms which are captured by the corresponding N-blocks.

In the following we express these blocks in terms of the 3×3 identity matrix and the Gell-Mann matrices

$$\begin{gathered} \lambda_1 = \begin{bmatrix} 0 & 1 & 0 \\ 1 & 0 & 0 \\ 0 & 0 & 0 \end{bmatrix}, \quad \lambda_2 = \begin{bmatrix} 0 & -i & 0 \\ i & 0 & 0 \\ 0 & 0 & 0 \end{bmatrix}, \quad \lambda_3 = \begin{bmatrix} 1 & 0 & 0 \\ 0 & -1 & 0 \\ 0 & 0 & 0 \end{bmatrix} \\ \lambda_4 = \begin{bmatrix} 0 & 0 & 1 \\ 0 & 0 & 0 \\ 1 & 0 & 0 \end{bmatrix}, \quad \lambda_5 = \begin{bmatrix} 0 & 0 & i \\ 0 & 0 & 0 \\ -i & 0 & 0 \end{bmatrix}, \quad \lambda_6 = \begin{bmatrix} 0 & 0 & 0 \\ 0 & 0 & 1 \\ 0 & 1 & 0 \end{bmatrix} \\ \lambda_7 = \begin{bmatrix} 0 & 0 & 0 \\ 0 & 0 & -i \\ 0 & i & 0 \end{bmatrix}, \quad \lambda_8 = \begin{bmatrix} 1 & 0 & 0 \\ 0 & 1 & 0 \\ 0 & 0 & -2 \end{bmatrix}. \end{gathered} \tag{4.29}$$

The spinless block of the Hamiltonian is derived from Heisenberg exchange terms, but does not contain contributions from the DM or nematic interaction.

$$\boldsymbol{M}_{0,k} = \boldsymbol{M}^{XXZ}_{0,k} = J_\parallel \boldsymbol{I}_{3\times 3} + J'_\perp \left[\cos(\delta_1 \cdot k/2)\lambda_4 + \cos(\delta_2 \cdot k/2)\lambda_1 + \cos(\delta_3 \cdot k/2)\lambda_6\right]. \tag{4.30}$$

The pairing block has identical off-diagonal terms, but its diagonal is zero

$$\boldsymbol{N}_{0,k} = \boldsymbol{M}_{0,k} - J_{\parallel}\boldsymbol{I}_{3\times 3}. \tag{4.31}$$

The spinfull block on the other hand contains contributions from both the nematic and DM terms.

$$\boldsymbol{M}_k = \boldsymbol{M}_k^{XXZ} + \boldsymbol{M}_k^{\mathrm{DM}} + \boldsymbol{M}_k^{\mathrm{nematic}}. \tag{4.32}$$

This block operates on the space defined by the $\hat{t}_{\pm 1,k}$ triplons and therefore in general will have terms which can be decomposed as $s^{\alpha} \otimes \lambda_{\beta}$, where s^{α} are the spin matrices projected onto the $m = \pm 1$ subspace. On the spinor space spanned by the $m = \pm 1$ triplons each s^{α} corresponds to the Pauli-matrix σ^{α}. The s^x and s^y matrices may therefore in general mix the $m = \pm 1$ triplets.

The $\boldsymbol{M}_k^{XXZ}$ block comes from Heisenberg exchange terms which commute with the dimer $\hat{S}^z$. It can be written as

$$\begin{aligned}\boldsymbol{M}_k^{XXZ} = {} & \frac{J_{\parallel} + J_{\perp}}{2}\boldsymbol{I}_{2\times 2} \otimes \boldsymbol{I}_{3\times 3} + J'_{\parallel}\big(\cos(\delta_1 \cdot k/2)\boldsymbol{I}_{2\times 2} \otimes \lambda_4 \\ & + \cos(\delta_2 \cdot k/2)\boldsymbol{I}_{2\times 2} \otimes \lambda_1 + \cos(\delta_3 \cdot k/2)\boldsymbol{I}_{2\times 2} \otimes \lambda_6\big)\end{aligned} \tag{4.33}$$

The coupling terms may then be written as

$$\boldsymbol{N}_k^{XXZ} = -\boldsymbol{M}_k^{XXZ} + \frac{J_{\parallel} + J_{\perp}}{2}. \tag{4.34}$$

As discussed earlier, the in-plane component of the DM interaction vanishes for the triplon hopping Hamiltonian due to the mirror plane. The out-of-plane component is

$$\begin{aligned}\boldsymbol{M}_k^{\mathrm{DM}} = {} & \big(D'_{\perp}\cos(\delta_1 \cdot k/2) + D''_{\perp}\cos((\delta_2 - \delta_3) \cdot k/2)\big)s^z \otimes \lambda_5 \\ & + \big(D'_{\perp}\cos(\delta_2 \cdot k/2) + D''_{\perp}\cos((\delta_3 - \delta_1) \cdot k/2)\big)s^z \otimes \lambda_2 \\ & + \big(D'_{\perp}\cos(\delta_3 \cdot k/2) + D''_{\perp}\cos((\delta_1 - \delta_2) \cdot k/2)\big)s^z \otimes \lambda_7.\end{aligned} \tag{4.35}$$

We also have pairing terms

$$\boldsymbol{N}_k^{\mathrm{DM}} = -\boldsymbol{M}_k^{\mathrm{DM}} \tag{4.36}$$

This term is analogous to the spin-orbit coupling of the Kane and Mele model and here it has exactly the same function. As long as the two spinful triplet bands do not mix, the $m = 1$ triplet bands experience an imaginary hopping which is opposite, but with equal magnitude on the $m = -1$ bands. Therefore the bands will in this situation have equal and opposite Chern numbers and the thermal Hall signal from each band adds up to zero. Now, because they have opposite spin, they should support a spin-Nernst signal. This may also be compared to the bilayer kagome magnet with weak interlayer anti-ferromagnet interaction. Here the same term manifests as a conventional DM-interaction for magnons with opposite sign on the two-layers.

However, in the presence of nematic interactions this is no longer the case. In general the nematic interaction may break the global $m = \pm 1$ degeneracy and cause the bands to mix. For the nematic interaction, it is only the in-plane components which contribute. They have the form

$$\begin{aligned}\boldsymbol{M}_k^{\text{Nematic}} &= \frac{K_{\|}}{4}\left(s^x \otimes \lambda_8 - \sqrt{3}s^y \otimes \lambda_3\right) \\ &\quad + K_{\|}' \cos(\delta_1 \cdot k/2)\Big(-s^x/2 + \sqrt{3}s^y/2\Big) \otimes \lambda_4 \\ &\quad + K_{\|}' \cos(\delta_2 \cdot k/2)\Big(-s^x/2 - \sqrt{3}s^y/2\Big) \otimes \lambda_1 \\ &\quad + K_{\|}' \cos(\delta_3 \cdot k/2) s^x \otimes \lambda_6. \end{aligned} \tag{4.37}$$

The corresponding pairing terms are obtained by removing the diagonal component of this matrix. The off-diagonal elements are opposite in sign

$$\boldsymbol{N}_k^{\text{Nematic}} = -\boldsymbol{M}_k^{\text{Nematic}} + \frac{K_{\|}}{4}\left(s^x \otimes \lambda_8 - \sqrt{3}s^y \otimes \lambda_3\right). \tag{4.38}$$

Due to the appearance of s^x and s^y, these terms do not commute with $\hat{S}_T^z$ (see equation (4.28)) and therefore mix the spinful subspace. In the Kane and Mele model such terms were allowed in the form of the Rashba spin-orbit coupling. However, a key difference between these terms and the ones allowed in our triplon hopping model is that our $m = \pm 1$ bands are not protected from hybridizing at the TRIM. This can be readily seen by the fact that $\boldsymbol{M}_k^{\text{Nematic}}$ (equation (4.37)) has a constant non-zero diagonal. Therefore the $\mathcal{Z}_2$topology of our model is not protected by time-reversal symmetry, but only appears when the $K_{\|}$ and $K_{\|}'$ are both accidentally zero.

To see why time-reversal symmetry does not protect against the mixing of bands at the TRIM consider the effect of time-reversal on the dimer. For an arbitrary $S = 1/2$ dimer we write

$$\begin{aligned}\tau &: \left|\uparrow,\uparrow\right\rangle \to \left|\downarrow,\downarrow\right\rangle \\ \tau &: \left|\uparrow,\downarrow\right\rangle \to -\left|\downarrow,\uparrow\right\rangle \\ \tau &: \left|\downarrow,\uparrow\right\rangle \to -\left|\uparrow,\downarrow\right\rangle \\ \tau &: \left|\downarrow,\downarrow\right\rangle \to \left|\uparrow,\uparrow\right\rangle . \end{aligned} \tag{4.39}$$

Here the sign of the $|\sigma, \bar{\sigma}\rangle$ is reversed because of how the electrons are swapped. For the $|\sigma, \sigma\rangle$ this reversal happens either twice or not at all, depending on how the electron gauge has been fixed, and so results in no change. Time-reversal therefore has no effect on the singlet state. Its matrix form on the space of triplons $[|t_1\rangle, |t_0\rangle, |t_{-1}\rangle]$ is

$$\boldsymbol{T} = \begin{bmatrix} 0 & 0 & 1 \\ 0 & -1 & 0 \\ 1 & 0 & 0 \end{bmatrix} K. \tag{4.40}$$

This matrix squares to the identity and therefore does not give a Krämers degeneracy. Writing this operator in terms of its action on the spinful $m = \pm 1$ subspace, where it acts as s^x. We also include the sublattice degrees of freedom through the identity operator as

$$\boldsymbol{T} = s^x \otimes \boldsymbol{I}_{3\times 3} K. \tag{4.41}$$

This commutes with $\boldsymbol{M}^{\text{Nematic}}$. Evidently, time-reversal is therefore not enough to protect triplon bands from hybridizing.

In this section we have so far made several points that are worth summarizing before moving on to results.

1. Nearest and next-nearest neighbor terms were included in this model in the most general form allowed by the D_{6h} point group. Due to the horizontal mirror plane, there are no matrix elements which mix the $m = 0$ triplon with the $m = \pm 1$ subspace. Because of the horizontal mirror symmetry the in-plane component of the DM interaction does not affect the triplons to linear order in the bond-wave theory. Neither does the out-of-plane component of the nematic interaction.

2. The allowed component of the DM interaction corresponds to the spin-orbit coupling in the Kane and Mele model, which gives us a way to realize the $\mathcal{Z}_2$ topology. In our case the spinful bands $m = \pm 1$ are subject to an equal and opposite complex hopping respectively. If the dimer $\hat{S}^z$ commutes with the Hamiltonian, then the situation is analogous to the Kane and Mele model where we can view each spin component as defining a Haldane model with an opposite complex hopping.

3. The nematic term mixes the $m = \pm 1$ bands. It does so even at the TRIM as there is no Krämer's protection of the triplons. This is in contrast to the Rashba spin-orbit term in the Kane and Mele model, which does not break the $\mathcal{Z}_2$ topology of the model.

The $\mathcal{Z}_2$ phase of the triplon bands is not protected by a Krämer's degeneracy in the same way as the electron bands would be. As suggested by [13], it seems that a *pseudo* time-reversal symmetry is needed. We will discuss what form this must take and how it needs to be realized in bosonic systems later in the chapter. We will also discuss the nematic term and its effect on the topological triplon edge-mode by calculating the triplon spectrum in an open geometry.

Before discussing this aspect of the problem in detail we will first consider what happens when we restrict interactions such that the Hamiltonian only contains $U(1)$ symmetric terms. This is achieved by setting $K_{\parallel} = K'_{\parallel} = 0$. We also include a Zeeman term

$$\hat{H}_{\text{Zeeman}} = -h_z \sum_{\substack{i \\ l=1,2}} \hat{S}^z_i. \tag{4.42}$$

In the triplon BdG Hamiltonian this enters $\boldsymbol{M}_{\sigma,k}$ as

$$\boldsymbol{M}_k^{\text{Zeeman}} = -h_z s^z \otimes \boldsymbol{I}_{3\times 3}. \tag{4.43}$$

With this we will be able to study a Chern insulating TR breaking limit of the model too.

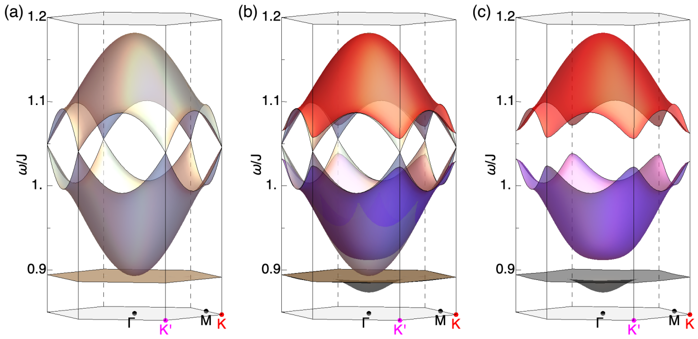

Figure 4.2: Here the bulk bands are depicted for $K_{\parallel} = 0$, $h = 0$, $J = 1$ and $J' = 0.2$. (a) When the DM interaction is zero all of the bands coincide and there is a global three-fold degeneracy as the model has $SU(2)$ symmetry. (b) The band-structure is depicted for $D'' = 0.01$. The $m = \pm 1$ bands are globally degenerate and almost coincide with the $m = 0$ if not for the DM-induced band-gaps. (c) The $m = \pm 1$ bands are depicted with $m = 0$ omitted.

4.3 Berry curvature and band-topology

In this section we restrict our attention to the case where $K_{\parallel} = 0$. In this case triplons characterized by distinct m do not mix because the dimer $\hat{S}^z$ is conserved. We can therefore decompose the Hamiltonian into three separate blocks. Each block is a 3×3 matrix acting on the sub-lattice space of the problem. As explained in the previous section, the DM interaction contributes terms such as $s^z \otimes \lambda_\alpha$, λ_α being a Gell-Mann matrix. In each of the m blocks, this is simply replaced by $m\lambda_\alpha$. Apart from this, the Heisenberg interaction contributes through the $\hat{H}^{XXZ}$ part. If we set $J_{\perp} = J_{\parallel} = J$, the Heisenberg interaction is invariant to a global $SU(2)$ rotation of the spins. We can express this independently of m. Thus we obtain

$$\boldsymbol{M}^{U(1)}_{m,k} = \boldsymbol{M}^{SU(2)}_{k} + \boldsymbol{M}^{\mathrm{DM}}_{m,k}, \tag{4.44}$$

with

$$\boldsymbol{M}^{SU(2)}_{k} = J\boldsymbol{I}_{3\times 3} + J'\big(\cos(\delta_1 \cdot k/2)\lambda_4 + \cos(\delta_2 \cdot k/2)\lambda_1 + \cos(\delta_3 \cdot k/2)\lambda_6\big) \tag{4.45}$$

and

$$\begin{aligned}\boldsymbol{M}^{\mathrm{DM}}_{m,k} = m\big(&D'_{\perp}\cos(\delta_1 \cdot k/2) + D''_{\perp}\cos((\delta_2 - \delta_3)\cdot k/2)\big)\lambda_5 \\ &+ \big(D'_{\perp}\cos(\delta_2 \cdot k/2) + D''_{\perp}\cos((\delta_3 - \delta_1)\cdot k/2)\big)\lambda_2 \\ &+ \big(D'_{\perp}\cos(\delta_3 \cdot k/2) + D''_{\perp}\cos((\delta_1 - \delta_2)\cdot k/2)\big)\lambda_7.\end{aligned} \tag{4.46}$$

We also have the pairing terms given by

$$\boldsymbol{N}^{U(1)}_{m,k} = J\boldsymbol{I}_{3\times 3} - \boldsymbol{M}^{U(1)}_{m,k}. \tag{4.47}$$

The band-dispersion is plotted in figure 4.2. The energy scale is given by $J = 1$, which defines the gap to excitations above the singlet state. $J' = 0.2$ is what gives the bands dispersion. The dispersion is calculated for the $SU(2)$ symmetric case where all three components of m are equivalent. When $D'' = 0.01$ is included the $m = \pm 1$ bands additionally obtain gaps at the high-symmetry points. We calculate the band-gaps for the BdG Hamiltonian as outlined in Chapter 2 and obtain the analytical form of the band-energies at the Γ-point

$$\begin{aligned} \omega_{1,m}(\Gamma) &= \sqrt{J(J - 2J' - m\Delta_\Gamma)} \\ \omega_{2,m}(\Gamma) &= \sqrt{J(J - 2J' + m\Delta_\Gamma)} \\ \omega_{3,m}(\Gamma) &= \sqrt{J(J + 4J')}, \end{aligned} \tag{4.48}$$

with

$$\Delta_\Gamma = 2\sqrt{3}(D' + D''). \tag{4.49}$$

At the K and K' points they are

$$\begin{aligned} \omega_{1,m}(K) &= \sqrt{J(J - 2J')} \\ \omega_{2,m}(K) &= \sqrt{J(J + J' - m\Delta_K)} \\ \omega_{3,m}(K) &= \sqrt{J(J + J' + m\Delta_K)}. \end{aligned} \tag{4.50}$$

with

$$\Delta_K = \sqrt{3}(D' - 2D''). \tag{4.51}$$

The gaps at the Γ (K) points close when $\Delta_{\Gamma(K)}$ are 0. This occurs at $D' = -D''$ and $D' = 2D''$ respectively.

The Bogoliubov transform results in wavefunctions, $|\psi_i\rangle$ whose Berry's curvature must be calculated in the following way.

$$F_i^{x,y} = \langle \partial_{k_x}\psi_i | \Sigma_z \partial_{k_y}\psi_i \rangle - \langle \partial_{k_y}\psi_i | \Sigma_z \partial_{k_x}\psi_i \rangle \tag{4.52}$$

From this the Chern numbers can be calculated by discretizing the Brillouin zone in a way that is analogous to [153]. Doing so we obtain the topological phase-diagram of figure 4.3. The combination of nearest and next-nearest neighbor DM interactions in the form of D' and D'' means that the band-touching phase transitions at the Γ-point and K and K' points can occur separately. Each band-touching defines a phase boundary, the ones at Γ-point being $D' = -D''$ and the K, K' points being $D' = 2D''$. Because of this we see the appearance of four distinct topological phases. In figure 4.4 we show how the Berry's curvature gets redistributed at these band-touching points.

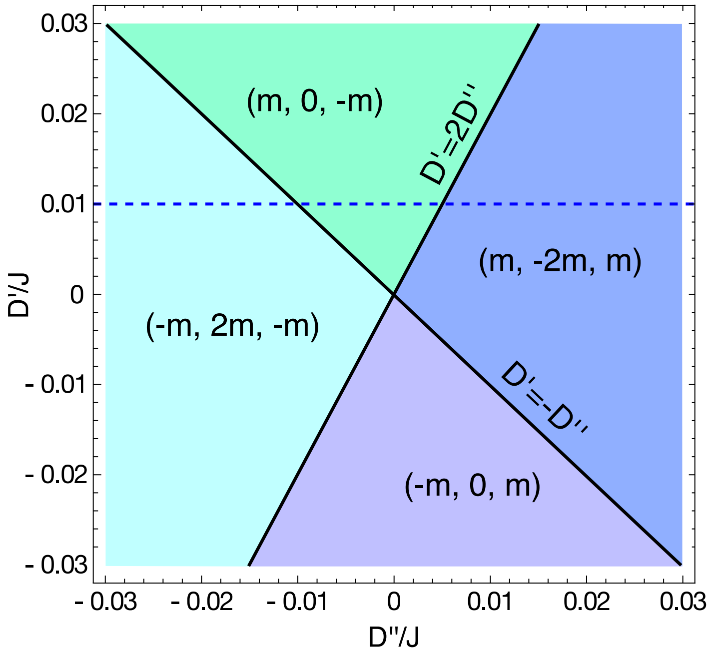

Figure 4.3: In the $U(1)$ symmetric model the Chern numbers can be calculated separately for each m component of the triplon wave-function. Doing so gives this phase diagram with four distinct topological phases defined by regions on (D', D'') space. The Chern numbers are listed for each band in order of increasing energy. The dashed line at constant D' defines a path taken in parameter space in generating figure 4.4.

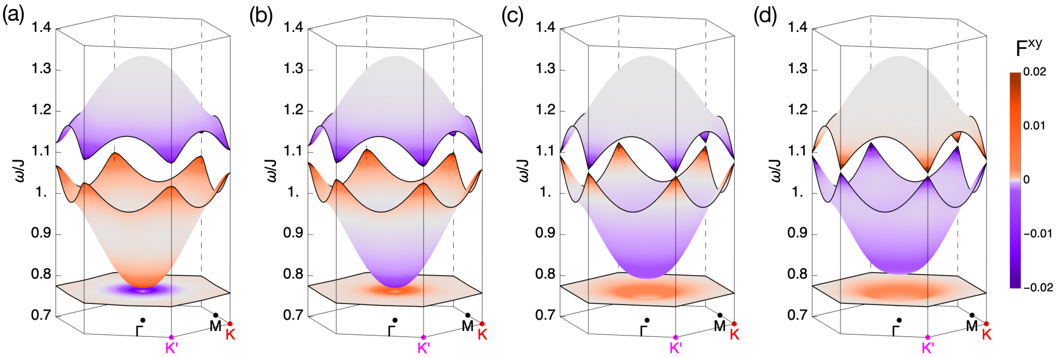

Figure 4.4: The distribution of the Berry's curvature is shown here for the $m = 1$ bands following the dashed path shown on the topological phase diagram of figure 4.3. The parameters are $J = 1$, $J' = 0.2$ and $D' = 0.01$. The next-nearest neighbor DM interaction is (a) $D'' = -0.0125$ (b) $D'' = -0.0075$ (c) $D'' = 0.0025$ (d) $D'' = 0.0075$. The band-touching at the Γ-point occurs at $D'' = -D'$. Here the Berry's curvature is redistributed as seen in going from (a) to (b). The touching at the K and K' points occurs when $D'' = D'/2$ and as seen the distribution of the Berry's curvature here inverts on the two bands that touch.

4.3.1 Linear vs quadratic band-touchings

The band-touchings at the Γ point and at K and K' points can be approximated by effective two-band theories similarly to what was carried out in Chapter 3 for the single layer kagome magnon dispersion. Here the dispersion was quadratic in k near the Γ point and linear at the K and K' points.

For the triplon bands of $\hat{H}^{U(1)}_{m,k}$ the situation is identical as it is a 3-sublattice problem with imaginary hopping. The only difference here being that there is an additional next-nearest neighbor imaginary hopping taken into account here. In this section we will derive analytical expressions for the Berry's curvature near these band-touchings. We will do so by considering effective two-band models at the vicinity of the band-touchings.

In deriving these effective models we will consider only the number conserving part of the Hamiltonian. Although there are some instances where pairing terms can influence the topology of a system, they need be significant enough to make a band-transition happen by closing one or more gaps. However, without the pairing terms the triplon energies at the Γ-point are

$$\begin{aligned} \omega_{1,m}(\Gamma) &= J - J' - m\Delta_\Gamma/2 \\ \omega_{2,m}(\Gamma) &= J - J' + m\Delta_\Gamma/2 \\ \omega_{3,m}(\Gamma) &= J + 2J'. \end{aligned} \tag{4.53}$$

While at the K and K' points they are

$$\begin{aligned} \omega_{1,m}(K) &= J - J' \\ \omega_{2,m}(K) &= J + J'/2 + m\Delta_K/2 \\ \omega_{3,m}(K) &= J + J'/2 - m\Delta_K/2. \end{aligned} \tag{4.54}$$

The band-touching point therefore does not change compared to the full BdG Hamiltonian. It is still given by $\Delta_{\Gamma(K)} = 0$.

The effective field model will take the form

$$\boldsymbol{M}^{\text{eff}}_k = d_0(k)\boldsymbol{I}_{2\times 2} + \mathbf{d}(k)\cdot\boldsymbol{\sigma}. \tag{4.55}$$

Here $\boldsymbol{\sigma}$ is the vector of Pauli-matrices. The above expression has an associated Berry's curvature given by

$$\Omega_{k_x,k_y} = \frac{1}{2}\frac{\mathbf{d}\cdot\left(\frac{\partial\mathbf{d}}{\partial k_x}\times\frac{\partial\mathbf{d}}{\partial k_y}\right)}{(\mathbf{d}\cdot\mathbf{d})^{3/2}}. \tag{4.56}$$

This is the Berry's curvature of the lower of the two touching bands. The other band is endowed with a curvature of $-\Omega_{K,K'}$. We will project the three-sublattice problem of each m onto the space defined by the bands which diagonalize the Hamiltonian at a band-gap.

Linear band-touching at K and K'

At the K point we may diagonalize the matrix $\boldsymbol{M}_{m,k}^{U(1)}$ with

$$U_K = \begin{bmatrix} -\frac{1}{\sqrt{3}} & -\frac{1}{\sqrt{2}} & \frac{1}{\sqrt{6}} \\ -\frac{1}{\sqrt{3}} & \frac{1}{\sqrt{2}} & \frac{1}{\sqrt{6}} \\ \frac{1}{\sqrt{3}} & 0 & \frac{2}{\sqrt{6}} \end{bmatrix}. \tag{4.57}$$

The first column vector here corresponds to the low-energy eigenstate of $\boldsymbol{M}_{m,k}^{U(1)}$. The second and third vector form a doublet at the K-point in the absence of DM interaction. In this basis $M_{m,k}^{U(1)}$ becomes

$$U_k \boldsymbol{M}_{m,k}^{U(1)} U_k^{\dagger} = \begin{bmatrix} J - J' & -\frac{1}{4}\sqrt{\frac{3}{2}}J'k_y + im\frac{3}{4\sqrt{2}}D'k_x & \frac{1}{4}\sqrt{\frac{3}{2}}J'k_x + im\frac{3}{4\sqrt{2}}D'k_y \\ -\frac{1}{4}\sqrt{\frac{3}{2}}J'k_y - im\frac{3}{4\sqrt{2}}D'k_x & J + \frac{J'}{2} + \frac{\sqrt{3}}{4}J'k_x & -\frac{\sqrt{3}}{4}J'k_y + im\sqrt{3}\left(\frac{D'}{2} - D''\right) \\ \frac{1}{4}\sqrt{\frac{3}{2}}J'k_x - im\frac{3}{4\sqrt{2}}D'k_y & -\frac{\sqrt{3}}{4}J'k_y - im\sqrt{3}\left(\frac{D'}{2} - D''\right) & J + \frac{J'}{2} - \frac{\sqrt{3}}{4}J'k_x \end{bmatrix}. \tag{4.58}$$

As seen above there is some mixing of the high-energy bands with the low energy one at finite k, but to a good approximation we can consider them to be separate. We can here write the effective field model

$$\boldsymbol{M}_K^{\text{lin}} = (J + \frac{J'}{2})\boldsymbol{I}_{2\times 2} + \mathbf{d}_K \cdot \boldsymbol{\sigma}, \tag{4.59}$$

with

$$\begin{aligned} d_K^x &= -\frac{\sqrt{3}}{4}J'k_y \\ d_K^y &= -m\frac{\sqrt{3}}{2}(D' - 2D'') \\ d_K^z &= \frac{\sqrt{3}}{4}J'k_x. \end{aligned} \tag{4.60}$$

At the K'-point the model is written with $(d_{K'}^x, d_{K'}^y, d_{K'}^z) = (-d_K^x, d_K^y, -d_K^z)$. The Berry's curvature is the same at the K, K'. Now equation (4.56) becomes

$$\Omega_{K,K'}(k) = \frac{mJ'^2(D' - 2D'')}{(J'^2k^2 + 4(D' - 2D'')^2)^{3/2}}. \tag{4.61}$$

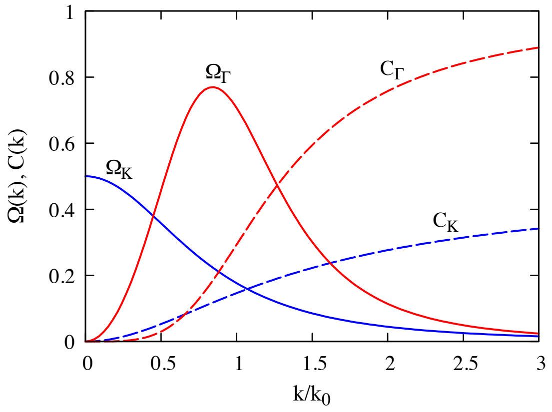

Figure 4.5: The Berry's curvature near Γ and K points. It is here plotted as a function of the radial distance in k-space from the high symmetry point in terms of the characteristic length-scale k_0. The Dashed lines are the contributions to the Chern number obtained by integrating $\Omega_{K,\Gamma}$ from 0 up to k. Note that the Berry's curvature at K only integrates up to $1/2$, but the Berry's curvature is the same at K' and so in total both valleys contribute an integer Chern number.

Here $k^2 = k_x^2 + k_y^2$. We can introduce the characteristic quasi-momentum

$$k_0 = \frac{2(D' - 2D'')}{J'}. \tag{4.62}$$

This now gives a simplified form of the Berry's curvature

$$\Omega_{K,K'}(k) = \frac{mk_0}{2(k^2 + {k_0}^2)^{3/2}}. \tag{4.63}$$

Here we see that $\Omega_{K,K'}$ is highest at $k = 0$. The sign of $\Omega_{K,K'}$ is equal to the sign of mk_0. As with magnons on the kagome lattice, when a circular path in (k_x, k_y)-space is taken around $k = 0$, the $\mathbf{d}_{K,K'}$ vector winds once.

Taking the integral of the Berry's curvature in a disk of radius k, we get a contribution to the Chern number as

$$C_{K,K'} = \frac{1}{2\pi}\int_0^k \Omega_{K,K'}(k')2\pi k' dk' \tag{4.64}$$

$$= \frac{m}{2}\mathrm{sgn}(k_0)\left(1 - \frac{|k_0|}{\sqrt{k^2 + {k_0}^2}}\right). \tag{4.65}$$

Here it is seen clearly that each valley contributes the same $m\ \mathrm{sgn}(k_0)/2$ to the total Chern number. Crossing the $D' = 2D''$ phase boundary reverses the sign of k_0, and therefore changes the sign of the Chern number.

The Berry's curvature and its integral is plotted in figure 4.5. This discussion so far has been concerned only with contributions to the Chern number from the K and

K' points and is only valid near those high-symmetry points. However, each band also has a contribution from the Berry's curvature at the Γ point, which we explore below.

4.3.2 Quadratic band-touching at Γ

In the previous discussion we expanded the Hamiltonian up to first order in k in the vicinity of the K, K' points. In order to understand the appearance of Chern numbers due to a winding of the effective field vector $\mathbf{d}_{K,K'}$, the leading first order terms were enough.

However, the matrix $\boldsymbol{M}^{U(1)}_{m,k}$ only has terms which are either cosinusoidal or constant in k. Therefore, at the Γ point, any Taylor expansion performed will only contain constant and second order terms. Clearly a constant $\mathbf{d}$ will not result in Chern numbers, so it is here necessary to expand up to second order.

First we consider again a change of basis. Here we use

$$U_\Gamma = \begin{bmatrix} \frac{1}{\sqrt{3}} & \frac{1}{\sqrt{2}} & \frac{1}{\sqrt{6}} \\ \frac{1}{\sqrt{3}} & -\frac{1}{\sqrt{2}} & \frac{1}{\sqrt{6}} \\ \frac{1}{\sqrt{3}} & 0 & -\frac{2}{\sqrt{6}} \end{bmatrix}. \tag{4.66}$$

Changing to this basis and expanding up to second order in k we obtain

$$U_\Gamma \boldsymbol{M}^{U(1)}_{m,k} U_\Gamma^\dagger = \begin{bmatrix} J - \frac{J'}{8}k^2 + 2J' & -\frac{J'}{8\sqrt{2}}k_x k_y & -\frac{J'}{16\sqrt{2}}(k_x^2 - k_y^2) \\ -\frac{J'}{8\sqrt{2}}k_x k_y & J - J' + \frac{J'}{8}k_x^2 & -im\sqrt{3}(D' + D'') + \frac{J'}{8}k_x k_y \\ -\frac{J'}{16\sqrt{2}}(k_x^2 - k_y^2) & im\sqrt{3}(D' + D'') + \frac{J'}{8}k_x k_y & J - J' + \frac{J'}{8}k_y^2 \end{bmatrix}. \tag{4.67}$$

There are additional terms of the form k^2D' and k^2D'', however, these are vanishingly small compared to the constant D' and D'' terms. We take the bottom right block of the above matrix to be our effective field model

$$\boldsymbol{M}^{\mathrm{quad}}_\Gamma = \left(J - J'\left(1 - \frac{k^2}{16}\right)\right)\boldsymbol{I}_{2\times2} + \mathbf{d}_\Gamma \cdot \boldsymbol{\sigma}, \tag{4.68}$$

with

$$\begin{aligned} d^x_\Gamma &= \frac{1}{8}J'k_x k_y \\ d^y_\Gamma &= m\sqrt{3}(D' + D'') \\ d^z_\Gamma &= \frac{1}{16}J'({k_x}^2 - {k_y}^2). \end{aligned} \tag{4.69}$$

Again, drawing a circular path around $k = 0$ the (d^x, d^z) components $\mathbf{d}_\Gamma$ have a non-zero winding number. However, here this feature winds twice and not once.

We again calculate the Berry's curvature of the lower band using equation (4.56). We obtain

$$\Omega_\Gamma(k) = \frac{4m\sqrt{3}(D' + D'')\left(\frac{J'k}{8}\right)^2}{\left[12(D' + D'')^2 + \left(\frac{J'k^2}{8}\right)^2\right]^{3/2}}. \tag{4.70}$$

We now define the reciprocal lattice length scale

$${k_0}^2 = 16\sqrt{3}\frac{|D' + D''|}{J'}. \tag{4.71}$$

This allows us to rewrite

$$\Omega_\Gamma = m\frac{2k^2{k_0}^2}{(k^4 + {k_0}^4)^{3/2}}\mathrm{sgn}(D' + D''). \tag{4.72}$$

In contrast to the Berry's curvature of the linearly dispersing model the maximum is now at $k = 2^{-1/4}k_0$ and it vanishes at $k = 0$ as well as $k \gg k_0$. We have the asymptotic forms

$$\Omega_\Gamma = \begin{cases} m\ \mathrm{sgn}(D' + D'')\frac{2k^2}{{k_0}^4} + \ldots & k \to 0 \\ m\ \mathrm{sgn}(D' + D'')\frac{2{k_0}^2}{k^4} + \ldots & k \gg k_0 \end{cases}. \tag{4.73}$$

The Berry's curvature forms a ring around the origin which contrasts with the linearly dispersing model at K, K'. Performing the integral over the disk with radius k this time yields

$$C_\Gamma(k) = m\ \mathrm{sgn}(D' + D'')\left(1 - \frac{{k_0}^2}{\sqrt{k^4 + {k_0}^4}}\right) \tag{4.74}$$

$$= m\ \mathrm{sgn}(D' + D'')\left(1 - \frac{{k_0}^2}{k^2}\right), \quad k \gg k_0 \tag{4.75}$$

We thereby have a Berry's curvature which integrates up to $m\ \mathrm{sgn}(D' + D'')$ on the lower band (the Berry's curvature on the upper band is reversed in sign.) Now one may simply add up the contributions from the Γ point and the K, K' points to determine completely the Chern numbers on each band. At the Γ point is the two lower bands which touch, and therefore here the contribution to the total Chern number depends on $\mathrm{sgn}(D' + D'')$. This completely determines the Chern number on the lowest band, but the middle band will have an additional contribution from the K, K' point which depends on $\mathrm{sgn}(D' - 2D'')$. Thus it may be either 0 or $\pm m$. Finally the Chern number of the top band only depends on the band-touching at K, K'. Thus we see how the phase diagram of figure 4.3 is reproduced.

4.4 $\mathcal{Z}_2$-topology and pseudo-time-reversal operator

So far we have established the topology of the triplon bands without nematic terms. We have concluded that we can analyze the bands separately in blocks of distinct m quantum numbers. Here each m subspace acts as a separate hopping Hamiltonian and the DM terms enact an imaginary hopping with opposite chirality for $m = 1$ and -1.

For $m = 0$ the hopping is purely real and the bands are topologically trivial. For $m = \pm 1$ the two triplon bands experience an equal magnitude DM interaction with opposite sign. The result is that the bands will have opposite Berry's curvature and Chern numbers.

This situation is similar to that of the Kane and Mele model [5] in the absence of Rashba spin-orbit coupling. Each band has a time-reversed degenerate partner with opposite Chern number. Taken together this results in a Chern number of 0. The $\mathcal{Z}_2$ topological invariant for such a system is the spin Chern number, i.e. for band i we have

$$(C_{m=1,i} - C_{m=-1,i})/2 \mod 2. \tag{4.76}$$

If this equates to 1 then topological helical edge-modes will appear. In figure 4.6 we show these for different edge-geometries.

However, it is important to establish that the $m = \pm 1$ triplons are not true Krämers pairs since they are bosons. Therefore, although they are connected by time-reversal in the special case of $K_{\|} = 0$, in general time-reversal symmetry does not prevent them from mixing. This is why symmetry allowed terms such as the bond-nematic interaction are able to mix them.

The reason for the Krämers degeneracy to appear in fermionic systems with TR symmetry, is that TR squares to -1 [154]. When acting on bosons, this is not the case, which is why it was suggested by [13] that a different symmetry has to be present to protect the bands from mixing. This is the pseudo-time-reversal (PTR), which acts on the space of bond-operators $(\mathbf{t}_k^\dagger, \mathbf{t}_{-k})$ and can be expressed as

$$\Theta = \boldsymbol{I}_{2\times 2} \otimes i\sigma_y \otimes \boldsymbol{I}_{3\times 3} K. \tag{4.77}$$

The $\boldsymbol{I}_{2\times 2}$ matrix acts on the particle-hole space and $i\sigma_y$ acts on the $m = \pm 1$ subspace and K is complex conjugation. Physically this corresponds to a combination of TR, which on this space is

$$\tau = \boldsymbol{I}_{2\times 2} \otimes \sigma_x \otimes \boldsymbol{I}_{3\times 3} K, \tag{4.78}$$

as well as a $U(1)$ rotation by π which induces an opposite phase on the $m = \pm 1$ bands. This is represented by

$$R = \boldsymbol{I}_{2\times 2} \otimes \sigma_z \otimes \boldsymbol{I}_{3\times 3}. \tag{4.79}$$

Evidently the PTR operator can be written in terms of R and τ as

$$\Theta = R\tau. \tag{4.80}$$

In the Kane and Mele model, the Rashba spin-orbit coupling commutes with TR.

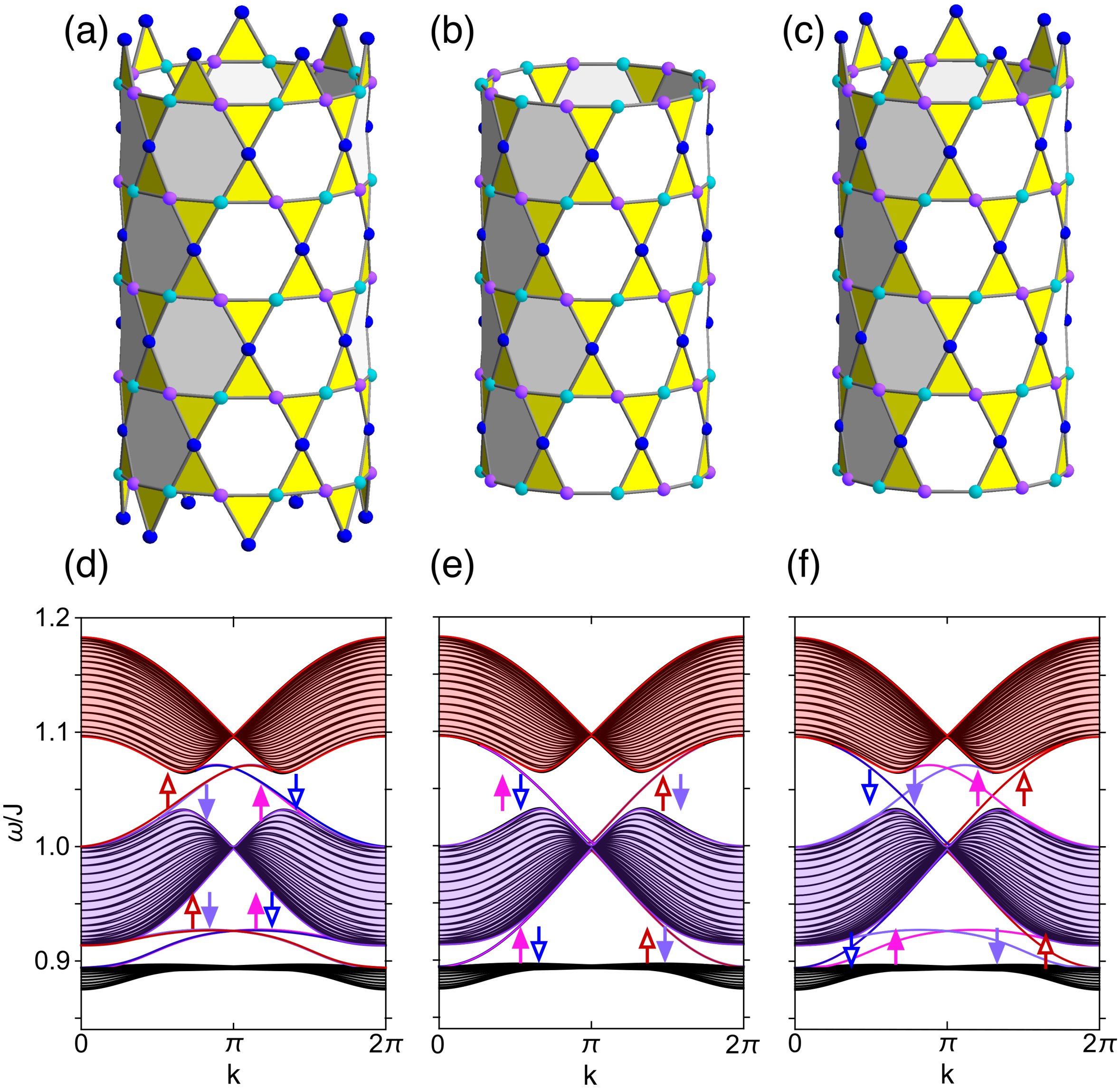

Figure 4.6: Triplon band structure in the absence of nematic interaction, calculated for the open cluster geometries shown in (a-c). Here the appearance of topological quantum edge-modes is evident in all three cases as seen by the band-dispersion (d-e). Each pair of open or filled arrows of opposite orientation are a time-reversed pair of triplon edge-modes. Each edge has a pair of topological modes with opposite spin and momentum k due to time-reversal symmetry.

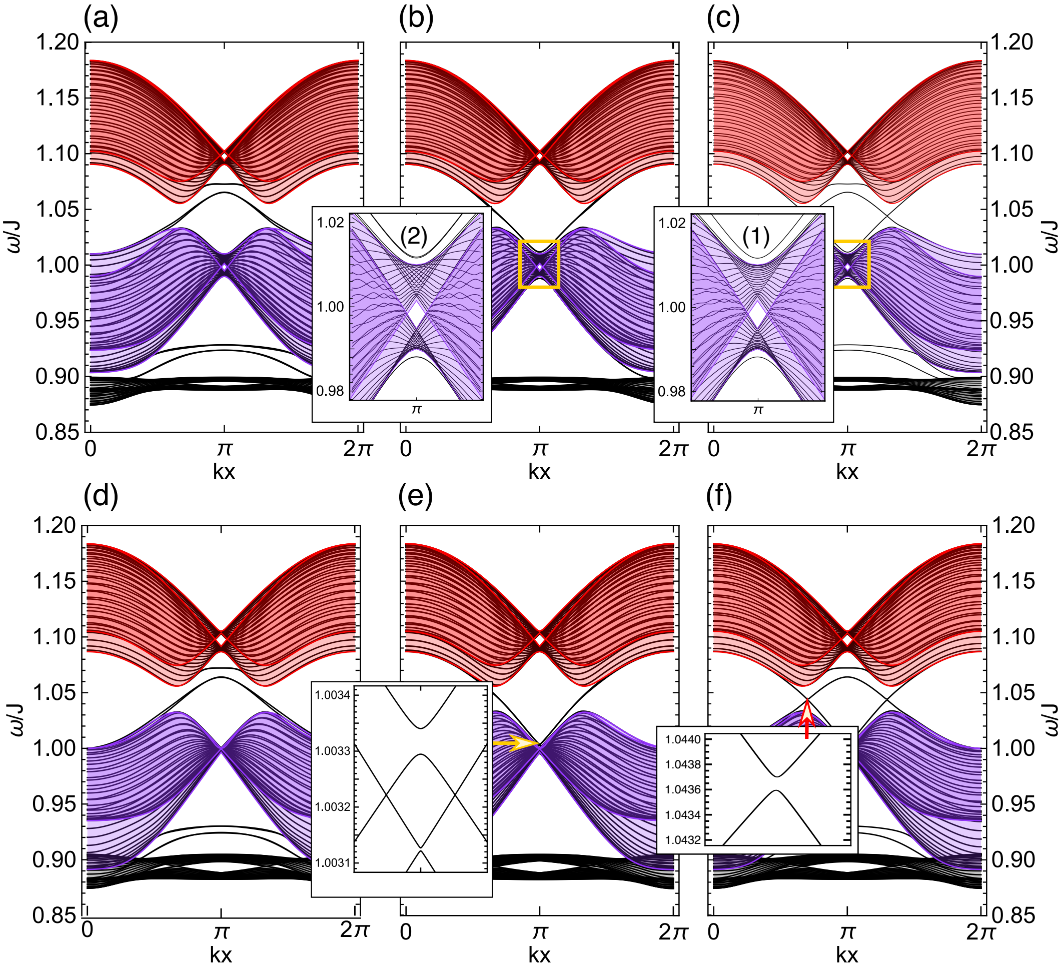

Figure 4.7: Triplon band structure in the presence of nematic interaction, calculated for the open cluster geometries shown in figure 4.6. (a-c) the parameters are $J' = 0.1J$, $D'' = 0.01J$, and $K_{\parallel} = 0.02J$. As seen in each case, within the band-gap the edge-modes and avoid crossing the gap. (a) in the flat geometry this is easily visible as the edge-modes do not approach each-other in the gap. (b) and (c) the edge-modes approach the bulk bands where they hybridize and avoid crossing into the bulk bands. (d-f) The $J' = 0.1J$, $D'' = 0.01J$, and $K'_{\parallel} = 0.01J$. Here the situation is similar and we have qualitatively the same edge-modes. The inset of (f) shows how the edge-modes themselves hybridize within the gap and thereby avoid crossing.

This is why the Krämer's degeneracy at TRIM is protected. However PTR is the relevant symmetry of our system, and our model is not PTR invariant. Because of this the Nematic terms are allowed, which do not commute with PTR. This is why we do not have a Krämer's degenerate system. When the triplon bands hybridize the spectrum becomes gapped at the TRIM. We no longer have a protected degeneracy, and therefore the $\mathcal{Z}_2$ topology is lost.

This can be shown by considering the commutation of the PTR operator with the Hamiltonian. We will for convenience define

$$\mathcal{T} = \sigma_z \otimes \boldsymbol{I}_{3\times 3}. \tag{4.81}$$

Within the particle (hole) subspace this acts as a PTR operator and we can recover the total PTR operator as

$$\Theta = \boldsymbol{I}_{2\times 2} \otimes \mathcal{T}. \tag{4.82}$$

We can now write the matrix form of the commutator as

$$\Theta \Sigma_z \boldsymbol{H}_k^{(1,-1)} - \Sigma_z \boldsymbol{H}_k^{(1,-1)} \Theta = \Sigma_z \begin{bmatrix} [\mathcal{T}, \boldsymbol{M}_k] & [\mathcal{T}, \boldsymbol{N}_k] \\ [\mathcal{T}, \boldsymbol{N}_k] & [\mathcal{T}, \boldsymbol{M}_k] \end{bmatrix}. \tag{4.83}$$

Since $\boldsymbol{N}_k$ block can be obtained from $\boldsymbol{M}_k$ by removing the diagonal and multiplying by -1, it is enough to consider the commutator with $\boldsymbol{M}_k$. We have the following equations which describe the effect of PTR on each term in $\boldsymbol{M}_k$

$$\mathcal{T}(s^\alpha \otimes \lambda_n)\mathcal{T}^\dagger = -s^\alpha \otimes \lambda_n^* \tag{4.84}$$

$$\mathcal{T}(\boldsymbol{I}_{2\times 2} \otimes \lambda_n)\mathcal{T}^\dagger = \boldsymbol{I}_{2\times 2} \otimes \lambda_n^* \tag{4.85}$$

$$\mathcal{T}(s^\alpha \otimes \boldsymbol{I}_{3\times 3})\mathcal{T}^\dagger = -s^\alpha \otimes \boldsymbol{I}_{3\times 3}. \tag{4.86}$$

From this we can conclude whether or not $\boldsymbol{M}_k$ commutes with $\mathcal{T}$. The terms $\boldsymbol{I}_{2\times 2} \otimes \lambda_n$ commute if the Gell-Mann matrix λ_n is real, but not if it's imaginary. Therefore the M_k^{XXZ} term commutes. The $s^\alpha \otimes \lambda_n$ terms commute only when λ_n is imaginary, which means that the DM terms of M_k^{DM} will commute, however M_k^{Nematic} does not.

This can be verified by calculating the bands of the open geometry. Returning to the kagome lattice geometry of figure 4.6 we calculate the bands again, but this time with a non-zero nematic interaction both on the dimer and nearest neighbor inter-dimer. The results are shown in figure 4.7. The nematic terms mix the edge-modes in such a way that they either hybridize with the bulk bands or with each-other. In both cases they avoid crossing and merge back into the bulk.

4.5 Thermal Hall and spin Nernst coefficients

In the previous sections we discussed the topology of the bilayer kagome triplon bands with and without the bond-nematic spin interaction. We showed that when it is absent, the triplons separate into 3 blocks based on their m quantum number. Each of these blocks are affected by a DM term which causes the bands to be topologically non-trivial. In this regime the topological invariant of the bands is the spin-Chern

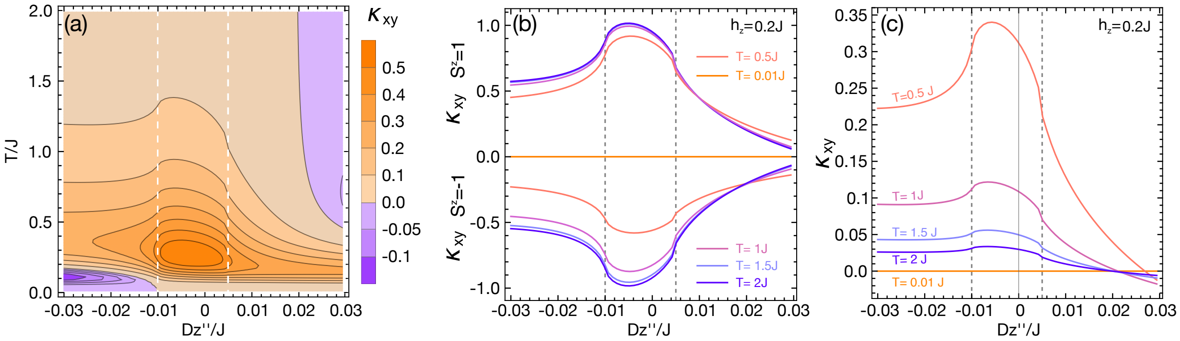

Figure 4.8: (a) We compute the thermal Hall coefficient at finite temperatures for a range of values of the next-nearest neighbor DM interaction D'' with $D' = 0.01J$, following the dashed line of the phase diagram in figure 4.3. The two dashed vertical lines correspond to the topological phase transitions of $D'' = -D'$ and $D'' = D'/2$ respectively. The magnetic field strength is $h_z = 0.2J$. (b) The contributions to the Thermal Hall coefficient of each m block is calculated over this same range of D''. Each line corresponds to a different temperature. (c) The contributions of each m from (b) is here summed to obtain the total thermal Hall coefficient.

number.

We also showed that as soon as the nematic interaction is non-zero, the bands belonging to different m hybridize and lose their global degeneracy. The $\mathcal{Z}_2$ topology has to be protected by PTR symmetry, which in this case is broken by the spin-nematic terms. These spin-nematic terms cause the bands belong to $m = 1$ and -1 to hybdridize, thus opening a gap. This is verifiable by calculating the band-spectrum with an open cylindrical geometry.

We now shift our focus to experimental signals that arise from these band-structures. For this purpose we study the model in the absence of the nematic interaction. In this case PTR is not broken and the triplet bands have $\mathcal{Z}_2$ topology. We can write it very simply as

$$\hat{M}^{\text{Zeeman}}_{m,k} = -mh_z\boldsymbol{I}_{3\times 3}. \tag{4.87}$$

The effect of this term is to move each m block up and down in energy space. At $h_z = 0$ the bands will overlap and be concentrated around the excitation energy of the dimer, which is given by J. Here the ± 1 bands are globally degenerate, and although the $m = 0$ bands are not affected by DM, the real part of their dispersion is identical to that of the spinful bands.

By applying a heat gradient across the system a thermal energy current can be generated. There's a direct component to this current lying in the negative direction of the thermal gradient, but there is also the thermal Hall component

$$j_{\text{TH}} = \kappa_{xy}\hat{\mathbf{z}} \times \nabla T. \tag{4.88}$$

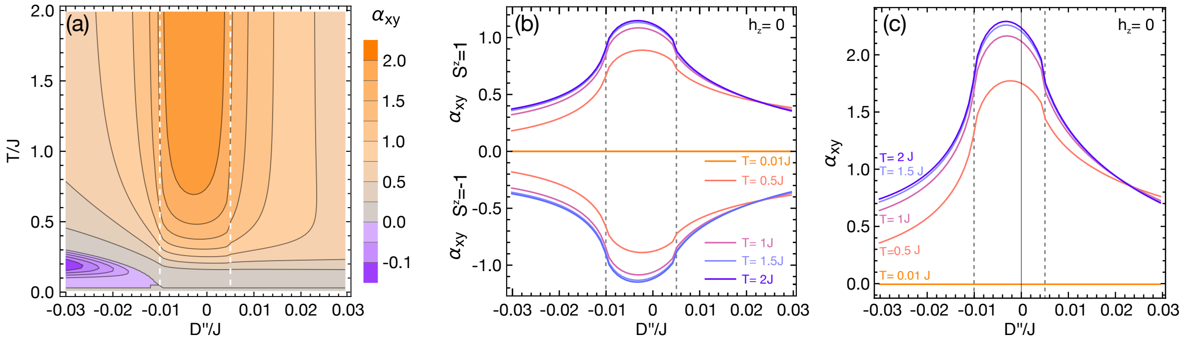

Figure 4.9: (a) We compute the spin Nernst coefficient at finite temperatures for a range of values of the next-nearest neighbor DM interaction D'' with $D' = 0.01J$, following the dashed line of the phase diagram in figure 4.3. The two dashed vertical lines correspond to the topological phase transitions of $D'' = -D'$ and $D'' = D'/2$ respectively. The magnetic field strength is $h_z = 0$. (b) The contributions to the spin Nernst coefficient of each m block is calculated over this same range of D''. Each line corresponds to a different temperature. (c) The contributions of each m from (b) is here summed with a prefactor of m to obtain the spin Nernst coefficient.

For bosonic excitations the thermal Hall coefficient is

$$\kappa_{xy} = -i\frac{1}{\beta}\sum_{n,m}\int_{\text{BZ}} c_2(\rho(\epsilon_{n,m}))\Omega_{n,m}(k_x,k_y)d^2\mathbf{k} \tag{4.89}$$

$$= -i\frac{1}{\beta}\sum_{n,m}\int_{\text{BZ}} mc_2(\rho_{n,m})\Omega_{n,1}(k_x,k_y)d^2\mathbf{k} \tag{4.90}$$

Here $\Omega_{n,m}(k_x,k_y)$ is the Berry curvature of the n'th band belonging to block m. $\rho(\epsilon_{n,m})$ is the Bose distribution. The last equality follows from the fact that the Berry's curvature of the spinless bands is 0 whereas $\Omega_{n,1}(k_x,k_y) = -\Omega_{n,-1}(k_x,k_y)$. Here

$$c_2(x) = \int_0^x \ln^2(1+t^{-1})dt. \tag{4.91}$$

By tuning h_z we can move the ±1 bands up and down in energy until they no longer overlap. At finite temperatures, each band is populated according to the Bose-Einstein distribution $\rho(\epsilon_{n,m})$. Therefore, breaking the degeneracy with a finite h_z introduces a difference in occupation of the $m = \pm 1$ bands, which is necessary to see a finite thermal Hall effect in the triplon system. With a magnetic field $h_z = 0.2J$ we obtain the thermal Hall coefficient plotted in figure 4.8. Here the the value of the thermal Hall coefficient has been for a range of temperatures and values of D'' according to the dashed line of figure 4.3. Topological phase transitions are indicated with dashed lines at $D'' = -0.01$ and $D'' = 0.005$. Due to their bosonic statistics, the triplons do not yield a sharp step-like signature of these phase transitions. However, at those points the change in thermal Hall coefficient is very large with respect to D''. This can be interpreted as a result of the Berry's curvature of two bands being swapped when they touch, as seen in figure 4.4.

If $h_z = 0$, then the application of a heat gradient will result in the currents with

$m = 1$ and $m = -1$ having opposite transverse components. Thus there will be no net thermal Hall effect. However, those two components carry opposite spin, and therefore will contribute an equal spin-current. This results in a spin-Nernst effect with transport coefficient [129]

$$\alpha_{xy} = -i \sum_{n,m} \int_{\text{BZ}} m c_1(\rho(\epsilon_{n,m}))\Omega_{n,m}(k_x, k_y) d^2\mathbf{k}. \tag{4.92}$$

Here

$$c_1(x) = \int_0^x \ln(1 + t^{-1}) dt = (1 + x)\ln(1 + x) - x \ln x. \tag{4.93}$$

This is computed in figure 4.9. Here the spin-Nernst coefficient is calculated again along the dashed line of figure 4.3. We again indicate topological phase transitions with dashed lines at $D'' = -0.01$ and $D'' = 0.005$. Again there are inflection points due to the way the Berry's curvature gets redistributed across the bands.

4.6 Conclusions

We have investigated the bond-wave Hamiltonian of a bilayer anti-ferromagnetic kagome lattice model. Admitting only intra-dimer, nearest and next-nearest inter-dimer terms, we find that the model does not support a $\mathcal{Z}_2$ topological phase even though it is TR symmetric. We investigate the relevant pseudo-time-reversal symmetry of the model, and find that the nematic terms we describe violate it, although in general they are allowed by the D_{6h} point group. We supported this claim by calculating the band spectrum with an open geometry with an without those terms present. We thereby verified the presence of helical edge-modes when those terms are not present. We also showed that when the nematic terms appear, they hybridize those edge-modes and prevent them from connecting the bulk bands.

Additionally we have provided analytical results for the Chern numbers of the effective two-band models associated with each band-gap in the limit where bands are separable into 3 different $\hat{S}^z = m$ components. We also calculated the triplon mediated thermal Hall and spin Nernst coefficients. As expected these band-structures give rise to responses which in principle can be measured experimentally. However, although the existence of these topological phases implies that such signals will be present, the converse may not be the case, as it is easy to imagine these signals appearing even for topologically trivial bands.

Chapter 5

From half-moons to Chern numbers

In previous chapters, we remarked that topological magnetic excitations can be associated with a thermal Hall effect. However, even in topologically trivial materials, the thermal Hall signal may still be non-zero. The reason for this is that the excitations we discussed, either triplons or magnons are bosonic in nature. Although topologically trivial bands have a Berry curvature that integrates up to 0, the Berry curvature may still be non-zero locally, and since the bosonically distributed magnons have an energy dependent statistical weight, the contribution to the transverse transport of the higher and lower energy parts will not in general cancel out.

In this chapter we instead focus on neutron scattering features and show how they may reveal the topology of a magnon band-structure. In neutron scattering experiments, two particular features tend to appear across a wide range of materials with plaquette like structures. These are the so-called pinch-point and half-moon features, which are often associated with pyrochlore and kagome materials [155, 156]. It has already been shown that these features are different projections of the same phenomenon in the spin-spin structure factor [157]. We will therefore describe them simply as half-moons here.

We analyze kagome in the field-aligned phase and show that half-moons here arise from constraints imposed by symmetry and that they signal topologically non-trivial bands. Using the magnetic point group of the spin-polarized phase we derive constraints which guarantee topological band-gaps at high-symmetry points as well as half-moon features on both of the touching bands. The remarkable finding here is that both the non-trivial band topology and the characteristic spectral features originate from the magnetic point-group symmetry.

As outlined in Section 3.4, the topology of magnon bands can be investigated by constructing an effective field theory at the high-symmetry points where two of the three magnon bands touch. The symmetries of the lattice impose a winding of $\vec{d}_k$ around the high symmetry points of the Brillouin zone. Because of this, each band-gap endows the bands with a Berry curvature. It is this same winding which manifests as half-moons in the structure factor $S_k(\omega)$, and we find that the winding number of $\vec{d}_k$ is identical to the number of intensity minima and maxima observed. This is similar to previous discussions about half-moons in the context of magnon Weyl points [158].

This is supplemented with spin-wave calculations which support this claim. We

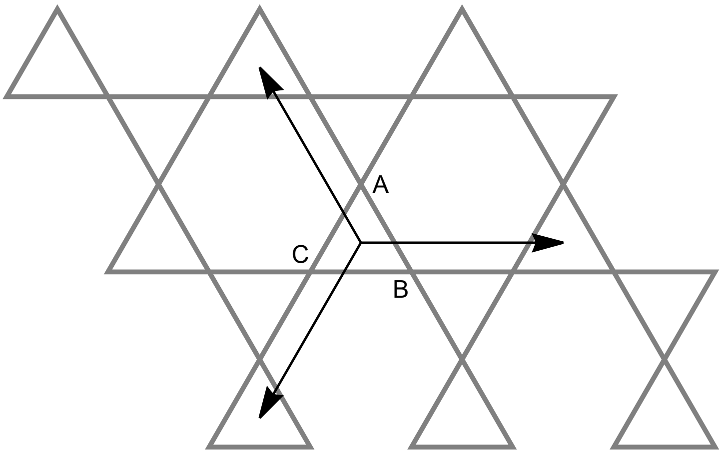

Figure 5.1: The kagome lattice with unit vectors indicated.

also derive a topological phase-diagram and study the transition between a DM-induced topological phase and one induced by Kitaev-like anisotropic interactions.

5.1 The kagome lattice geometry and point group

As a sufficiently general example, we consider a $S = 1/2$ magnet on a kagome lattice, which has been fully polarized by an applied magnetic field. The symmetries of the relevant point group D_{6h} are indicated on figure 5.1. The Hamiltonian must be invariant under application of the elements contained in this group. It is also invariant under translation by the lattice vectors

$$\begin{aligned} \delta_1 &= [1,0]^T \\ \delta_2 &= [-1/2, \sqrt{3}/2]^T \\ \delta_3 &= [-1/2, -\sqrt{3}/2]^T. \end{aligned} \tag{5.1}$$

We also define the reciprocal lattice vectors

$$\begin{aligned} \Delta_1 &= 2\pi[0, 2/\sqrt{3}]^T \\ \Delta_2 &= 2\pi[-1, -1/\sqrt{3}]^T \\ \Delta_3 &= 2\pi[1, -1/\sqrt{3}]^T. \end{aligned} \tag{5.2}$$

A generic form of such a Hamiltonian would be

$$\hat{H}^{\text{Generic}} = \sum_{i,j} \sum_{\alpha,\beta} J_{i,j}^{\alpha,\beta} \hat{S}_i^{\alpha} \hat{S}_j^{\beta}. \tag{5.3}$$

We can add a term which explicitly breaks TR symmetry as

$$\hat{H} = \hat{H}^{\text{Generic}} - h_z \sum_i \hat{S}_i^z. \tag{5.4}$$

We now imagine that h_z is large enough to saturate the spins. Now we may carry out spin-wave theory using the fully polarized state with $\langle \hat{S}_i^z \rangle = S$ as the ground state. Doing so results in a Bogoliubov-de-Gennes Hamiltonian of the form

$$\hat{H}_k^{BdG} = \mathbf{v}_k^\dagger \begin{bmatrix} \boldsymbol{M}_k & \boldsymbol{N}_k \\ \boldsymbol{N}_k^\dagger & \boldsymbol{M}_k^* \end{bmatrix} \mathbf{v}_k \tag{5.5}$$

with $\mathbf{v}_k = [\hat{a}_k, \hat{b}_k, \hat{c}_k, \hat{a}_{-k}^\dagger, \hat{b}_{-k}^\dagger, \hat{c}_{-k}^\dagger]$. For this very generic form of the Hamiltonian, we will in the following sections elaborate on the allowed matrix elements. We do so by considering the magnetic point group symmetry which remains after TR is broken by either a spin-polarizing magnetic field h^z or spontaneous magnetization (in the case of a ferromagnet).

In the final section we will show results from spin-wave theory considering the model

$$\hat{H} = \sum_{\langle i,j \rangle} \mathbf{S}_i \boldsymbol{J}_{i,j} \mathbf{S}_j - h^z \sum_i \hat{S}_i. \tag{5.6}$$

Here the tensor $\boldsymbol{J}_{i,j}$ depends on the sub-lattices of i and j as

$$\boldsymbol{J}_{B,C} = \begin{bmatrix} J_x & D_z & 0 \\ -D_z & J_y & 0 \\ 0 & 0 & J_z \end{bmatrix} \quad \boldsymbol{J}_{C,A} = \begin{bmatrix} \frac{1}{4}(J_x + 3J_y) & \frac{\sqrt{3}}{4}(J_x - J_y) + D_z & 0 \\ \frac{\sqrt{3}}{4}(J_x - J_y) - D_z & \frac{1}{4}(3J_x + J_y) & 0 \\ 0 & 0 & J_z \end{bmatrix}$$
$$\boldsymbol{J}_{A,B} = \begin{bmatrix} \frac{1}{4}(J_x + 3J_y) & -\frac{\sqrt{3}}{4}(J_x - J_y) + D_z & 0 \\ -\frac{\sqrt{3}}{4}(J_x - J_y) - D_z & \frac{1}{4}(3J_x + J_y) & 0 \\ 0 & 0 & J_z \end{bmatrix} \tag{5.7}$$

This is the most general nearest-neighbor spin interaction model on kagome allowed by the D_{6h} point-group [159]. We will use this to numerically calculate the Chern numbers of magnon bands.

5.2 Magnon irreducible representations

In this section we derive the irreducible representations of magnons under $D_{6h}(C_{6h})$. Doing so will allow us to determine the allowed matrix elements of $\hat{H}_k$ in the basis of magnon operators. Then, in the next section, we will make use of this to construct the effective field model of touching bands.

The point group we use is $D_{6h}(C_{6h})$. This is the magnetic point group that appears when a material which is described by the symmetry group D_{6h} orders in such a way that the spins follow its subgroup C_{6h}. This is the case for instance when the material is polarized by a $-h\hat{S}^z$ term. The way that we construct $D_{6h}(C_{6h})$ from C_{6h} and D_{6h} is to take the complement to C_{6h} and apply time-reversal symmetry with those operations.

$$D_{6h}(C_{6h}) = C_{6h} \oplus \tau \times (D_{6h} \backslash C_{6h}) \tag{5.8}$$

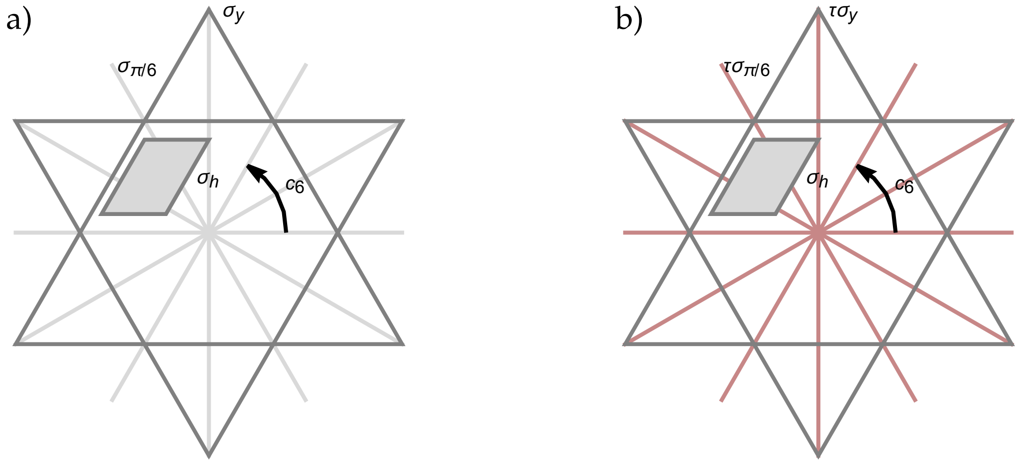

Figure 5.2: Here we depict the elements of (a) D_{6h} and (b) $D_{6h}(C_{6h})$. The horizontal plane of reflection σ_h, and the 6-fold rotation c_6 are indicated on both figures. The vertical planes of reflection in (b) must be applied together with time-reversal, which we indicate by coloring them red, as opposed to (a) where they are gray.

The × operation here is defined as

$$A \times \{g_1, g_2, \dots, g_n\} = \{Ag_1, Ag_2, \dots, Ag_n\} \tag{5.9}$$

Table 5.1: The generators of $D_{6h}(C_{6h})$. We tabulate their action on spin operators including step up and down operators, as well as site indices. Here $\omega = e^{i2\pi/3}$.

$D_{6h}(C_{6h})$	c_6	$\tau\sigma_y$	σ_h
$\hat{S}^x$	$\frac{1}{2}\hat{S}^x + \frac{\sqrt{3}}{2}\hat{S}^y$	$\hat{S}^x$	$-\hat{S}^x$
$\hat{S}^y$	$-\frac{\sqrt{3}}{2}\hat{S}^x + \frac{1}{2}\hat{S}^y$	$-\hat{S}^y$	$-\hat{S}^y$
$\hat{S}^z$	$\hat{S}^z$	$\hat{S}^z$	$\hat{S}^z$
$\alpha\hat{S}^+$	$-\omega\alpha\hat{S}^+$	$\alpha^*\hat{S}^+$	$-\alpha\hat{S}^+$
$\alpha\hat{S}^-$	$-\omega^*\alpha\hat{S}^-$	$\alpha^*\hat{S}^-$	$-\alpha\hat{S}^-$
A	B	A	A
B	C	C	B
C	A	B	C

Magnons are created by application of the $\hat{S}^-$ operator to the ordered state and therefore should transform in the same way. This is clear from the Holstein-Primakoff transform which gives

$$\hat{S}^- = \hat{a}^\dagger \sqrt{1 - \frac{\hat{a}^\dagger \hat{a}}{2S}}. \tag{5.10}$$

Everything under the square root transforms as a scalar, so the magnon creation operator must transform exactly as $\hat{S}^-$. Conversely, the annihilation operator must transform as $\hat{S}^+$.

To continue, we first notice that inversion can be used as a generator in place of

σ_h since

$$\sigma_h = {c_6}^3 i. \tag{5.11}$$

This is more convenient, since the inversion symmetry acts as an identity operator on spins and sublattice indeces. So for the purposes of writing up the irreducible representations of magnons we can make use of only the subgroup generated by c_6 and $\tau\sigma_y$. We can write up explicitly how each element acts on the magnons. Here each magnon creation operator is labeled according to its sublattice. We also include a complex prefactor α to account for the conjugation due to τ. We will also shorten the notation and introduce $\tilde{\sigma}_\theta = \tau\sigma_\theta$, where θ is the angle that the plane of reflection makes with the y-axis.

Table 5.2: The action of the magnetic point group on magnons on sublattices A, B and C respectively. Here $\omega = e^{i2\pi/3}$. We label each plane of reflection $\tau\sigma_v \equiv \tilde{\sigma}_\theta$, with the θ being angle that the plane makes with the y-axis. Each $\tilde{\sigma}_\theta$ of the bottom row is obtained by the composition $\tilde{\sigma}_\theta = g \circ \tilde{\sigma}_{0^\circ}$, where g is from the top row. For instance $\tilde{\sigma}_{\pi/6} = c_6 \circ \tilde{\sigma}_0$

g	e	c_6	c_3	c_2	${c_3}^2$	${c_6}^5$
$g : \alpha\hat{a}^\dagger$	$\alpha\hat{a}^\dagger$	$-\omega^*\alpha\hat{b}^\dagger$	$\omega\alpha\hat{c}^\dagger$	$-\alpha\hat{a}^\dagger$	$\omega^*\alpha\hat{b}^\dagger$	$-\omega\alpha\hat{c}^\dagger$
$g : \alpha\hat{b}^\dagger$	$\alpha\hat{b}^\dagger$	$-\omega^*\alpha\hat{c}^\dagger$	$\omega\alpha\hat{a}^\dagger$	$-\alpha\hat{b}^\dagger$	$\omega^*\alpha\hat{c}^\dagger$	$-\omega\alpha\hat{a}^\dagger$
$g : \alpha\hat{c}^\dagger$	$\alpha\hat{c}^\dagger$	$-\omega^*\alpha\hat{a}^\dagger$	$\omega\alpha\hat{b}^\dagger$	$-\alpha\hat{c}^\dagger$	$\omega^*\alpha\hat{a}^\dagger$	$-\omega\alpha\hat{b}^\dagger$

g	$\tilde{\sigma}_0$	$\tilde{\sigma}_{\pi/6}$	$\tilde{\sigma}_{\pi/3}$	$\tilde{\sigma}_{\pi/2}$	$\tilde{\sigma}_{2\pi/3}$	$\tilde{\sigma}_{5\pi/6}$
$g : \alpha\hat{a}^\dagger$	$\alpha^*\hat{a}^\dagger$	$-\omega^*\alpha^*\hat{c}^\dagger$	$\omega\alpha^*\hat{b}^\dagger$	$-\alpha^*\hat{a}^\dagger$	$\omega^*\alpha^*\hat{c}^\dagger$	$-\omega\alpha^*\hat{b}^\dagger$
$g : \alpha\hat{b}^\dagger$	$\alpha^*\hat{c}^\dagger$	$-\omega^*\alpha^*\hat{b}^\dagger$	$\omega\alpha^*\hat{a}^\dagger$	$-\alpha^*\hat{c}^\dagger$	$\omega^*\alpha^*\hat{b}^\dagger$	$-\omega\alpha^*\hat{a}^\dagger$
$g : \alpha\hat{c}^\dagger$	$\alpha^*\hat{b}^\dagger$	$-\omega^*\alpha^*\hat{a}^\dagger$	$\omega\alpha^*\hat{c}^\dagger$	$-\alpha^*\hat{b}^\dagger$	$\omega^*\alpha^*\hat{a}^\dagger$	$-\omega\alpha^*\hat{c}^\dagger$

By taking linear combinations of sublattice bosonic field operators $\hat{a}^\dagger$, $\hat{b}^\dagger$ and $\hat{c}^\dagger$ we can obtain the basis-functions

$$\begin{aligned}
\hat{\psi}_0^\dagger &= (\hat{a}^\dagger + \omega^*\hat{b}^\dagger + \omega\hat{c}^\dagger)/\sqrt{3} \\
\hat{\psi}_+^\dagger &= (\hat{a}^\dagger + \hat{b}^\dagger + \hat{c}^\dagger)/\sqrt{3} \\
\hat{\psi}_-^\dagger &= (\hat{a}^\dagger + \omega\hat{b}^\dagger + \omega^*\hat{c}^\dagger)/\sqrt{3}.
\end{aligned} \tag{5.12}$$

These basis functions in turn define three irreducible representations of the group $D_{6h}(C_{6h})$. We have labeled them in such a way that each $\hat{\psi}_j^\dagger$ transforms according to Γ^j. Now, we label the magnon created on the unit cell centered on r_i as $\hat{\psi}_{j,i}^\dagger$. Then we define the Fourier transformed

$$\hat{\psi}_{j,k}^\dagger = \frac{1}{\sqrt{L}} \sum_{i=1}^{L} e^{ir_i \cdot k} \hat{\psi}_{j,i}^\dagger. \tag{5.13}$$

The elements of $D_{6h}(C_{6h})$ applied to $\hat{\psi}_{j,k}$, in addition to their irreps listed in table 5.3 also transform k. Their action on k can be represented by $O(2)$ matrices according

Table 5.3: We list three irreps of $D_{6h}(C_{6h})$. Here K is complex conjugation.

g	e	c_6	c_3	c_2	${c_3}^2$	${c_6}^5$
$\Gamma^0(g)$	1	-1	1	-1	1	-1
$\Gamma^+(g)$	1	$-\omega^*$	ω	-1	ω^*	$-\omega$
$\Gamma^-(g)$	1	$-\omega$	ω^*	-1	ω	$-\omega^*$

g	$\tilde{\sigma}_0$	$\tilde{\sigma}_{\pi/6}$	$\tilde{\sigma}_{\pi/3}$	$\tilde{\sigma}_{\pi/2}$	$\tilde{\sigma}_{2\pi/3}$	$\tilde{\sigma}_{5\pi/6}$
$\Gamma^0(g)$	K	$-K$	K	$-K$	K	$-K$
$\Gamma^+(g)$	K	$-\omega^* K$	ωK	$-K$	$\omega^* K$	$-\omega K$
$\Gamma^-(g)$	K	$-\omega K$	$\omega^* K$	$-K$	ωK	$-\omega^* K$

to the given rotation/reflection which is being applied. Denoting the matrix representation of the element g as $\boldsymbol{A}(g)$, we have for instance

$$\boldsymbol{A}(c_2) = -\boldsymbol{I}_{2\times 2}. \tag{5.14}$$

The reflections are combined with time-reversal which has the effect of reversing k due to complex conjugation. Finally, while inversion does not act on spins, it reverses k.

5.2.1 K and K′ subgroups

At the K and K' points, the k index is invariant under application of some of the group elements. Specifically the subgroup $C_{3v}(C_3)$ transforms k into itself at these points. We can tabulate the group and its irreps as shown on table 5.4. Here the basis functions are obtained from equation (5.13) as $\hat{\psi}^\dagger_{j,K}$ and $\hat{\psi}^\dagger_{j,K'}$. Note that in this instance, although we can use this to establish the eigenstates of the Hamiltonian at high symmetry points, in general the $\hat{\psi}^\dagger_{j,k}$ do not diagonalize the Hamiltonian at arbitrary k. It is worth noting that each of these irreps are one-dimensional, meaning that there are no symmetry-protected degeneracies at the high-symmetry points.

Table 5.4: We list three irreps of $C_{3v}(C_3)$. Here K is complex conjugation.

g	e	c_3	${c_3}^2$	$\tilde{\sigma}_0$	$\tilde{\sigma}_{\pi/3}$	$\tilde{\sigma}_{2\pi/3}$
$\Gamma^0(g)$	1	1	1	K	K	K
$\Gamma^+(g)$	1	ω	ω^*	K	ωK	$\omega^* K$
$\Gamma^-(g)$	1	ω^*	ω	K	$\omega^* K$	ωK

We have so far not discussed the role of number non-conserving terms in the Hamiltonian. In general they imply that the true eigenstates must be obtained by Bogoliubov transform

$$\hat{\Psi}^\dagger_{i,k} = \kappa_{i,k}\hat{\psi}^\dagger_{i,k} + \gamma_{i,k}\hat{\phi}_{i,k}. \tag{5.15}$$

Here $\hat{\phi}_{i,k}$, $\kappa_{i,k}$ and $\gamma_{i,k}$ are chosen such that the Hamiltonian can be written entirely in the space of $\hat{\Psi}^\dagger_{i,k}$. We describe this in Appendix C. The $\hat{\Psi}_{i,k}$ must be constructed in such a way that they transform in the same way as $\hat{\phi}_{i,k}$, and therefore the same observations about the representations of $D_{6h}(C_{6h})$ apply here. In the rest of this chapter we will use $\hat{\Upsilon}^\dagger_{i,k}$ and the kernel matrix describing the dispersion in this space is $\tilde{M}_k$. However, everything that follows is equally valid for $\hat{\psi}^\dagger_{i,k}$ and M_k.

5.3 Allowed magnon hopping terms

We now return to the question of which terms are allowed in the magnon hopping Hamiltonian. We consider the matrix elements of $\tilde{M}_k$, which we introduced in the previous section. This matrix can be written as

$$\begin{aligned}\tilde{M}_k &= \begin{bmatrix} \epsilon_{1,k} & m_{1,k} & m^*_{3,k} \\ m^*_{1,k} & \epsilon_{2,k} & m_{2,k} \\ m_{3,k} & m^*_{2,k} & \epsilon_{3,k} \end{bmatrix} && (5.16)\\ &= \sum_j \alpha_{j,k}\lambda_j + \beta_{j,k}\eta_j + e_{j,k}\nu_j. && (5.17)\end{aligned}$$

Here we introduce the real coefficients $\alpha_{j,k}$ and $\beta_{j,k}$ defined by $m_{j,k} = \alpha_{j,k} + i\beta_{j,k}$. We also define

$$\begin{aligned} e_{i,k} &= (\epsilon_{1,k} - \epsilon_{2,k})/2 \\ e_{2,k} &= (\epsilon_{2,k} - \epsilon_{3,k})/2 \\ e_{3,k} &= (\epsilon_{3,k} - \epsilon_{1,k})/2 \end{aligned} \tag{5.18}$$

For convenience, rather than writing $\tilde{M}$ in the basis of Gell-Mann matrices, we have chosen a basis

$$\begin{aligned} \lambda_1 &= \begin{bmatrix} 0 & 1 & 0 \\ 1 & 0 & 0 \\ 0 & 0 & 0 \end{bmatrix}, \lambda_2 = \begin{bmatrix} 0 & 0 & 0 \\ 0 & 0 & 1 \\ 0 & 1 & 0 \end{bmatrix}, \lambda_3 = \begin{bmatrix} 0 & 0 & 1 \\ 0 & 0 & 0 \\ 1 & 0 & 0 \end{bmatrix} \\ \eta_1 &= \begin{bmatrix} 0 & i & 0 \\ -i & 0 & 0 \\ 0 & 0 & 0 \end{bmatrix}, \eta_2 = \begin{bmatrix} 0 & 0 & 0 \\ 0 & 0 & i \\ 0 & -i & 0 \end{bmatrix}, \eta_3 = \begin{bmatrix} 0 & 0 & -i \\ 0 & 0 & 0 \\ i & 0 & 0 \end{bmatrix} \\ \nu_1 &= \begin{bmatrix} 1 & 0 & 0 \\ 0 & -1 & 0 \\ 0 & 0 & 0 \end{bmatrix}, \nu_2 = \begin{bmatrix} 0 & 0 & 0 \\ 0 & 1 & 0 \\ 0 & 0 & -1 \end{bmatrix}, \nu_3 = \begin{bmatrix} -1 & 0 & 0 \\ 0 & 0 & 0 \\ 0 & 0 & 1 \end{bmatrix}. \end{aligned} \tag{5.19}$$

For each j, the three matrices λ_j, η_j and ν_j form an $SU(2)$ sub-algebra. We will now apply the symmetries of our lattice to this Hamiltonian, under which we require it to be invariant. By doing so we will show that the $m_{j,k}$ off-diagonal elements, which mix the basis functions $[\hat{\Upsilon}_{0,k}, \hat{\Upsilon}_{+,k}, \hat{\Upsilon}_{-,k}]^T$, follow certain constraints.

One of the elements of $D_{6h}(C_{6h})$ is the reflection through the x,z-plane combined with TR. In table 5.3 we wrote this as $\tilde{\sigma}_{\pi/2}$. This operation defines a line in k-space, $k_x = 0$ where k is transformed into itself, first by reflection through the x,z-plane, then by TR. Along this line, we can represent the action of $\tilde{\sigma}_{\pi/2}$ by its action on the

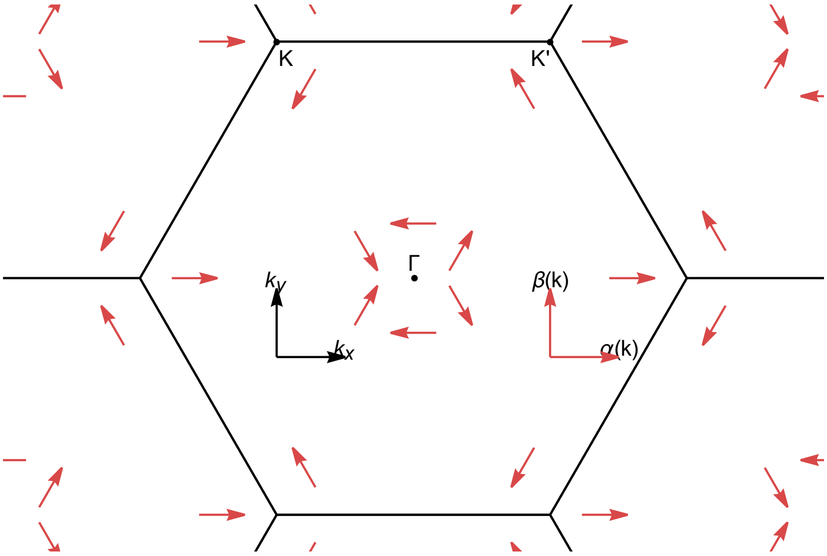

Figure 5.3: We here plot the orientation of $m_{j,k} = \alpha_{j,k} + i\beta_{j,k}$ of equation (5.17) in the complex plane at points in the Brillouin zone where it is fixed by symmetry.

$[\hat{\Psi}_{0,k}, \hat{\Psi}_{+,k}, \hat{\Psi}_{-,k}]^T$ space, which is

$$\boldsymbol{A}(\tilde{\sigma}_{\pi/2}) = \begin{bmatrix} -1 & 0 & 0 \\ 0 & -1 & 0 \\ 0 & 0 & -1 \end{bmatrix} K. \tag{5.20}$$

Here K is complex conjugation. We have

$$\boldsymbol{A}(\tilde{\sigma}_{\pi/2})\tilde{\boldsymbol{M}}_{k_x=0}\boldsymbol{A}(\tilde{\sigma}_{\pi/2}) = \tilde{\boldsymbol{M}}_{k_x=0}, \tag{5.21}$$

so $\tilde{\sigma}_{\pi/2}$ puts a constraint on the Hamiltonian, which we can restate simply by recognizing that

$$\boldsymbol{A}(\tilde{\sigma}_{\pi/2})\eta_j\boldsymbol{A}(\tilde{\sigma}_{\pi/2}) = -\eta_j. \tag{5.22}$$

This means that along the $k_x = 0$ line in the Brillouin zone $\beta_{j,k_x=0} = 0$, or equivalently $m_{j,k_x=0}$ is real. This does not reveal anything about the magnitude of these coefficients or their sign. However, we can now relate each $m_{j,k_x=0}$ with its corresponding value elsewhere in the Brillouin zone. Starting at some point $k' = (0, k_y)$, the c_6 rotation must take this point into $k'' = (-\sqrt{3}k_y/2, k_y/2)$. At the same time, it acts on the $[\hat{\Psi}_{0,k}, \hat{\Psi}_{+,k}, \hat{\Psi}_{-,k}]^T$ as

$$\boldsymbol{A}(c_6) = \begin{bmatrix} -1 & 0 & 0 \\ 0 & -\omega^* & 0 \\ 0 & 0 & -\omega \end{bmatrix}. \tag{5.23}$$

The inverse of c_6 is ${c_6}^5$. We can equate

$$
\begin{aligned}
\tilde{M}_{k''} &= \boldsymbol{A}(c_6)\tilde{M}_{k'}\boldsymbol{A}(c_6)^5 && (5.24)\\
&= \begin{bmatrix} \epsilon_{1,k} & \omega m_{1,k} & \omega^* m^*_{3,k} \\ \omega^* m^*_{1,k} & \epsilon_{2,k} & \omega m_{2,k} \\ \omega m_{3,k} & \omega^* m^*_{2,k} & \epsilon_{3,k} \end{bmatrix}. && (5.25)
\end{aligned}
$$

Thus it will take $m_{j,(0,k_y)} = \alpha_{j,(0,k_y)}$ into $m_{j,(-\sqrt{3}k_y/2,k_y/2)} = -\alpha_{j,(0,k_y)}/2 + i\sqrt{3}\alpha_{j,(0,k_y)}/2$. In other words c_6 performs a $U(1)$ rotation on $m_{j,k}$ by the constant ω. Successive applications of c_6 amounts to rotations in k and in the complex plane of $(\alpha_{i,k}, \beta_{i,k})$.

We visualize the effect of this rotation in figure 5.3 where we have drawn arrows corresponding to the allowed orientations of $m_{i,k}$ in the complex plane at points in the Brillouin zone that are connect by c_6. Here it is clear that a winding feature is drawn out by $m_{i,k}$, twice around the Γ-point and once around K and K'. We cannot relate the magnitudes of $m_{j,k}$ with distinct j, and in general they could have different signs as well.

5.4 Two-band effective models

The rules we derived above define a winding feature for each $m_{j,k}$. Here $m_{1,k}$ is the matrix element which mixes $\hat{\Psi}^\dagger_{0,k}$ and $\hat{\Psi}^\dagger_{+,k}$, and so on. Each j combination of the λ_j, η_j and ν_j matrices together with the 2×2 identity matrix form an $SU(2)$ sub-algebra, where they correspond exactly to Pauli matrices.

In the spin-polarized phase, if the model has pure Heisenberg interactions, there will be a degeneracy at the Γ point where the two lower-energy bands touch, as well as at the K and K' points where it is the higher energy bands that become degenerate. When a gap is introduced due to some perturbative interaction, to a good approximation we can treat the Hamiltonian in the vicinity of the gap as a 2×2 effective model, whilst neglecting the third band.

In doing so we are also not including corrections which would follow from a canonical basis transform. These terms would be $O(t^2/\Delta)$, where Δ is the gap in energy from the 2×2 block to the third band, and t is an off-diagonal matrix element connecting them. To see in detail how this is done and the implications, we formally treat the pairing terms through a canonical transform in Section C.1.

At the Γ point the effective 2×2 model is written in the $[\hat{\Psi}_{0,k}, \hat{\Psi}_{-,k}]^T$ basis, at K and K' it is $[\hat{\Psi}_{+,k}, \hat{\Psi}_{-,k}]^T$ and $[\hat{\Psi}_{+,k}, \hat{\Psi}_{0,k}]^T$ respectively. Writing up the effective model gives us

$$
\begin{aligned}
\hat{M}^{\text{eff}}_{j,k} &= (\epsilon_{j,k} + \epsilon_{j+1,k})\boldsymbol{I}_{2\times 2}/2 + \alpha_{j,k}\sigma^x + \beta_{j,k}\sigma^y + e_{j,k}\sigma^z && (5.26)\\
&= (\epsilon_{j,k} + \epsilon_{j+1,k})\boldsymbol{I}_{2\times 2}/2 + \mathbf{d}_{j,k} \cdot \boldsymbol{\sigma}. && (5.27)
\end{aligned}
$$

In Section 3.1 we described the topology of such two-band models in terms of a topological flux through a surface defined by the $\mathbf{d}_{j,k}$ vector. We have no constraints on the $e_{j,k}$, and therefore we cannot make any comments on the sign of $d^z_{j,k}$ or its magnitude. We can however make comments about $\alpha_{j,k}$ and $\beta_{j,k}$, which must wind around the high-symmetry points of the Brillouin zone. As explained in Section 3.1, for a constant $d^z_{j,k}$, this winding ensures that the Berry's flux integrates up to πn, where n is the winding number.

At the Γ-point, the bands which touch are $\hat{\Psi}_{0,\Gamma}$ and $\hat{\Psi}_{-,\Gamma}$. At the K point they are $\hat{\Psi}_{+,\Gamma}$, $\hat{\Psi}_{-,\Gamma}$ and at K' they are $\hat{\Psi}_{0,\Gamma}$, $\hat{\Psi}_{+,\Gamma}$. Although $e_{j,k}$ has to be the same at K and K' due to inversion symmetry, it is generally different at Γ. If the sign of both are known then the Chern numbers of each band can be determined.

The band-gap at the Γ-point only guarantees an added ±1 to the Chern number of the bottom and middle bands, but we cannot tell from these arguments alone which band gets which contribution. We cannot tell what the total Chern number on the middle band integrates up to either, but the bottom band must be non-zero, as there are no other band-gaps which can endow it with a Chern number. At K and K' the band-gaps each contribute $\pm 1/2$ to the Chern number due to the single-winding feature. By a similar logic, the top band must also have a non-zero Chern number. This is summarized in table 5.5.

Table 5.5: We tabulate the Chern numbers here depending on the sign of $e_{3,\Gamma}$ and $e_{1,K} = e_{2,K'}$. The Chern numbers are labeled c_i according to band energy in ascending order.

$\mathrm{sgn}(e_{3,\Gamma})$	$\mathrm{sgn}(e_{1,K})$	c_1	c_2	c_3
$+1$	$+1$	-1	0	1
$+1$	-1	-1	2	-1
-1	$+1$	1	-2	1
-1	-1	1	0	-1

In this derivation we have not made any assumptions about model parameters or even whether they are nearest-neighbor or next-nearest neighbor. Our finding is that the topology of magnon bands in kagome arises from the point group symmetry, which imposes constraints on the matrix elements of the magnon hopping Hamiltonian. Thus spin-polarized or ferromagnetic kagome is always accompanied by topologically non-trivial magnon bands.

5.5 Implications for the structure factor

The effective field models we have defined using $\mathbf{d}_{j,k}$ imply an orientation on the Bloch sphere that can be parametrized by a set of angles $\theta_{j,k}$ and $\phi_{j,k}$, such that

$$\begin{aligned} d^x_{j,k} &= \alpha_{j,k} = d^0_{j,k} \sin\theta \cos\phi \\ d^y_{j,k} &= \beta_{j,k} = d^0_{j,k} \sin\theta \sin\phi \\ d^z_{j,k} &= e_{j,k} = d^0_{j,k} \cos\theta. \end{aligned} \tag{5.28}$$

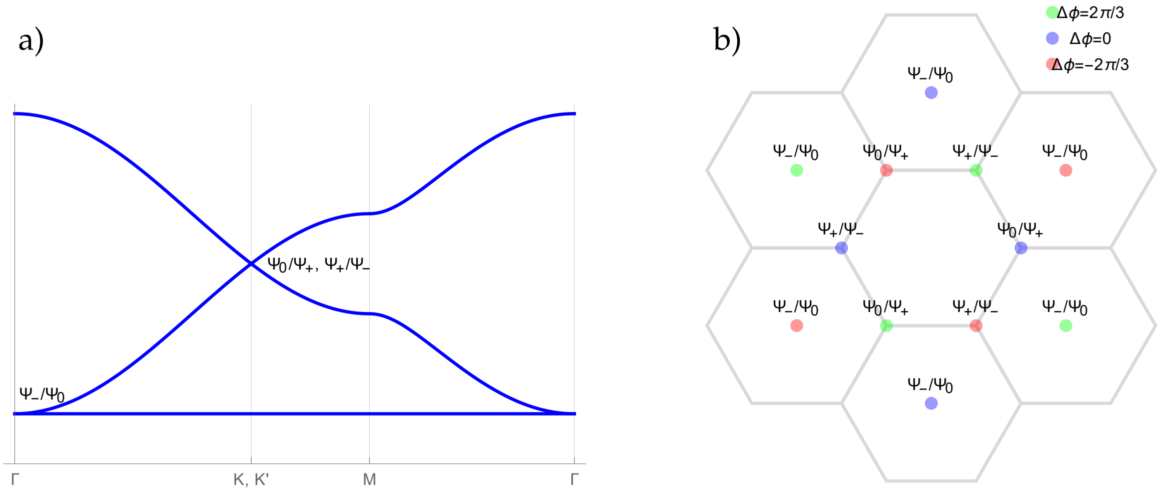

Figure 5.4: (a) Here we show the spectrum of kagome magnon bands. $\hat{\Psi}^\dagger_{-,k}$ and $\hat{\Psi}^\dagger_{0,k}$ touch at Γ, $\hat{\Psi}^\dagger_{0,k}$ and $\hat{\Psi}^\dagger_{+,k}$ at K and $\hat{\Psi}^\dagger_{+,k}$ and $\hat{\Psi}^\dagger_{-,k}$ at K'. (b) The 1st Brillouin zone, and its nearest neighbors. Here the phase $\Delta\phi$ must be taken into account when calculating the structure factor. This picture shows where the band-touching points of (a) lie in k-space.

At Γ, K and K', the only non-zero component of $\mathbf{d}_{j,k}$ is $d^z_{j,k}$. Moving away from this point, in the limit of $\cos\theta \to 0$ the mixing of the bands results in two eigenstates defined by

$$\hat{\Theta}^\dagger_{\pm,p,q,k} = (\hat{\Psi}^\dagger_{p,k} \pm e^{i\phi_j}\hat{\Psi}^\dagger_{q,k})/\sqrt{2}. \tag{5.29}$$

We may calculate the dynamical structure factor in the vicinity of one of the reciprocal lattice vectors $q = \pm\Delta_j$. For reader convenience we rewrite them here

$$\begin{aligned} \Delta_1 &= 2\pi[0, 2/\sqrt{3}]^T \\ \Delta_2 &= 2\pi[-1, -1/\sqrt{3}]^T \\ \Delta_3 &= 2\pi[1, -1/\sqrt{3}]^T. \end{aligned} \tag{5.30}$$

Here it is $\hat{\Psi}^\dagger_{0,k}$ and $\hat{\Psi}^\dagger_{-,k}$ which mix, so we set $\hat{\Theta}^\dagger_{\pm,k} = \hat{\Theta}^\dagger_{\pm,0,-,k}$. We then have

$$\begin{aligned} S_k(\omega) &= \frac{1}{2\pi}\int dt e^{-\omega t} \langle \mathbf{S}_k \cdot \mathbf{S}_k(t) \rangle &(5.31)\\ &= \frac{1}{2\pi}\int dt \sum_j e^{(\omega_j-\omega)t} |\langle \sum_\alpha S^\alpha_k | \hat{\Theta}^\dagger_{\pm,k} \rangle|^2 &(5.32)\\ &\approx \frac{1}{2\pi}\int dt \sum_j e^{(\omega_j-\omega)t} |\langle \sum_\alpha S^\alpha_q | \hat{\Theta}^\dagger_{\pm,k} \rangle|^2 &(5.33) \end{aligned}$$

Here the expectation value in the first line is taken with respect to the ground state. The inner product evaluates to

$$|\langle \sum_\alpha S_q^\alpha | \hat{\Theta}^\dagger_{\pm,k}\rangle|^2 = \begin{cases} \hat{\Theta}^\dagger_{+,k}: & |-2e^{i\phi/2}\cos(\phi_k/2+\Delta\phi)|^2 = 4\cos^2(\phi_k/2+\Delta\phi) \\ \hat{\Theta}^\dagger_{-,k}: & |-2ie^{i\phi/2}\sin(\phi_k/2+\Delta\phi)|^2 = 4\sin^2(\phi_k/2+\Delta\phi). \end{cases} \tag{5.34}$$

The spin structure factor depends on the angle ϕ_k, which is the complex angle of $m_{j,k}$. In addition, one must take care to add an angle $\Delta\phi$, depending on which lattice vector is chosen. This is shown in figure 5.4. We already know by symmetry that ϕ_k must wind twice around the Γ-point. The above result shows that there will be two intensity minima on a circle around Γ and two maxima. This is exactly what the half-moon features commonly observed in neutron scattering spectra look like.

This calculation can be repeated at K and K' points. If this is done the same expression for $S_k(\omega)$ is obtained. The phase that must be added at each K and K' point is indicated in figure 5.4. On this figure we also indicate which of the basis functions must be picked for $\hat{\Theta}^\dagger_{\pm,p,q,k}$ at each high-symmetry point.

In figure 5.5 results from spin-wave theory are shown. We calculate the structure factor at constant energy cuts. This allows us to resolve the half-moon features both near the Γ-point and the K and K' points. The $q = \Delta_1$ lattice vector was chosen for the (a) and (b) subfigures. We have also superimposed the winding pattern of figure 5.3.

5.6 Topological phases caused by Kitaev-like anisotropy

In addition to the well-known result that the DM interaction causes topological magnon bands [10, 104], band-topology may also be altered by Kitaev-like parity even anisotropic interaction [160]. We here refer to the J_- term of equation (5.6).

Since we have shown that there must be a winding of $\mathbf{d}_k$ around the high-symmetry points, as long as there is a finite perturbation that can lift the degeneracy exactly at those points, then the band-gap must be accompanied by Chern numbers. Even parity anisotropic interaction breaks the $U(1)$ symmetry of the otherwise $\hat{S}^z$ conserving model. This results in pairing terms, which must be treated by a Bogoliubov transform which results in a gap.

We refer back to equation (5.6), which defines the most general nearest neighbor exchange Hamiltonian allowed by the D_{6h} point group.

$$\hat{H} = \sum_{\langle i,j\rangle} \mathbf{S}_i \boldsymbol{J}_{i,j} \mathbf{S}_j - h^z \sum_i \hat{S}_i. \tag{5.35}$$

Following the procedure outlined in Chapter 2, we derive a BdG Hamiltonian

$$\hat{H}^{\mathrm{BdG}}_k = \mathbf{v}_k^\dagger \begin{bmatrix} \boldsymbol{M}_k & \boldsymbol{N}_k \\ \boldsymbol{N}_k^\dagger & \boldsymbol{M}_k^* \end{bmatrix} \mathbf{v}_k. \tag{5.36}$$

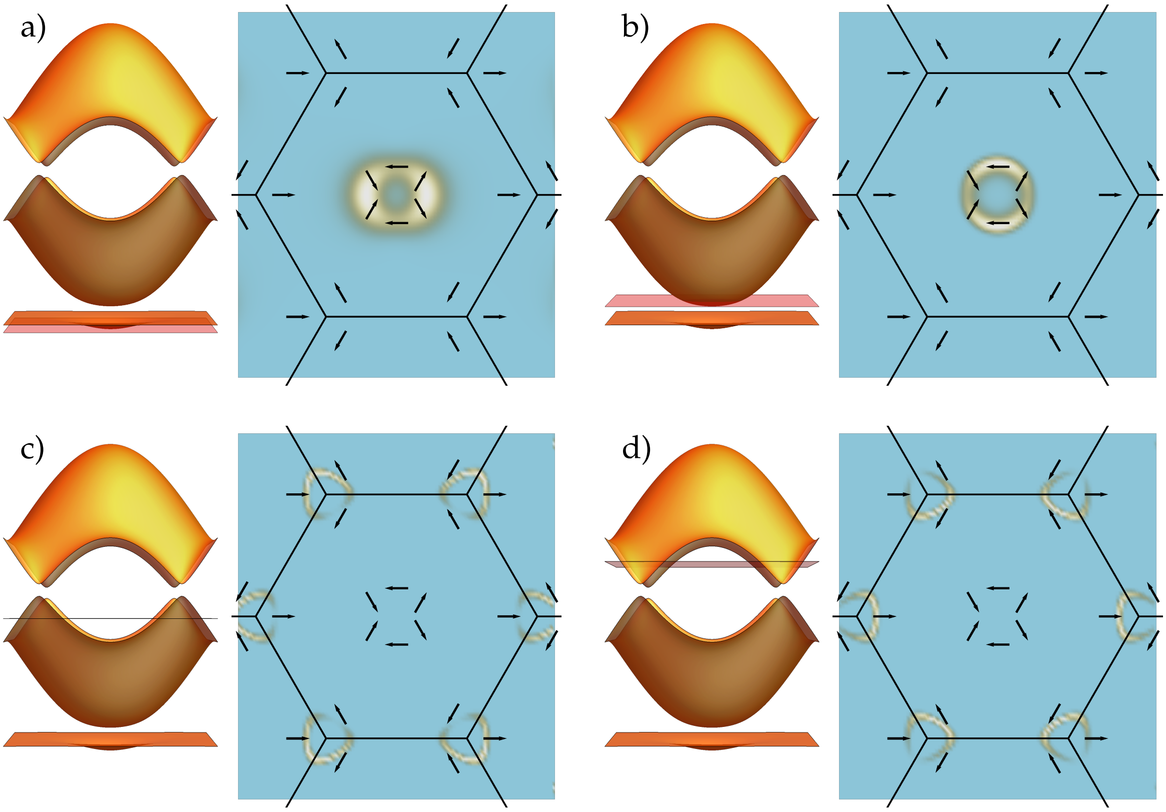

Figure 5.5: We here plot the topological magnon bands with the structure factor calculated through constant energy cuts for $J_x = J_y = J_z = 1$, $D_z = 0.1$. A transparent flat surface shown alongside the bands shows the energy that the structure factor is being calculated at. (a) the energy cut is taken just below the bottom band. There is here a half-moon feature consistent with the double-winding expected at the Γ-point. (b) here the energy cut is taken just above the band-gap. Again a half-moon feature is visible, but the intensity minima and maxima have swapped. (c) at higher energies the effective field winds only once around each K and K' point. This is visible as the intensity only has one minimum and maximum. (d) the intensity minima and maxima swap when we move to the upper band.

Here

$$\boldsymbol{M}_k = \begin{bmatrix} h/2 - J_z & -iD_z/2 + J_+/2\cos[\delta_3 \cdot k] & iD_z/2 + J_+/2\cos[\delta_2 \cdot k] \\ iD_z/2 + J_+/2\cos[\delta_3 \cdot k] & h/2 - J_z & -iD_z/2 + J_+/2\cos[\delta_1 \cdot k] \\ -iD_z/2 + J_+/2\cos[\delta_2 \cdot k] & iD_z/2 + J_+/2\cos[\delta_1 \cdot k] & h/2 - J_z \end{bmatrix} \tag{5.37}$$

and

$$\boldsymbol{N}_k = \begin{bmatrix} 0 & J_-/2\cos[\delta_3 \cdot k] & \omega J_-/2\cos[\delta_2 \cdot k] \\ J_-/2\cos[\delta_3 \cdot k] & 0 & \omega^* J_-/2\cos[\delta_1 \cdot k] \\ \omega^* J_-/2\cos[\delta_2 \cdot k] & \omega J_-/2\cos[\delta_1 \cdot k] & 0 \end{bmatrix}. \tag{5.38}$$

Here

$$J_+ = (J_x + J_y)/2 \tag{5.39}$$

$$J_- = (J_x - J_y)/2 \tag{5.40}$$

and once again

$$\omega = -1/2 + i\sqrt{3}/2. \tag{5.41}$$

To obtain the correct eigenstates, this must be diagonalized via a generalized Bogoliubov transform as outlined in Section 2.2.2. Doing so allows us to derive the exact energies at the high-symmetry points.

At the Γ-point $\hat{\Psi}^\dagger_{0,k}$ and $\hat{\Psi}^\dagger_{-,k}$ are gapped due to J_- and D_z. Their band-energies are

$$\epsilon^0_\Gamma = \frac{-3}{2}J_+ - \frac{\sqrt{3}}{2}D_z + 2\sqrt{\left(\frac{h}{2} - J_z + \frac{J_+}{4} - \frac{\sqrt{3}}{4}D_z\right)^2 - \frac{{J_-}^2}{4}} \tag{5.42}$$

$$\epsilon^-_\Gamma = \sqrt{\left(\frac{h}{2} - J_z - \frac{J_+}{2} + \frac{\sqrt{3}}{2}D_z\right)^2 - {J_-}^2}. \tag{5.43}$$

At the K-point it is the higher energy $\hat{\Psi}^\dagger_{+,k}$ and $\hat{\Psi}^\dagger_{-,k}$ which are gapped due to J_- and D_z. Their band-energies are

$$\epsilon^-_K = \frac{3}{4}J_+ + \frac{\sqrt{3}}{4}D_z + 2\sqrt{\left(\frac{h}{2} - J_z - \frac{J_+}{8} + \frac{\sqrt{3}}{8}D_z\right)^2 - \frac{{J_-}^2}{16}} \tag{5.44}$$

$$\epsilon^+_K = \sqrt{\left(\frac{h}{2} - J_z + \frac{J_+}{4} - \frac{\sqrt{3}}{4}D_z\right)^2 - \frac{{J_-}^2}{4}}. \tag{5.45}$$

At K' the gapped bands are $\hat{\Psi}^\dagger_{+,k}$ and $\hat{\Psi}^\dagger_{0,k}$. Their band-gap is identical to the one at K.

Each of these sets of equations define curves in parameter-space where the band-gaps close. Thus by drawing up the regions and calculating Chern numbers in each case we are able to construct the phase diagram of figure 5.6. This phase-diagram

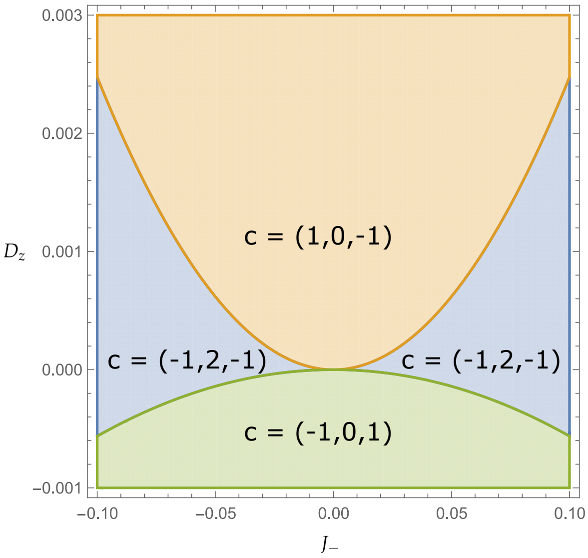

Figure 5.6: We here show the Chern numbers obtained for different sets of parameters J_- (first axis) and D_z (second axis). There are three distinct topological phases obtainable by tuning the DM interaction and the Kitaev anisotropy. The phases are labeled by their Chern numbers. It is worthwhile noting that the axis are scaled so that the DM interaction is almost two orders of magnitude lower than the Kitaev anisotropy.

shows 3 distinct phases as categorized by Chern numbers, which are labeled in order of ascending band-energy. There are two phases which are caused by DM interaction, and they have opposite Chern numbers. The phase caused by J_- is characterized only by one set of Chern numbers, both when J_- is positive and negative. Note also that the axes of the phase-diagram are not equal. The range of J_- is more than an order of magnitude larger than that of D_z.

5.7 Conclusions

In this chapter we started by considering the $D_{6h}(C_{6h})$ magnetic point group and the representations of magnons under this group. We arrived at a representation theory that allowed us to describe magnon basis functions of the kagome lattice.

By writing the spin-wave Hamiltonian in this basis we were able to show how $D_{6h}(C_{6h})$ imposes constraints on the Hamiltonian in k-space. These constraints result in the appearance of a characteristic winding of $[d_1(\mathbf{k}), d_2(\mathbf{k})]$ near the high symmetry points. Due to this winding the bands are endowed with a Berry curvature as well as easily distinguishable half-moon features in $S_k(\omega)$. These findings are supported by spin-wave calculations where DM and Kitaev-like anisotropies have been taken into account.

It is remarkable that these features arise directly from symmetry considerations. Our results suggest a connection between band-topology and halft-moon features in $S_k(\omega)$. This connection becomes clear when the effective two-band model of a band-touching is considered with the constraints imposed by symmetry. A natural open question is then how general this result is and whether it applies to spectral features in other magnetic materials.

While preparing the final draft of this thesis, it has come to our attention that another study on magnon representation theory and its consequence for band topology has been published in the preprint [161]. Here the spin-space groups are introduced which are used to discuss symmetry enforced degeneracies in the magnon band structure. Upon introduction of spin-orbit terms, the spin-space and real-space groups cannot be treated seperately and here the spin-space groups are isomorphic to magnetic space-groups. Although this has similarities with our work, the model studied here is a honeycomb lattice model. The authors show that the bands potentially have Berry curvature and must be gapped as a consequence of the spin-space group representations. In our study we go beyond this by examining the winding feature of **d** enforced by symmetry as well as the topology this causes. Furthermore we establish a link between this and the spin structure factor.

Chapter 6

Summary and conclusions

In this thesis we addressed aspects of topology in band-like excitations in magnets. There are certain invariants that can be associated with these as well as experimental signatures. Our main discussions have been about the $\mathcal{Z}_2$ topological phase of bilayer $S = 1/2$ kagome, as well as the connection between the spin-spin structure factor and Chern numbers in kagome magnon bands.

Previous studies on these topics have concluded that magnetic insulators exhibit topologically non-trivial magnon bands. Studies of the thermal Hall effect of magnons by Katsura et. al. [33] showed that a formula for the thermal Hall coefficient could be derived which is analogous to the TKNN formula. This famous work shows that the heat current mediated by magnons, should have an associated transverse component which depends on the Berry curvature. This was used to calculate the thermal Hall coefficient in a kagome lattice [10] in order to shed light on Onose's famous $Lu_2V_2O_7$ experiments [9]. In connection to this, additional work on topologically non-trivial band-structures in kagome was undertaken [104] to clarify the existence of topological magnon edge-states.

Unlike the electronic quantized Hall current, the response found in magnetic band-structures is weighted thermally by a Bose distribution. The topology of the magnon bands could therefore in principle be trivial even when a finite thermal Hall effect is observed. This naturally merits the question, do more direct signatures of band topology exist in magnets? and are there ways to infer the magnon band-topology from symmetry? These are the main questions we set out to address in our study on the symmetry origins of half-moons in $S_k(\omega)$ of the spin-polarized phase of kagome.

Inspired by the discovery of the $\mathcal{Z}_2$ topological phase in electronic band theory, notable papers have been published which investigated similar phenomena in magnets. Joshi et. al. introduced the triplet bond-wave Hamiltonian of the bilayer honeycomb lattice [130] in which it was stated that triplons should enjoy a similar protection mechanism as degenerate Krämer's pairs in electronic band theory.

However, the proper formulation of a pseudo-time-reversal operator for magnons was treated in a separate publication by Kondo et. al. [13], where the protection mechanism is much more carefully introduced and explained. Using the pseudo-time-reversal operator defined in [13], it is possible to give a much more rigorous treatment of the $\mathcal{Z}_2$ topological phase in a wide range of bilayer $S = 1/2$ lattices.

What conclusions can we draw about the $\mathcal{Z}_2$ phase in bilayer models involving triplon excitations based on the PTR protection mechanism? In this thesis we set out to answer this question using the PTR symmetry.

6.1 $\mathcal{Z}_2$ topology and pseudo-time-reversal

The theoretical investigation of the pseudo-time-reversal (PTR) symmetry for bilayer magnetic insulators [13] has inspired questions to further the understanding of what conditions are needed for a $\mathcal{Z}_2$ band topology in a magnetic insulator. We explored this question in great depth focusing on the bilayer kagome lattice with triplet excitations.

The role of PTR symmetry is to protect the $\mathcal{Z}_2$ from being broken except by very large perturbations. It is therefore an interesting question whether it appears also in bands of magnetic excitations. We found in our study that it indeed has no physical origin in the bilayer kagome lattice.

There are at least two ways that this can be shown, and we have done both. One is by including those interactions that are allowed by lattice and global symmetries and explicitly showing that some of them break PTR symmetry. We did so, and we found that the bond-nematic interaction, which we describe in detail, breaks PTR symmetry. The other method, which we also used, is to show explicitly that these interactions cause the helical triplon edge-modes to hybridize.

The question then remains, how exactly is PTR symmetry realized in magnetic insulators, and is there even a sense in which it is possible for a system of bosonic excitations? This question arises primarily because bosons do not automatically form Krämer's pairs under time reversal, in contrast to fermions. Some additional mechanism is needed for bosonic pseudo-Krämer's degeneracy to arise, which would endow the excitations with the same protection properties. We found that what is needed here is a $U(1)$ symmetry in combination with TR.

It is an open question which systems possess such symmetries. However, perhaps there are ways that they can be generated. An example could be through magnetic point groups. When a material orders magnetically, its symmetry may be lowered in such a way that TR is no longer a symmetry of the system. However, TR in combination with lattice symmetries, such as reflection, may still be. There are certain cases where these can be represented by a $U(1)$ phase rotation together with complex conjugation. This may be a promising direction to look.

6.2 Half-moons and Chern numbers in kagome lattice

In the spin-polarized phase of the kagome anti-ferromagnet, we were able to show that there is a concrete connection between magnon band topology and the spin-spin structure factor. The approach we took was to derive representations of the magnetic point group on the space of magnon basis functions. In doing so we were able to derive the relationship between matrix elements of the Hamiltonian in different parts of k-space.

Around the high symmetry points in the lattice, these rules predict winding features which are indicative of topological bands. Furthermore, these same rules predict features in the structure factor which are directly compatible with half-moon features seen in experiments.

Does this mean that half-moons in a more general context predict topological bands? This is an interesting open question. In the kagome lattice, which we studied, the winding feature in $S_k(\omega)$ comes from the mixing of basis functions, which at high symmetry points are exact eigenstates of the Hamiltonian. This same winding is what makes the band-topology non-trivial.

Here we used the basis functions of a magnetic point-group to prove the connection between the two in a very specific case. Doing so for general magnetic excitations may not be easy. Not least because of the variety of magnetic order. Additionally, we have here only described single-magnon bands. The situation could be further complicated by interaction with other magnons, and we have not treated such matrix elements.

But perhaps there are other applications. An interesting implication of our work is that by placing constraints on the Fourier transformed $\hat{H}(k)$ without writing out the concrete form of the real-space Hamiltonian, we make no restrictions about the range of interactions. They could be nearest-neighbor, next-nearest and so on. This potentially offers a different approach to investigating quite general symmetry allowed spin-wave Hamiltonians. On a broader level it could be generalized to also describe bond-wave or other types of magnetic excitations.

Appendix A

Magnetic point groups

Group theory is a topic with very wide applicability in physics. In many cases, the laws governing particle dynamics are the consequence of some symmetry in nature. This is the case in particle physics certainly, but there are also profound new laws that can be discovered and applied only to interacting particles.

In this section we will briefly list the definitions of group theory. This will then allow us to introduce the point group C_{3v}, which describes for instance the kagome (without site centered inversion) and triangular lattice. We then discuss how the symmetry is lowered during spontaneous ordering and how this leads to the appearance of a magnetic point group $C_{3v}(C_3)$. For a good reference, which discusses all of this in great detail, please see any one of [162–164].

A.1 definitions

A group is a collection G of elements $g \in G$ with a product $\otimes$. It obeys the following conditions.

1. The product of any two elements of the group is itself an element of the group.
2. $\otimes$ is associative, that is $g_a \otimes (g_b \otimes g_c) = (g_a \otimes g_b) \otimes g_c$.
3. There exists an identity element $e \in G$ such that $e \otimes g = g \otimes e = g$ for any $g \in G$.
4. For any $g \in G$ there exists an inverse element g^{-1} such that $gg^{-1} = g^{-1}g = e$.

An example of a continuous group is the set of real numbers $\mathcal{R}$ under the operation of addition $+$. Clearly the sum of any two real numbers is a real number. Addition is an associative operator, and the identity element is 0. Each real number also has an inverse element obtained by changing the sign of that number.

As an example of a discrete group, consider the symmetry operations on the triangle. The group is then

$$C_{3v} = \{e, c_3, {c_3}^2, \sigma_1, \sigma_2, \sigma_3\}. \tag{A.1}$$

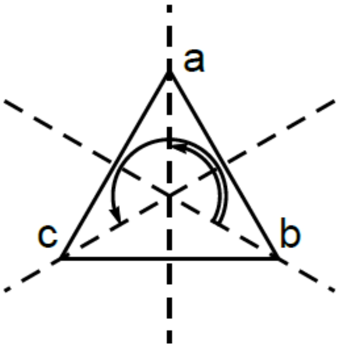

Figure A.1: Here the symmetry operations of C_{3v} are depicted on the triangle. The triangle is invariant to the planes of reflection and rotations of this group.

Here c_3 is a 120° rotation in the x, y-plane. $c_3{}^2$ is just the same rotation applied twice. The σ_i elements are reflections. σ_1 is a reflection through the y, z-plane, and the two other planes of reflection can be constructed by rotating the plane of reflection. $\sigma_2 = c_3\sigma_1$ and $\sigma_3 = c_3{}^2\sigma_1$ (see figure A.1).

To be more concrete we can consider the effect of those operations on a vector in the plane. A set of matrices that does this for us shown on table A.1

Table A.1: The point group c_{3v} represented by its action on a 3 component coordinate space $\vec{R} = [x, y, z]^T$.

g	e	c_3	$c_3{}^2$
$M_{\mathbf{R}}(g)$	$\begin{bmatrix} 1 & 0 & 0 \\ 0 & 1 & 0 \\ 0 & 0 & 1 \end{bmatrix}$	$\begin{bmatrix} -1/2 & -\sqrt{3}/2 & 0 \\ \sqrt{3}/2 & -1/2 & 0 \\ 0 & 0 & 1 \end{bmatrix}$	$\begin{bmatrix} -1/2 & \sqrt{3}/2 & 0 \\ -\sqrt{3}/2 & -1/2 & 0 \\ 0 & 0 & 1 \end{bmatrix}$
g	σ_1	σ_2	σ_3
$M_{\mathbf{R}}(g)$	$\begin{bmatrix} -1 & 0 & 0 \\ 0 & 1 & 0 \\ 0 & 0 & 1 \end{bmatrix}$	$\begin{bmatrix} 1/2 & -\sqrt{3}/2 & 0 \\ -\sqrt{3}/2 & -1/2 & 0 \\ 0 & 0 & 1 \end{bmatrix}$	$\begin{bmatrix} 1/2 & \sqrt{3}/2 & 0 \\ \sqrt{3}/2 & -1/2 & 0 \\ 0 & 0 & 1 \end{bmatrix}$

This is one possible *matrix representation* of C_{3v}. By showing how it acts on an arbitrary coordinate vector $\vec{R} = [x, y, z]^T$, we now have a construction where each group element is a matrix. It may be checked very easily that under matrix multiplication this representation obeys all of the rules that a group should.

We notice however, that the z-coordinate is left invariant under this group, regardless of which operation is being applied to it. It is therefore possible to write a representation of C_{3v} applied to z separate to the 2×2 matrix representation of C_{3v} applied to the $[x, y]^T$ vector.

This is an example of an *irreducible representation*. In the case of C_{3v} there are 3 irreducible representations, which we tabulate as

Here the two-dimensional point group E describe how the coordinates x and y transform into one-another. We say they are partners under this point group. z is an example of a basis function, which transforms according to the irrep $A1$.

Table A.2: The irreducible representations of the point group C_{3v}.

g	e	c_3	${c_3}^2$	σ_1	σ_2	σ_3
$\Gamma^{A1}(g)$	1	1	1	1	1	1
$\Gamma^{A2}(g)$	1	1	1	-1	-1	-1
$\Gamma^{E}(g)$	$\begin{bmatrix} 1 & 0 \\ 0 & 1 \end{bmatrix}$	$\begin{bmatrix} -\frac{1}{2} & -\frac{\sqrt{3}}{2} \\ \frac{\sqrt{3}}{2} & -\frac{1}{2} \end{bmatrix}$	$\begin{bmatrix} -\frac{1}{2} & \frac{\sqrt{3}}{2} \\ -\frac{\sqrt{3}}{2} & -\frac{1}{2} \end{bmatrix}$	$\begin{bmatrix} -1 & 0 \\ 0 & 1 \end{bmatrix}$	$\begin{bmatrix} \frac{1}{2} & -\frac{\sqrt{3}}{2} \\ -\frac{\sqrt{3}}{2} & -\frac{1}{2} \end{bmatrix}$	$\begin{bmatrix} \frac{1}{2} & \frac{\sqrt{3}}{2} \\ \frac{\sqrt{3}}{2} & -\frac{1}{2} \end{bmatrix}$

Now, we can look at how a different class of objects transform. We can start by defining the angular momentum operator

$$L^z = xv_y - yv_x. \tag{A.2}$$

Realizing that v_x and v_y are partners under this group according to E, in the same way as x and y are partners, simply substituting in the transformation rules allows one to show that L^z transforms according to $A2$. To see this, we can take

$$\begin{aligned} c_3 : xv_y &\rightarrow (-x/2 + y\sqrt{3}/2)(-v_y/2 - v_x\sqrt{3}/2) \qquad (A.3) \\ &= xv_y/4 - yv_x 3/4 + xv_x\sqrt{3}/4 - yv_y\sqrt{3}/4, \qquad (A.4) \end{aligned}$$

as well as

$$\begin{aligned} c_3 : yv_x &\rightarrow (-y/2 - x\sqrt{3}/2)(-v_x/2 + v_y\sqrt{3}/2) \qquad (A.5) \\ &= yv_x/4 - xv_y 3/4 - yv_y\sqrt{3}/4 + xv_x\sqrt{3}/4. \qquad (A.6) \end{aligned}$$

Taking the difference between these terms, we see that

$$c_3 : L^z = L^z. \tag{A.7}$$

We also have

$$\sigma_1 : xv_y \rightarrow -xv_y \tag{A.8}$$

and

$$\sigma_1 : yv_x \rightarrow -yv_x. \tag{A.9}$$

Which gives

$$\sigma_1 : L^z = -L^z. \tag{A.10}$$

This together with the group algebra shows that L^z transforms according to $A2$.

The common intuition one has of angular momentum is of a vector oriented in the direction perpendicular to the plane in which the given object is spinning or rotating. If we instead of imagining an angular momentum vector we think of a vortex-like current lying in this plane encircling the origin, we can intuitively see that vertical reflections through the origin should reverse this current and thus reverse L^z. This is an example of an axial vector.

As it happens, spins too are axial vectors. If we write up the matrix representation of C_{3v} acting on a spin we find

Table A.3: The point group C_{3v} represented by its action on a 3 component spin space with $\hat{S}^z$ orthogonal to the plane.

g	e	c_3	${c_3}^2$
$M_{\mathbf{S}}(g)$	$\begin{bmatrix}1 & 0 & 0\\0 & 1 & 0\\0 & 0 & 1\end{bmatrix}$	$\begin{bmatrix}-1/2 & -\sqrt{3}/2 & 0\\\sqrt{3}/2 & -1/2 & 0\\0 & 0 & 1\end{bmatrix}$	$\begin{bmatrix}-1/2 & \sqrt{3}/2 & 0\\-\sqrt{3}/2 & -1/2 & 0\\0 & 0 & 1\end{bmatrix}$
g	σ_1	σ_2	σ_3
$M_{\mathbf{S}}(g)$	$\begin{bmatrix}1 & 0 & 0\\0 & -1 & 0\\0 & 0 & -1\end{bmatrix}$	$\begin{bmatrix}-1/2 & \sqrt{3}/2 & 0\\\sqrt{3}/2 & 1/2 & 0\\0 & 0 & -1\end{bmatrix}$	$\begin{bmatrix}-1/2 & -\sqrt{3}/2 & 0\\-\sqrt{3}/2 & 1/2 & 0\\0 & 0 & -1\end{bmatrix}$

We see that S^z is a basis function transforming according to $A2$ whereas S^x and S^y transform according to the E irrep as partners. Although it isn't written in the same way as in table A.2, this is a result of the chosen basis. If we replace $\hat{S}^x \to \hat{S}^y$, and $\hat{S}^y \to -\hat{S}^x$, then the result will be the same.

There is a fundamental symmetry in nature we have not yet discussed. Angular momenta are not time-reversal invariant, which complicates some of the symmetry analysis involved since reversing the arrow of time reverses each spin. This is highly relevant in studying spontaneous magnetic order.

A.2 Spontaneous magnetic order and magnetic point groups

Magnetic insulators unless under some applied field are time-reversal symmetric at high temperatures. Apart from the point group which is dictated by the structure of the material, they also have time-reversal as a symmetry element. Thus we may write up the symmetry group describing for instance a kagome lattice as

$$G_\Delta = \tau \otimes C_{3v}. \tag{A.11}$$

At temperatures where the material is a paramagnet, the system transforms trivially according to this point group. In the space of the spin-configuration of the entire lattice, each symmetry operation, including time-reversal, acts as the identity element.

As the material is cooled down, spontaneous order sets in. This occurs because the favourable low-energy states of the material are very far from each other in phase space. The ground states no longer transform trivially, but instead transform according to one of the irreps of the point group.

When the kagome lattice orders, it does so in a number of ways each corresponding to an irreducible representation of G_Δ [159, 165]. For now we will consider the ferromagnetic state in which all spins are aligned. The total symmetry group acting on this state can now be represented as

In this example we see that there is a subgroup of G_Δ with respect to which this

Table A.4: Action of the group $\tau \otimes C_{3v}$ on the ferromagnetic state.

g	e	c_3	${c_3}^2$	σ_1	σ_2	σ_3	τ	τc_3	$\tau {c_3}^2$	$\tau\sigma_1$	$\tau\sigma_2$	$\tau\sigma_3$
$\Gamma(g)$	1	1	1	-1	-1	-1	-1	-1	-1	1	1	1

state is invariant. This is the group

$$C_{3v}(C_3) = C_3 \oplus \tau \times C_{3v} \backslash C_3. \tag{A.12}$$

This is an example of a magnetic point group, a type of point group which describes the symmetries of magnetically ordered states. They are constructed from a regular point group in the following way. First the invariant subgroup of the ordered material is identified (in this case C_3). The rest of the regular point group is combined with time-reversal and the union of those to sets are taken. In the above example this results in the magnetic point group $C_{3v}(C_3)$, which is isomorphic to C_{3v}, but still is able to describe magnetically ordered kagome.

Appendix B

Topological Charge

In Chapter 3 we stated the equation for the Berry phase as

$$\gamma_{\pm} = \iint_S \mathbf{F}_{\pm} \cdot \hat{n}(d_{S,1}, d_{S,2}) dS. \tag{B.1}$$

Here $\mathbf{F}_{\pm}$ has the elements

$$F_{\pm,i} = \epsilon_{ijk} \partial_{d_j} \langle \psi_{\pm} | \partial_{d_k} | \psi_{\pm} \rangle . \tag{B.2}$$

This can be shown in the following way. The Berry curvature is

$$\begin{aligned} F_{\pm} &= \partial_\theta \langle \psi_{\pm} | \partial_\phi | \psi_{\pm} \rangle - \partial_\phi \langle \psi_{\pm} | \partial_\theta | \psi_{\pm} \rangle & \text{(B.3)} \\ &= \sum_{i,j} \Big(\frac{\partial d_i}{\partial \theta} \frac{\partial d_j}{\partial \phi} - \frac{\partial d_i}{\partial \phi} \frac{\partial d_j}{\partial \theta} \Big) \partial_{d_i} \langle \psi_{\pm} | \partial_{d_j} | \psi_{\pm} \rangle & \text{(B.4)} \\ &= \sum_i \det(J_i) F_{\pm,i}. & \text{(B.5)} \end{aligned}$$

Here each pairwise combination of d_i and d_j define a Jacobian

$$J_1 = \begin{bmatrix} \frac{\partial d_2}{\partial \theta} & \frac{\partial d_2}{\partial \phi} \\ \frac{\partial d_3}{\partial \theta} & \frac{\partial d_3}{\partial \phi} \end{bmatrix}, \tag{B.6}$$

and so on for J_2 and J_3. Returning to the parameterization of $\mathbf{d}$ from Chapter 3 with

$$\begin{aligned} d_1 &= d_0 \sin\theta \cos\phi \\ d_2 &= d_0 \sin\theta \sin\phi . \\ d_3 &= d_0 \cos\theta \end{aligned} \tag{B.7}$$

Then

$$F_{\pm} = \sin\theta \mathbf{n} \cdot \mathbf{F}_{\pm} {d_0}^2. \tag{B.8}$$

The unit vector $\mathbf{n}$ is $\mathbf{d}/d_0$.

We can therefore write the Berry phase as

$$\gamma_{\pm} = \iint F_{\pm} d\theta d\phi \tag{B.9}$$

$$= \iint \mathbf{F}_{\pm} \cdot \mathbf{n} \sin\theta {d_0}^2 d\theta d\phi \tag{B.10}$$

$$= \iint \mathbf{F}_{\pm} \cdot \mathbf{n} dA \tag{B.11}$$

$$= \iint \mathbf{F}_{\pm} d\mathbf{S}. \tag{B.12}$$

In the last equality we have gone from the area element of the sphere of radius d_0 to that of the general surface S with normal vector $\hat{n}$.

B.1 Generic cases

We can first imagine that the Hamiltonian is periodic in the parameters $\mathbf{x}$. Equivalently, then $\vec{d}$ must be periodic in $\mathbf{x}$ and $\theta(\mathbf{x}), \phi(\mathbf{x})$ must necessarily be as well. There are some cases which are now of interest. We can imagine a trivial one first, in which $\theta = 0$ and $\phi(\mathbf{x})$ changes from 0 to 2π. Here the Berry curvature is a constant 0 and therefore the Berry phase too evaluates to 0 upon integration.

We can imagine this being the case if we have some symmetry in our system which takes $\boldsymbol{\sigma}_z \to -\boldsymbol{\sigma}_z$. This would ensure that there is no third component of the $\mathbf{d}$-vector. For the sake of argument, we can imagine that

$$\vec{d} = [\sin x_1 k_1, \sin x_2 k_2, 0]^T. \tag{B.13}$$

Now let us imagine a finite perturbation

$$H' = \delta(1 + \cos(x_1 k_1)\cos(x_2 k_2))\boldsymbol{\sigma}_z \tag{B.14}$$

which breaks this symmetry. At the edges defined by $x_1 k_1 = \pm\pi$ or $x_2 k_2 = \pm\pi$, $\vec{d}$ is still constrained to lie on a circle. In a real physical system this constraint could come about as the result of an applied uniform field. In this case we have

$$\gamma_{\pm} = \pm \iint \frac{\sin(\theta)}{2} d\theta d\phi \tag{B.15}$$

$$= \pm\frac{1}{2} \oint d\phi. \tag{B.16}$$

The value of the last integral depends on how many times the angle ϕ winds around the equator of the Bloch sphere, which again depends on its parametrization with regards to parameters $\mathbf{x}$. Here we will define the winding integer n, such that

$$\gamma_{\pm} = \pm\pi n. \tag{B.17}$$

So, in this case taking the adiabatic evolution through a closed path in the space of parameters **x** results in a Berry phase of $\pm\pi$. The intuition is that due to the symmetry breaking term $\delta\boldsymbol{\sigma}_z$, the northern hemisphere of the Bloch sphere is covered a number of times which depends on the winding number.

If on the other hand we add a perturbation

$$H' = \delta\cos(x_1k_1)\cos(x_2k_2)\boldsymbol{\sigma}_z \tag{B.18}$$

we will obtain the result

$$\gamma_{\pm} = \pm 2\pi n. \tag{B.19}$$

This is analogous to Gauss' law. Whenever we have an enclosed surface and we calculate the flux through it we can associate it with an enclosed charge. With open surfaces we cannot define an enclosed charge, but we may still have a finite Berry curvature. As in the previous case where **d** forms a half-sphere.

Appendix C

Bogoliubov de Gennes basis-functions

Our treatment of the magnon wave-function ultimately results in a set of rules for matrix elements which mix the basis functions near the high symmetry points of the Brillouin zone, which we will elaborate on in the next section. However, these basis functions may in general be obtained by a Bogoliubov transform which results in bosons that have a Hermitian conjugate component added to their wave-function. We show here how to construct these wave-functions so that they still transform according to the irreps we outlined above.

We briefly restate that the general eigenstate of a BdG Hamiltonian is obtained through a Bogoliubov transform (see Section 2.2.2). In general there may be non-pairing terms, which require eigenstates of the form

$$\hat{\Psi}_k^\dagger = \alpha_{a,k}\hat{a}_k^\dagger + \ldots + \alpha_{c,k}\hat{c}_k^\dagger + \beta_{a,k}\hat{a}_{-k} + \ldots + \beta_{c,k}\hat{c}_{-k}. \tag{C.1}$$

Requiring $\Psi_k^\dagger$ to be bosonic then leads to the normalization requirement

$$\sum_i |\alpha_{i,k}|^2 - |\beta_{i,k}|^2 = 1. \tag{C.2}$$

At the high symmetry points, we require that $\Psi_k^\dagger$ transforms according to the irreps we have written. We rewrite the basis functions as the more general

$$\hat{\Psi}_{j,k}^\dagger = \alpha_{j,k}\hat{\psi}_{j,k}^\dagger + \beta_{j,k}\hat{\phi}_{j,-k}. \tag{C.3}$$

Now the index $j = 0, +, -$ specifies which irrep $\hat{\Psi}_{j,0}^\dagger$ transforms as. The choice of $\alpha_{j,k}$ and $\beta_{j,k}$ will usually be such that $\hat{\Psi}_{j,0}^\dagger$, $\hat{\Psi}_{j,K}^\dagger$ and $\hat{\Psi}_{j,K'}^\dagger$ are eigenstates. In general the above construction does not yield eigenstates at arbitrary k, but it allows us to define a symmetrical basis in the same way as equation (5.13). At Γ we now have

$$\hat{\Psi}_{j,0}^\dagger = \alpha_{j,0}\hat{\psi}_{j,0}^\dagger + \beta_{j,0}\hat{\phi}_{j,0}. \tag{C.4}$$

Now we can take some $g \in D_{6h}(C_{6h})$ and

$$g : \hat{\Psi}_{j,0}^\dagger = \Gamma^j(g)(\alpha_{j,0}\hat{\psi}_{j,0}^\dagger) + (g : \beta_{j,0}\hat{\phi}_{j,0}). \tag{C.5}$$

If $\hat{\Upsilon}^\dagger_{j,0}$ is to transform according to Γ^j, then evidently so must $\hat{\phi}^\dagger_{j,0}$. However, while the magnon creation operator transforms as $\hat{S}^-$ as we noted, the annihilation operator transforms as $\hat{S}^+$. Because of this, we find the basis functions

$$\begin{aligned}\hat{\phi}_{0,0} &= \hat{\psi}_{0,0} = (\hat{a} + \omega\hat{b} + \omega^*\hat{c})\\ \hat{\phi}_{+,0} &= \hat{\psi}_{-,0} = (\hat{a} + \omega^*\hat{b} + \omega\hat{c})\\ \hat{\phi}_{-,0} &= \hat{\psi}_{+,0} = (\hat{a} + \hat{b} + \hat{c}).\end{aligned} \tag{C.6}$$

This results in

$$\begin{aligned}\hat{\Upsilon}^\dagger_{0,0} &= \alpha_k\hat{\psi}^\dagger_{0,0} + \beta_k\hat{\psi}_{0,0}\\ \hat{\Upsilon}^\dagger_{+,0} &= \alpha_k\hat{\psi}^\dagger_{+,0} + \beta_k\hat{\psi}_{-,0}\\ \hat{\Upsilon}^\dagger_{-,0} &= \alpha_k\hat{\psi}^\dagger_{-,0} + \beta_k\hat{\psi}_{+,0}.\end{aligned} \tag{C.7}$$

The derivation can be repeated for the K, K' points with the sub-group $C_{3v}(C_3)$ which yields

$$\begin{aligned}\hat{\Upsilon}^\dagger_{0,K} &= \alpha_k\hat{\psi}^\dagger_{0,K} + \beta_k\hat{\psi}_{0,K'}\\ \hat{\Upsilon}^\dagger_{+,K} &= \alpha_k\hat{\psi}^\dagger_{+,K} + \beta_k\hat{\psi}_{-,K'}\\ \hat{\Upsilon}^\dagger_{-,K} &= \alpha_k\hat{\psi}^\dagger_{-,K} + \beta_k\hat{\psi}_{+,K'}.\end{aligned} \tag{C.8}$$

In the case of a BdG Hamiltonian, one may pick $\alpha_{j,k}$ and $\beta_{j,k}$ in such a way that the pairing terms are transformed away. In general this can be accomplished via a canonical transformation of the basis. In other words given a Hamiltonian of the form

$$\hat{H}^{\text{BdG}}_k = \mathbf{v}^\dagger_k \begin{bmatrix} \boldsymbol{M}_k & \boldsymbol{N}_k \\ \boldsymbol{N}^\dagger_k & \boldsymbol{M}^*_k \end{bmatrix} \mathbf{v}_k = \tilde{\mathbf{v}}^\dagger_k \begin{bmatrix} \tilde{\boldsymbol{M}}_k & \mathbf{0} \\ \mathbf{0} & \tilde{\boldsymbol{M}}^*_k \end{bmatrix} \tilde{\mathbf{v}}_k \tag{C.9}$$

We select $\alpha_{j,k}$ and $\beta_{j,k}$ such that our new basis $\tilde{\mathbf{v}}_k$ puts $\hat{H}^{\text{BdG}}_k$ in a block diagonal form. The derivations of the following section then apply to the transformed block $\tilde{\boldsymbol{M}}_k$ which has matrix elements that connect each $\hat{\Upsilon}^\dagger_{i,k}$. This is relevant to the effective 2-band field theories we derive later. In the event that $\hat{H}^{\text{BdG}}_k$ does not contain pairing terms $\tilde{\boldsymbol{M}}_k = \boldsymbol{M}_k$ and $\hat{\Upsilon}^\dagger_{i,k}$ reduces to $\hat{\psi}^\dagger_{i,k}$. However the analyses we will present in the following section still holds.

C.1 Canonical transformation

We may obtain some intuitions about how the Kitaev like terms result in a topological band-gap by deriving the canonical transform. With the Hamiltonian in the form

$$\hat{H} = \sum_k \mathbf{v}^\dagger_k \boldsymbol{G}_k \mathbf{v}_k, \tag{C.10}$$

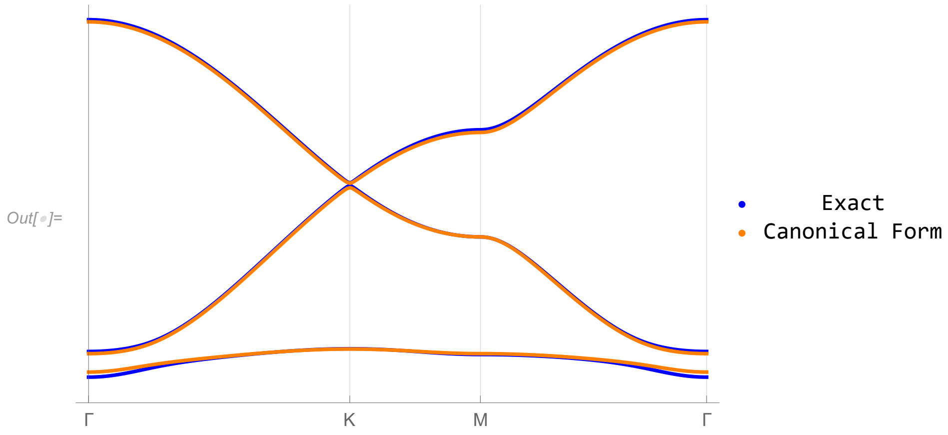

Figure C.1: We calculate the band energies with parameters $J^x = 0.5$, $J^y = 1.5$, $J^z = 1$ and $h = 5$ exactly and with the canonical transformation.

with $\mathbf{v}_k = [\hat{a}_k, \hat{b}_k, \hat{c}_k, \hat{a}^\dagger_{-k}, \hat{b}^\dagger_{-k}, \hat{c}^\dagger_{-k}]$ and

$$\boldsymbol{G}_k = \begin{bmatrix} \boldsymbol{M}_k & \boldsymbol{N}_k \\ \boldsymbol{N}_k^\dagger & \boldsymbol{M}_{-k}^T \end{bmatrix}. \tag{C.11}$$

We wish to derive the effective Hamiltonian

$$\hat{H}_{\text{eff}} = e^W \hat{H} e^{-W} = H + [W, H] + [W, [W, H]] + \dots \tag{C.12}$$

Ideally then W is chosen such that to first order in the above expansion the pairing terms are zeroed out so that we can return to a pure hopping Hamiltonian. If $\boldsymbol{M}_k$ and $\boldsymbol{N}_k$ are similar, then this is fairly straightforward. In this case they are not, but we can still cancel out these terms up to some desired order in η.

We do so by picking some generic $\boldsymbol{V}_k$ and fitting its parameters to give the desired result.

$$\boldsymbol{V}_k = \lambda \begin{bmatrix} 0 & C_k \\ -C_k & 0 \end{bmatrix} \tag{C.13}$$

Now we define the matrix

$$\sigma_3 = \begin{bmatrix} I_{3\times 3} & 0 \\ 0 & -I_{3\times 3} \end{bmatrix} \tag{C.14}$$

Then the matrix form of the commutator $[W, H]$ is

$$\boldsymbol{V}_k \sigma_3 \boldsymbol{G}_k - \boldsymbol{G}_k \sigma_3 \boldsymbol{V}_k = \lambda \begin{bmatrix} -C_k \boldsymbol{N}_k^\dagger - \boldsymbol{N}_k C_k^\dagger & -C_k \boldsymbol{M}_k^T - \boldsymbol{M}_k C_k \\ -C_k^\dagger \boldsymbol{M}_k - \boldsymbol{M}_k^T C_k^\dagger & -C_k^\dagger \boldsymbol{N}_k - \boldsymbol{N}_k^\dagger C_k \end{bmatrix}. \tag{C.15}$$

Since we wish to zero out the off-diagonal blocks of $\boldsymbol{G}_k$, we require that the upper right block of $[\boldsymbol{V}_k, \boldsymbol{G}_k]$ is equal to $-\boldsymbol{N}_k + O(1/\eta)$. This gives us

$$\lambda (C_k \boldsymbol{M}_k^T + \boldsymbol{M}_k C_k) = \boldsymbol{N}_k + O(1/\eta). \tag{C.16}$$

This is at the same time equivalent to requiring the lower left block to equal $-\boldsymbol{N}_k^\dagger$.

The above equation is solved by setting

$$\lambda = \frac{1}{2\eta} \tag{C.17}$$

and

$$C_k = \boldsymbol{N}_k. \tag{C.18}$$

The effective $\boldsymbol{M}_k$ block is now the new hopping Hamiltonian. After applying the correction this is

$$\begin{aligned} \boldsymbol{M}_k^{\text{eff}} &= \boldsymbol{M}_k - \boldsymbol{N}_k \boldsymbol{N}_k^\dagger / \eta & \text{(C.19)} \\ &= \begin{bmatrix} \eta & (\gamma_1)^* \cos(\lambda_3 \cdot k) & \gamma_1 \cos(\lambda_2 \cdot k) \\ \gamma_1 \cos(\lambda_3 \cdot k) & \eta & (\gamma_1)^* \cos(\lambda_1 \cdot k) \\ (\gamma_1)^* \cos(\lambda_2 \cdot k) & \gamma_1 \cos(\lambda_1 \cdot k) & \eta \end{bmatrix} \\ &\quad - \frac{\gamma_2^2}{\eta} \begin{bmatrix} \Delta_{2,3} & \omega^* \delta_{1,2} & \omega \delta_{3,1} \\ \omega \delta_{1,2} & \Delta_{3,1} & \omega^* \delta_{2,3} \\ \omega^* \delta_{3,1} & \omega \delta_{2,3} & \Delta_{1,2} \end{bmatrix}. & \text{(C.20)} \end{aligned}$$

For simplicity we have introduced the variables

$$\begin{aligned} \eta &= h/2 - J_z \\ \gamma_1 &= J_+ + iD_z \\ \gamma_2 &= J_-. \end{aligned} \tag{C.21}$$

As in Chapter 5 $J_\pm = (J_x \pm J_y)/2$. We also define

$$\begin{aligned} \Delta_{i,j} &= \cos^2(\lambda_i \cdot k) + \cos^2(\lambda_j \cdot k) \\ \delta_{i,j} &= \cos(\lambda_i \cdot k) \cos(\lambda_j \cdot k). \end{aligned} \tag{C.22}$$

We here see how the correction to results in a complex hopping, in this case with a $\frac{\gamma_2^2}{\eta} = \frac{J_-^2}{h/2 - J_z}$ prefactor. This also explains why there is only one type of Kitaev-like topological phase, the sign of J_- does not affect the correction.

On figure C.1 we compare the band energies of the pure hopping model approximated by a canonical transform and the exact energies derived from the BdG Hamiltonian. Even the lowest order correction gives fairly accurate results.

We may also write up the effective field at the band-gaps by expanding the above expression in k and projecting down onto the relevant 2×2 block. Doing so we obtain at the Γ point

$$\begin{aligned} d_1 &= ({k_x}^2/4 + k_x k_y \sqrt{3}/4 - {k_y}^2/4)(J_+/8 + {J_-}^2/(16h - 32J_z)) \\ d_2 &= ({k_x}^2 \sqrt{3}/4 - k_x k_y/4 - {k_y}^2 \sqrt{3}/4)(J_+/8 + {J_-}^2/(16h - 32J_z)) \\ d_3 &= [({k_x}^2 + {k_y}^2)/16 - 1]\sqrt{3} D_z - [({k_x}^2 + {k_y}^2)/8 - 1](3{J_-}^2)/(h - 2j_z). \end{aligned} \tag{C.23}$$

At the K (K') point we obtain

$$\begin{aligned} d_1 &= (\frac{1}{2}\alpha + \frac{2}{3}\beta)k_x + (-\frac{\sqrt{3}}{2}\alpha + \frac{2}{3\sqrt{3}}\beta)k_y \\ d_2 &= (\frac{\sqrt{3}}{2}\alpha - \frac{2}{3\sqrt{3}}\beta)k_x + (\frac{1}{2}\alpha - \frac{1}{2}\beta)k_y \\ d_3 &= \frac{\sqrt{3}}{2}D_z + \frac{3J_-{}^2}{8h - 16J_z}. \end{aligned} \tag{C.24}$$

Here the coefficients are

$$\begin{aligned} \alpha &= -\frac{\sqrt{3}}{4}J_+ + \frac{\sqrt{3}}{32}\frac{J_-}{\eta} \\ \beta &= \frac{\pi}{24}J_+ + \frac{\sqrt{11\pi}}{192}\frac{J_-}{\eta}. \end{aligned} \tag{C.25}$$

This analysis gives a straightforward approximation to the band-gap physics of spin-polarized kagome. It also confirms our assertions about the topology of these gaps, as the (d_1, d_2) vector has the winding that we expect to see. Additionally, this approximate solution shows why there is a phase with Chern numbers $c = (-1, 2, -1)$.

Bibliography

[1] A. Thomasen, K. Penc, N. Shannon, and J. Romhányi, arXiv:2012.11765 [cond-mat] (2021), arXiv:2012.11765 [cond-mat] .

[2] K. v. Klitzing, G. Dorda, and M. Pepper, Physical Review Letters **45**, 494 (1980).

[3] R. B. Laughlin, Physical Review B **23**, 5632 (1981).

[4] F. D. M. Haldane, Physical Review Letters **61**, 2015 (1988).

[5] C. L. Kane and E. J. Mele, Physical Review Letters **95**, 226801 (2005).

[6] M. Z. Hasan and C. L. Kane, Reviews of Modern Physics **82**, 3045 (2010).

[7] M. Onoda, S. Murakami, and N. Nagaosa, Physical Review Letters **93**, 083901 (2004).

[8] M. Fruchart, Y. Zhou, and V. Vitelli, Nature **577**, 636 (2020).

[9] Y. Onose, T. Ideue, H. Katsura, Y. Shiomi, N. Nagaosa, and Y. Tokura, Science **329**, 297 (2010).

[10] A. Mook, J. Henk, and I. Mertig, Physical Review B **89**, 134409 (2014).

[11] J. Romhányi, K. Penc, and R. Ganesh, Nature Communications **6**, 1 (2015).

[12] P. Fazekas, *Lecture Notes On Electron Correlation And Magnetism* (World Scientific, 1999).

[13] H. Kondo, Y. Akagi, and H. Katsura, Physical Review B **99**, 041110 (2019).

[14] N. W. Ashcroft and N. D. Mermin, *Solid-State Physics* (Academic Press, 1976).

[15] C. Kittel and P. McEuen, *Introduction to Solid State Physics* (John Wiley & Sons, 2019).

[16] X.-L. Qi and S.-C. Zhang, Reviews of Modern Physics **83**, 1057 (2011).

[17] N. Nagaosa, J. Sinova, S. Onoda, A. H. MacDonald, and N. P. Ong, Reviews of Modern Physics **82**, 1539 (2010).

[18] T. Ozawa, H. M. Price, A. Amo, N. Goldman, M. Hafezi, L. Lu, M. C. Rechtsman, D. Schuster, J. Simon, O. Zilberberg, and I. Carusotto, Reviews of Modern Physics **91**, 015006 (2019).

[19] J. E. Moore, Nature **464**, 194 (2010).

[20] D. J. Thouless, M. Kohmoto, M. P. Nightingale, and M. den Nijs, Physical Review Letters **49**, 405 (1982).

[21] B. A. Bernevig and T. L. Hughes, *Topological Insulators and Topological Superconductors* (Princeton University Press, 2013).

[22] H. Saito, Y. Kawaguchi, and M. Ueda, Physical Review A **75**, 013621 (2007).

[23] S. Tung, V. Schweikhard, and E. A. Cornell, Physical Review Letters **97**, 240402 (2006).

[24] R. Süsstrunk and S. D. Huber, Science **349**, 47 (2015).

[25] M. Serra-Garcia, V. Peri, R. Süsstrunk, O. R. Bilal, T. Larsen, L. G. Villanueva, and S. D. Huber, Nature **555**, 342 (2018).

[26] M. C. Rechtsman, J. M. Zeuner, Y. Plotnik, Y. Lumer, D. Podolsky, F. Dreisow, S. Nolte, M. Segev, and A. Szameit, Nature **496**, 196 (2013).

[27] Y. Kasahara, T. Ohnishi, Y. Mizukami, O. Tanaka, S. Ma, K. Sugii, N. Kurita, H. Tanaka, J. Nasu, Y. Motome, T. Shibauchi, and Y. Matsuda, Nature **559**, 227 (2018).

[28] S.-H. Do, S.-Y. Park, J. Yoshitake, J. Nasu, Y. Motome, Y. S. Kwon, D. T. Adroja, D. J. Voneshen, K. Kim, T.-H. Jang, J.-H. Park, K.-Y. Choi, and S. Ji, Nature Physics **13**, 1079 (2017).

[29] Y. Ando, Journal of the Physical Society of Japan **82**, 102001 (2013).

[30] L. Zhang, J. Ren, J.-S. Wang, and B. Li, Physical Review B **87**, 144101 (2013).

[31] R. Chisnell, J. S. Helton, D. E. Freedman, D. K. Singh, R. I. Bewley, D. G. Nocera, and Y. S. Lee, Physical Review Letters **115**, 147201 (2015).

[32] A. Rückriegel, A. Brataas, and R. A. Duine, Physical Review B **97**, 081106 (2018).

[33] H. Katsura, N. Nagaosa, and P. A. Lee, Physical Review Letters **104**, 066403 (2010).

[34] R. Matsumoto and S. Murakami, Physical Review Letters **106**, 197202 (2011).

[35] R. Matsumoto and S. Murakami, Physical Review B **84**, 184406 (2011).

[36] R. Shindou, J.-i. Ohe, R. Matsumoto, S. Murakami, and E. Saitoh, Physical Review B **87**, 174402 (2013).

[37] R. Shindou, R. Matsumoto, S. Murakami, and J.-i. Ohe, Physical Review B **87**, 174427 (2013).

[38] P. Drude, Annalen der Physik **306**, 566 (1900).

[39] A. Sommerfeld, Zeitschrift für Physik **47**, 1 (1928).

[40] F. Bloch, Zeitschrift für Physik **52**, 555 (1929).

[41] E. K. U. Gross and R. M. Dreizler, *Density Functional Theory* (Springer Science & Business Media, 2013).

[42] R. B. Laughlin, Physical Review Letters **50**, 1395 (1983).

[43] X. G. Wen and Q. Niu, Physical Review B **41**, 9377 (1990).

[44] B. A. Bernevig, C.-H. Chern, J.-P. Hu, N. Toumbas, and S.-C. Zhang, Annals of Physics **300**, 185 (2002).

[45] D. Hsieh, D. Qian, L. Wray, Y. Xia, Y. S. Hor, R. J. Cava, and M. Z. Hasan, Nature **452**, 970 (2008).

[46] S.-C. Zhang and J. Hu, Science **294**, 823 (2001).

[47] R. Joynt and R. E. Prange, Physical Review B **29**, 3303 (1984).

[48] R. E. Prange and R. Joynt, Physical Review B **25**, 2943 (1982).

[49] R. Joynt, Journal of Physics C: Solid State Physics **18**, L331 (1985).

[50] R. Joynt, Journal of Physics C: Solid State Physics **17**, 4807 (1984).

[51] B. I. Halperin, Physical Review B **25**, 2185 (1982).

[52] S. Murakami, N. Nagaosa, and S.-C. Zhang, Science **301**, 1348 (2003).

[53] P. Roushan, J. Seo, C. V. Parker, Y. S. Hor, D. Hsieh, D. Qian, A. Richardella, M. Z. Hasan, R. J. Cava, and A. Yazdani, Nature **460**, 1106 (2009).

[54] Z. Wang, Y. D. Chong, J. D. Joannopoulos, and M. Soljačić, Physical Review Letters **100**, 013905 (2008).

[55] A. Roth, C. Brüne, H. Buhmann, L. W. Molenkamp, J. Maciejko, X.-L. Qi, and S.-C. Zhang, Science **325**, 294 (2009).

[56] P. Cheng, C. Song, T. Zhang, Y. Zhang, Y. Wang, J.-F. Jia, J. Wang, Y. Wang, B.-F. Zhu, X. Chen, X. Ma, K. He, L. Wang, X. Dai, Z. Fang, X. Xie, X.-L. Qi, C.-X. Liu, S.-C. Zhang, and Q.-K. Xue, Physical Review Letters **105**, 076801 (2010).

[57] C. Brüne, C. X. Liu, E. G. Novik, E. M. Hankiewicz, H. Buhmann, Y. L. Chen, X. L. Qi, Z. X. Shen, S. C. Zhang, and L. W. Molenkamp, Physical Review Letters **106**, 126803 (2011).

[58] R. S. K. Mong and V. Shivamoggi, Physical Review B **83**, 125109 (2011).

[59] H. Aoki and T. Ando, Solid State Communications **38**, 1079 (1981).

[60] D. J. Thouless, Journal of Physics C: Solid State Physics **14**, 3475 (1981).

[61] M. Kohmoto, Annals of Physics **160**, 343 (1985).

[62] S. C. Zhang, T. H. Hansson, and S. Kivelson, Physical Review Letters **62**, 82 (1989).

[63] J. K. Jain, Physical Review Letters **63**, 199 (1989).

[64] K. Musaelian and R. Joynt, Journal of Physics: Condensed Matter **8**, L105 (1996).

[65] G. Moore and N. Read, Nuclear Physics B **360**, 362 (1991).

[66] K. I. Bolotin, F. Ghahari, M. D. Shulman, H. L. Stormer, and P. Kim, Nature **462**, 196 (2009).

[67] N. Y. Yao, A. V. Gorshkov, C. R. Laumann, A. M. Läuchli, J. Ye, and M. D. Lukin, Physical Review Letters **110**, 185302 (2013).

[68] F. D. M. Haldane, Physical Review Letters **93**, 206602 (2004).

[69] M. Ezawa, Physical Review Letters **109**, 055502 (2012).

[70] G. Jotzu, M. Messer, R. Desbuquois, M. Lebrat, T. Uehlinger, D. Greif, and T. Esslinger, Nature **515**, 237 (2014).

[71] S. K. Kim, H. Ochoa, R. Zarzuela, and Y. Tserkovnyak, Physical Review Letters **117**, 227201 (2016).

[72] S. A. Owerre, Journal of Physics: Condensed Matter **28**, 386001 (2016).

[73] E. Prodan, T. L. Hughes, and B. A. Bernevig, Physical Review Letters **105**, 115501 (2010).

[74] T. Thonhauser and D. Vanderbilt, Physical Review B **74**, 235111 (2006).

[75] N. Regnault and B. A. Bernevig, Physical Review X **1**, 021014 (2011).

[76] Y.-L. Wu, B. A. Bernevig, and N. Regnault, Physical Review B **85**, 075116 (2012).

[77] C. L. Kane and E. J. Mele, Physical Review Letters **95**, 146802 (2005).

[78] J. E. Moore and L. Balents, Physical Review B **75**, 121306 (2007).

[79] R. Roy, Physical Review B **79**, 195322 (2009).

[80] L. Fu, C. L. Kane, and E. J. Mele, Physical Review Letters **98**, 106803 (2007).

[81] X.-L. Qi, T. L. Hughes, and S.-C. Zhang, Physical Review B **78**, 195424 (2008).

[82] L. Fu and C. L. Kane, Physical Review B **74**, 195312 (2006).

[83] B. A. Bernevig, T. L. Hughes, and S.-C. Zhang, Science **314**, 1757 (2006).

[84] D. Hsieh, Y. Xia, L. Wray, D. Qian, A. Pal, J. H. Dil, J. Osterwalder, F. Meier, G. Bihlmayer, C. L. Kane, Y. S. Hor, R. J. Cava, and M. Z. Hasan, Science **323**, 919 (2009).

[85] A. Nishide, A. A. Taskin, Y. Takeichi, T. Okuda, A. Kakizaki, T. Hirahara, K. Nakatsuji, F. Komori, Y. Ando, and I. Matsuda, Physical Review B **81**, 041309 (2010).

[86] I. Knez, R. R. Du, and G. Sullivan, Physical Review B **81**, 201301 (2010).

[87] T. Hirahara, G. Bihlmayer, Y. Sakamoto, M. Yamada, H. Miyazaki, S.-i. Kimura, S. Blügel, and S. Hasegawa, Physical Review Letters **107**, 166801 (2011).

[88] J. Balakrishnan, G. K. W. Koon, M. Jaiswal, A. H. C. Neto, and B. Özyilmaz, Nature Physics **9**, 284 (2013).

[89] I. Knez, R.-R. Du, and G. Sullivan, Physical Review Letters **109**, 186603 (2012).

[90] C. Liu, T. L. Hughes, X.-L. Qi, K. Wang, and S.-C. Zhang, Physical Review Letters **100**, 236601 (2008).

[91] B. A. Bernevig and S.-C. Zhang, Physical Review Letters **96**, 106802 (2006).

[92] A. Shitade, H. Katsura, J. Kuneš, X.-L. Qi, S.-C. Zhang, and N. Nagaosa, Physical Review Letters **102**, 256403 (2009).

[93] M. König, M. Baenninger, A. G. F. Garcia, N. Harjee, B. L. Pruitt, C. Ames, P. Leubner, C. Brüne, H. Buhmann, L. W. Molenkamp, and D. Goldhaber-Gordon, Physical Review X **3**, 021003 (2013).

[94] S. Souma, M. Komatsu, M. Nomura, T. Sato, A. Takayama, T. Takahashi, K. Eto, K. Segawa, and Y. Ando, Physical Review Letters **109**, 186804 (2012).

[95] N. P. Butch, K. Kirshenbaum, P. Syers, A. B. Sushkov, G. S. Jenkins, H. D. Drew, and J. Paglione, Physical Review B **81**, 241301 (2010).

[96] D. Kim, S. Cho, N. P. Butch, P. Syers, K. Kirshenbaum, S. Adam, J. Paglione, and M. S. Fuhrer, Nature Physics **8**, 459 (2012).

[97] T. Valla, H. Ji, L. M. Schoop, A. P. Weber, Z.-H. Pan, J. T. Sadowski, E. Vescovo, A. V. Fedorov, A. N. Caruso, Q. D. Gibson, L. Müchler, C. Felser, and R. J. Cava, Physical Review B **86**, 241101 (2012).

[98] H. Steinberg, D. R. Gardner, Y. S. Lee, and P. Jarillo-Herrero, Nano Letters **10**, 5032 (2010).

[99] H. Lin, R. S. Markiewicz, L. A. Wray, L. Fu, M. Z. Hasan, and A. Bansil, Physical Review Letters **105**, 036404 (2010).

[100] F. Yang, L. Miao, Z. F. Wang, M.-Y. Yao, F. Zhu, Y. R. Song, M.-X. Wang, J.-P. Xu, A. V. Fedorov, Z. Sun, G. B. Zhang, C. Liu, F. Liu, D. Qian, C. L. Gao, and J.-F. Jia, Physical Review Letters **109**, 016801 (2012).

[101] S. Murakami, Physical Review Letters **97**, 236805 (2006).

[102] C. Sabater, D. Gosálbez-Martínez, J. Fernández-Rossier, J. G. Rodrigo, C. Untiedt, and J. J. Palacios, Physical Review Letters **110**, 176802 (2013).

[103] C. H. Lee, S. Imhof, C. Berger, F. Bayer, J. Brehm, L. W. Molenkamp, T. Kiessling, and R. Thomale, Communications Physics **1**, 1 (2018).

[104] A. Mook, J. Henk, and I. Mertig, Physical Review B **90**, 024412 (2014).

[105] M. Hirschberger, J. W. Krizan, R. J. Cava, and N. P. Ong, Science **348**, 106 (2015).

[106] M. Hirschberger, R. Chisnell, Y. S. Lee, and N. P. Ong, Physical Review Letters **115**, 106603 (2015).

[107] X. Qin, F. Mei, Y. Ke, L. Zhang, and C. Lee, Physical Review B **96**, 195134 (2017).

[108] S. A. Owerre, Journal of Physics: Condensed Matter **29**, 385801 (2017).

[109] S. A. Owerre, Journal of Physics: Condensed Matter **30**, 245803 (2018).

[110] P. Laurell and G. A. Fiete, Physical Review Letters **118**, 177201 (2017).

[111] P. Laurell and G. A. Fiete, Physical Review B **98**, 094419 (2018).

[112] M. Malki and G. S. Uhrig, Physical Review B **99**, 174412 (2019).

[113] D. Bhowmick and P. Sengupta, Physical Review B **101**, 214403 (2020).

[114] H. Zhang, X. Feng, T. Heitmann, A. I. Kolesnikov, M. B. Stone, Y.-M. Lu, and X. Ke, Physical Review B **101**, 100405 (2020).

[115] H. Kondo, Y. Akagi, and H. Katsura, Physical Review B **100**, 144401 (2019).

[116] S. A. Owerre, EPL (Europhysics Letters) **125**, 36002 (2019).

[117] P. A. McClarty, F. Krüger, T. Guidi, S. F. Parker, K. Refson, A. W. Parker, D. Prabhakaran, and R. Coldea, Nature Physics **13**, 736 (2017).

[118] S. Miyahara and K. Ueda, Journal of Physics: Condensed Matter **15**, R327 (2003).

[119] K. Onizuka, H. Kageyama, Y. Narumi, K. Kindo, Y. Ueda, and T. Goto, Journal of the Physical Society of Japan **69**, 1016 (2000).

[120] H. Nojiri, H. Kageyama, K. Onizuka, Y. Ueda, and M. Motokawa, Journal of the Physical Society of Japan **68**, 2906 (1999).

[121] K. Kodama, M. Takigawa, M. Horvatić, C. Berthier, H. Kageyama, Y. Ueda, S. Miyahara, F. Becca, and F. Mila, Science **298**, 395 (2002).

[122] J. Schlappa, T. Schmitt, F. Vernay, V. N. Strocov, V. Ilakovac, B. Thielemann, H. M. Rønnow, S. Vanishri, A. Piazzalunga, X. Wang, L. Braicovich, G. Ghiringhelli, C. Marin, J. Mesot, B. Delley, and L. Patthey, Physical Review Letters **103**, 047401 (2009).

[123] K. P. Schmidt and G. S. Uhrig, Physical Review Letters **90**, 227204 (2003).

[124] K. Hwang and Y. B. Kim, Physical Review B **93**, 235130 (2016).

[125] H. Kuroe, T. Hamasaki, T. Sekine, M. Hase, K. Oka, T. Ito, H. Eisaki, and M. Matsuda, Journal of Physics: Conference Series **200**, 022028 (2010).

[126] G. S. Uhrig, K. P. Schmidt, and M. Grüninger, Physical Review Letters **93**, 267003 (2004).

[127] S. A. Owerre, Physical Review B **94**, 094405 (2016).

[128] S. A. Owerre, Journal of Physics: Condensed Matter **29**, 03LT01 (2016).

[129] V. A. Zyuzin and A. A. Kovalev, Physical Review Letters **117**, 217203 (2016).

[130] D. G. Joshi and A. P. Schnyder, Physical Review B **100**, 020407 (2019).

[131] P. Shen and S. K. Kim, Physical Review B **101**, 125111 (2020).

[132] D. Malz, J. Knolle, and A. Nunnenkamp, Nature Communications **10**, 3937 (2019).

[133] E. Thingstad, A. Kamra, A. Brataas, and A. Sudbø, Physical Review Letters **122**, 107201 (2019).

[134] G. Go, S. K. Kim, and K.-J. Lee, Physical Review Letters **123**, 237207 (2019).

[135] A. Mook, J. Henk, and I. Mertig, Physical Review Letters **117**, 157204 (2016).

[136] A. Mook, J. Henk, and I. Mertig, Physical Review B **95**, 014418 (2017).

[137] S.-K. Jian and W. Nie, Physical Review B **97**, 115162 (2018).

[138] M. R. Norman, Physical Review B **40**, 10632 (1989).

[139] G. H. Wannier, Physical Review **117**, 432 (1960).

[140] R. Balian and E. Brezin, Il Nuovo Cimento B Series 10 **64**, 37 (1969).

[141] A. V. Chubukov and D. I. Golosov, Journal of Physics: Condensed Matter **3**, 69 (1991).

[142] A. L. Chernyshev and M. E. Zhitomirsky, Physical Review B **79**, 144416 (2009).

[143] M. Mourigal, W. T. Fuhrman, A. L. Chernyshev, and M. E. Zhitomirsky, Physical Review B **88**, 094407 (2013).

[144] C. Knetter, A. Bühler, E. Müller-Hartmann, and G. S. Uhrig, Physical Review Letters **85**, 3958 (2000).

[145] K. Totsuka, S. Miyahara, and K. Ueda, Physical Review Letters **86**, 520 (2001).

[146] A. Koga and N. Kawakami, Physical Review Letters **84**, 4461 (2000).

[147] B. Sriram Shastry and B. Sutherland, Physica B+C **108**, 1069 (1981).

[148] S. Sachdev and R. N. Bhatt, Physical Review B **41**, 9323 (1990).

[149] P. Corboz and F. Mila, Physical Review B **87**, 115144 (2013).

[150] T. Moriya, Physical Review **120**, 91 (1960).

[151] T. Haku, M. Soda, M. Sera, K. Kimura, S. Itoh, T. Yokoo, and T. Masuda, Journal of the Physical Society of Japan **85**, 034721 (2016).

[152] K. Kimura, S. Nakatsuji, and T. Kimura, Physical Review B **90**, 060414 (2014).

[153] T. Fukui, Y. Hatsugai, and H. Suzuki, Journal of the Physical Society of Japan **74**, 1674 (2005).

[154] J. M. Domingos, International Journal of Theoretical Physics **18**, 213 (1979).

[155] K. Kimura, S. Nakatsuji, J.-J. Wen, C. Broholm, M. B. Stone, E. Nishibori, and H. Sawa, Nature Communications **4**, 1934 (2013).

[156] E. Lhotel, S. Petit, M. Ciomaga Hatnean, J. Ollivier, H. Mutka, E. Ressouche, M. R. Lees, and G. Balakrishnan, Nature Communications **9**, 3786 (2018).

[157] H. Yan, R. Pohle, and N. Shannon, Physical Review B **98**, 140402 (2018).

[158] S. Shivam, R. Coldea, R. Moessner, and P. McClarty, arXiv:1712.08535 [cond-mat] (2017), arXiv:1712.08535 [cond-mat] .

[159] K. Essafi, O. Benton, and L. D. C. Jaubert, Physical Review B **96**, 205126 (2017).

[160] P. A. McClarty, X.-Y. Dong, M. Gohlke, J. G. Rau, F. Pollmann, R. Moessner, and K. Penc, Physical Review B **98**, 060404 (2018).

[161] A. Corticelli, R. Moessner, and P. A. McClarty, arXiv:2103.05656 [cond-mat] (2021), arXiv:2103.05656 [cond-mat] .

[162] M. S. Dresselhaus, G. Dresselhaus, and A. Jorio, *Group Theory: Application to the Physics of Condensed Matter* (Springer Science & Business Media, 2007).

[163] M. Tinkham, *Group Theory and Quantum Mechanics* (Courier Corporation, 2003).

[164] J. A. Salthouse, M. J. Ware, and Salthouse, *Point Group Character Tables and Related Data* (CUP Archive, 1972).

[165] O. Benton, arXiv:2008.04677 [cond-mat] (2020), arXiv:2008.04677 [cond-mat] .